Coherent and cavity-based measurement of two-particle states

by

Joelle Joy Tiffany Corrigan

A dissertation submitted in partial fulfillment of

the requirements of the degree of

Doctor of Philosophy

(Physics)

at the

University of Wisconsin-Madison

2021

Date of final oral examination: August 23, 2021

This dissertation is approved by the following members of the Final Oral Committee:
Mark Eriksson, Professor, Physics
Susan Coppersmith, Professor, Physics
Mark Friesen, Distinguished Scientist, Physics
Robert McDermott, Professor, Physics
Donald Savage, Associate Scientist, Materials Science Engineering

Abstract

The possibility of a quantum computer continues to grow as arrays at the tens of quantum bits (qubits) level have been demonstrated. With an operational quantum computer comes access to computations infeasible today with the largest supercomputers; however, to achieve a computer at fault-tolerant levels, millions of qubits are necessary. Since most qubit platforms require complicated technologies to induce extreme environments like high vacuum, used to isolate the system, and cryogenic temperatures, used to minimize thermal excitations, scaling to the million-qubit level will be nontrivial. Thus, thought and effort must be put towards systems that have the potential to scale up.

Electrons or holes in semiconducting quantum dot qubits provide a promising path forward. They are very similar to the billions of transistors found in each smart phone used today, and are therefore quite small and have the possibility for large-scale industrial fabrication. Full understanding and sensitive readout of qubit levels are important requirements of any qubit architecture, but particularly in nanometer scale quantum dots which are highly sensitive to the material and electric potential landscapes of the operating device.

This thesis presents methods of readout enhancement and characterization of two-electron states in Si/SiGe quantum dot devices. The work focuses on the quantum dot hybrid qubit (QDHQ), a qubit encoding combining charge and spin states of electrons shared between two quantum dots. It presents a tunable latched readout protocol which maps a spin-like qubit state onto a metastable charge state, providing increased readout sensitivity and control over the measurement sequence. Next, there is a discussion of the tunability of the QDHQ

energy, including Ramsey spectra at various tunings measured using the latched protocol. Then, the latched technique is used in coherent measurements of two-electron states in the Wigner molecule regime, where strong electron-electron interactions soften the excited state spectrum. Finally, this work demonstrates an enhancement in transmission through a superconducting readout resonator in the presence of a double-dot-detuning drive, and uses this enhancement to perform excited-state readout of a QDHQ. This readout additionally acts as a spectroscopy of the singlet-triplet splitting in each quantum dot.

Acknowledgements

As my graduate school journey brought me through essentially every emotion imaginable, there have been countless people who have provided me support, encouragement, mentorship, education, and friendship along the way. This thesis would not be possible without all of them.

I first want to thank the members on my committee, Prof. Mark Eriksson, Prof. Susan Coppersmith, Dr. Mark Friesen, Prof. Robert McDermott, and Dr. Donald Savage, for setting aside time in the precious days before the semester starts to read through my thesis and attend my defense. Particularly with the oncoming COVID Delta-variant, this sacrifice is not lost on me.

Considering all the other careers I had in mind in high school (eg: Culinary Artist, French Teacher, Psychologist), I need to first start with acknowledging the professors at Hamilton College who sparked and cultivated my interest. Through a random bout of luck, I enrolled in the introductory physics course of Prof. Gordon Jones as an intended Psychology major. His passion for the subject opened my eyes to the beauty of physics, and his supportive mentoring style convinced me that it was a field in which I belonged. The next fall, I found myself in my first Quantum Physics course with Prof. Ann Silversmith, where I fell in love with the 'magic' that is quantum mechanics. Both Gordon and Ann provided me with endless mentorship throughout my career at Hamilton, in addition to Prof. Brian Collett and Prof. Kate (Jones-Smith) Brown. Gordon would go on to be my undergraduate thesis advisor, giving me both support and independence, and continues to be a lifelong mentor

and friend.

I adamantly said I would never go to physics graduate school, until Gordon encouraged me to apply to the Summer Undergraduate Research Fellowship (SURF) program at NIST in Gaithersburg, MD. I spent the summer with his former colleagues, Drs. Wangchun Chen and Shannon Watson. It was there that I learned what it could really mean to be an experimental physicist and I was finally resigned to pursuing my doctorate. Wangchun and Shannon were amazing experimentalists and great teachers, and I thank them for their endless help and for putting up with me for two whole summers.

When I was ready to look for graduate research programs, the one that stood out was Prof. Mark Eriksson's group studying quantum dot qubits. I had no experience or exposure to quantum computing when applying, but have come so far since my first day in the lab, and a huge part of that is from having Mark as an advisor. Mark has an amazing amount of knowledge, though never condescends, and is happy to answer questions and facilitate discussion. He also has an infectious optimism and excitement for science; this is hugely important for dejected graduate students when they think their entire world (read: PhD) is doomed. I hit that point many, many times while working on my PhD, and Mark was there at each one helping me regain my perspective, inspiration, and motivation. In addition to these things, Mark is someone who always strives to do the right thing, do good by others, and act in a compassionate or understanding manner; the lessons he taught me I will try to emulate for the rest of my life. I want to thank Mark for all of those moments, all the other ones, and of course all the work that goes unseen.

In addition to Prof. Mark Eriksson, there were two other PIs who each had a large presence in the Eriksson group - Prof. Susan Coppersmith and Dr. Mark Friesen, both of whom deserve tremendous thanks. When I started in the group, Sue (a theorist) would walk around for our daily meetings in the lab. Though she may never admit it, she has a nearly perfect track record for experimental suggestions and interpretations, and additionally has a very strong intuition when it comes to writing papers and making figures, etc. Essentially,

she is a fountain of wisdom, and is someone from whom you can learn something new with every conversation.

Dr. Mark Friesen has been a huge help throughout my PhD. Whenever there is a theoretical concept that has made my brain hurt from staring at it for too long, Mark was happy to help, sit down with me and walk through the derivation or explanation. I would always leave with much greater understanding, and with the knowledge that I could come back again when I realized there was still more I did not understand. Mark has a passion for bring intuitive understanding to complex theory, which is an important practice I have learned to value and benefitted from greatly.

In addition to Mark, Mark, and Sue, both Dr. Don Savage and Prof. Robert McDermott have helped me throughout my PhD as well. Don, a grower and closer collaborator with the group, has a knack for bringing a broader perspective to conference and job talks. His questions and suggestions are vital to building better presentations, and bringing us all out of our tunnel vision. Robert, with his endless knowledge of superconducting cavities and happiness to answer our unending questions, has been invaluable to the last chapter of this work.

I have been truly lucky to have been able to work with so many talented and friendly graduate students and post-docs in my time in the Eriksson group, many of whom I will consider lifelong friends. To thank them each for their specific help would extend this section even further, so here I list in a somewhat chronological order: Ryan Foote, Brandur Thorgrimsson, Trevor Knapp, Luke Smith, Adam Frees, Sam Neyens, Yuan-chi Yang, Evan MacQuarrie, Gabriel Jaffe, JP Dodson, Tom McJunkin, Nathan Holman, Mario Palma, Ekmel Ercan, Jose Carlos Abadillo-Uriel, Michael Wolfe, Ben Harpt, Abigail Shearrow, Merritt Losert, Emily Joseph, Sanghyeok Park, Piotr Marciniec, and Jack Reily. Though I have never met them, I would like to also thank Christie Simmons, Zhan Shi and Xian Wu for first being incredible physicists, and next for being inspirational female alumni of the Eriksson group, particularly in the many years when I was the only woman.

An enormous thanks goes to Prof. Lisa Everett, who has done so much for the department, and who has been an amazing mentor for me during my five years here. There were many times when she convinced me to keep going and for that I am in her debt. I additionally want to thank Ann Austin for her invaluable work getting all of the supplies needed for our experiments off the computer and into our hands. She is truly an angel. Additional thanks go to Sara Yaeger in the student shop for her patience and understanding with my limited milling experience, as well as Michelle Holland, Allison Tredinnick, Chad Seys, Keeley Bannon and Aimee Lefkow for their hard work and help with all of my various issues throughout the years.

Of course, so much of the work done here would not have been possible without the support of my parents, family, friends, and my therapist, all of whom were integral in keeping me sane throughout this whole process. Finally, the last thanks goes to my loving husband Micah, who has gotten particularly good at explaining the work I do to family and friends.

Funding acknowledgements:

Unless otherwise noted, the work in this thesis is sponsored in part by the Army Research Office (ARO), through Grant No. W911NF-17-1-0274. JC acknowledges support from the National Science Foundation Graduate Research Fellowship Program under Grant No. DGE-1747503 and the Graduate School and the Office of the Vice Chancellor for Research and Graduate Education at the University of Wisconsin-Madison with funding from the Wisconsin Alumni Research Foundation. We acknowledge the use of nanofacilities supported by the NSF through the UW-Madison MRSEC (DMR-1720415) and by the NSF MRI program (DMR-1625348). The views and conclusions contained in this paper are those of the authors and should not be interpreted as representing the official policies, either expressed or implied, of the ARO, NSF, or the U.S. Government. The U.S. Government is authorized to reproduce and distribute reprints for Government purposes notwithstanding any copyright notation herein.

Contents

List of Figures

List of Tables

Chapter 1

Introduction to Quantum Computing

1.1 The quantum bit

Though the first proposals for a quantum computer surfaced in the 1980s and 1990s [1–6], and research funding began distribution in the early 2000s, the field has gained momentum in the last 5-10 years with the help of government and private funding, national and international collaboration, and expanded education of a growing workforce. The technology is centered around the idea of the quantum bit, or qubit, as compared with a classical bit. All computers today, from a smart phone and laptop to a supercomputer, operate using classical bits which can take the binary values of 0 or 1. Qubits instead take advantage of the quantum mechanical properties of superposition and entanglement, both of which are what make the possibility of a real quantum computer so promising.

Superposition allows the qubit state to not only be in 0 or 1, but in some probabilistic linear combination of both values. The qubit's value, or wave function, can then be defined as $|\psi\rangle = \alpha|0\rangle + \beta|1\rangle$. Since each classical bit can only hold one finite value, 5 classical bits will only hold 5 pieces of information. However, the information storage of N qubits is exponential like 2^N so that 5 qubits can hold $2^5 = 32$ pieces of information. Moving from 5 to 32 may not seem like such a large jump, but with 100 qubits, the gain is from 100 to

$1.27 \cdot 10^{30}$, which is quite clearly beneficial.

Entanglement is a phenomenon where multiple qubits can be correlated in such a way that the total quantum state of all the qubits cannot be described in terms of the states of each individual qubit. When considering two qubits A and B, each in superposition states of $|\psi\rangle_{A,B} = \frac{1}{\sqrt{2}}(|0\rangle_{A,B} + |1\rangle_{A,B})$, the unentangled system is given by:

$$|\psi\rangle_A \otimes |\psi\rangle_B = \frac{1}{2}\big(\,|0\rangle_A \otimes |0\rangle_B + |0\rangle_A \otimes |1\rangle_B + |1\rangle_A \otimes |0\rangle_B + |1\rangle_A \otimes |1\rangle\,\big),$$

simplified as $|\psi_A\psi_B\rangle = \frac{1}{2}\big(\,|00\rangle + |01\rangle + |10\rangle + |11\rangle\big)$. Note how the combined, unentangled state formed from two qubits in maximum superposition states contains all four possible state combinations. Conversely, the four maximally entangled Bell states [7] $|\Phi^{\pm}\rangle = \frac{1}{\sqrt{2}}(|00\rangle \pm |11\rangle)$ and $|\Psi^{\pm}\rangle = \frac{1}{\sqrt{2}}(|01\rangle \pm |10\rangle)$, cannot be generated from two individual qubit wavefunctions. These correlations persist even as the qubits are separated so that a measurement of one qubit which collapses the wavefunction will determine the state of the other qubit. This is true even if the qubits are separated far enough and measured fast enough that the information transfer from one location to the other would need to travel as much as four times the speed of light, as experimentally demonstrated in Ref. [8]. Thus, quantum entanglement allows for advances like quantum communication and information transfer.

While some of the important applications of quantum computers will require millions of qubits [9], and even reaching the 100-1000 qubit limit is a challenging task, recent progress in the superconducting qubit community has allowed for a breach of the 50 qubit limit [10, 11] and demonstration of quantum supremacy [10], albeit on a specifically constructed problem. Though the path from 50 to 1000 or 1 million qubits may not be easy, there is strong motivation from a range of fields to keep efforts going. For example, an array of qubits can efficiently model a quantum system by initializing the array in a desired starting state and letting it evolve over time [12, 13]. This type of modeling will be very beneficial for studying the behavior of large numbers of particles, and can be used for understanding current or new

materials as well as chemical interactions like those between molecules in our bodies and new pharmaceuticals.

In addition to modeling, there are specific algorithms proposed with which a quantum computer will have a large advantage over a classical computer. One example is Shor's algorithm for integer factorization [14]. For some number N with d digits, which is a product of two prime numbers p and q, $N = p * q$, it is incredibly difficult and time consuming classically to find what p and q are, even using the most powerful supercomputers. The most efficient algorithm can find the solution with the run time on order $e^{(logN)^{1/3}(loglogN)^{2/3}}$ for integer N with digits d, with the record number of digits d = 250 [15]. However, using Shor's algorithm, the problem can be solved on order $(logN)^2(loglogN)(logloglogN)$, no longer an exponential growth. This may not seem readily useful, but in fact the RSA public-key cryptosystem which is used for safe transfer of data relies on the hardness of the prime factorization problem. Given how much of our personal data is transferred over the internet, moving past the RSA cryptosystem to something quantum-secure will become increasingly important.

Another example is Grover's algorithm for unstructured search [16]. This algorithm essentially allows for the retrieval of some value x in a list of span N, or in other words computes the inverse of some function f(x) to find the value x for which f(x) = a. Using classical operations, this search will at maximum take N operations by looking at every item in the list; if only 50% accuracy is desired, it could be reduced to N/2. Using a quantum computer instead would allow for solving the problem in $\sqrt{N}$ operations, a great increase in computational speed as compared to a classical computer.

1.2 The Bloch sphere

To fully understand the power of the qubit as compared to the classical bit, it is useful to visualize a quantum state $|\psi\rangle$ using a Bloch sphere, where the poles of the sphere will be $|0\rangle$

and $|1\rangle$. Fig. 1.1 depicts a Bloch sphere, with coordinates x,y,z, and quantum state $|\psi\rangle = \alpha|0\rangle + \beta|1\rangle$. Since α and β are normalized to 1, $|\psi\rangle$ is confined to always live on the Bloch sphere's surface. Thus, it can be useful to instead discuss the state in terms of spherical coordinates, where $\alpha = \cos(\theta/2)$ and $\beta = e^{i\phi}\sin(\theta/2)$.

Using the spherical definition, it is clear that basic qubit operations can be depicted as rotations around various axes of the Bloch sphere. For example, changing the qubit from entirely $|0\rangle$ ($\beta = 0$) to entirely $|1\rangle$ ($\alpha = 0$) involves rotating around the x-axis by $\theta = \pi$. Thus, this process is called an X-rotation or X gate. If instead it is necessary to accumulate a coherent phase of the qubit at an equal superposition, a rotation around the z-axis at the sphere's equator is required. This is achieved with $\theta = \pi/2$ and changing ϕ, and is called a Z-rotation or Z gate. Using combinations of θ and ϕ, it is therefore possible to place ψ anywhere on the surface of the sphere, allowing for gates of more arbitrary nature around some axis N. In linear algebra, two unique vectors will span an entire two dimensional space, meaning any arbitrary vector can be created with linear combinations of two unique vectors. Similarly, two unique axis of rotation allow for complete control of the Bloch sphere and the qubit state.

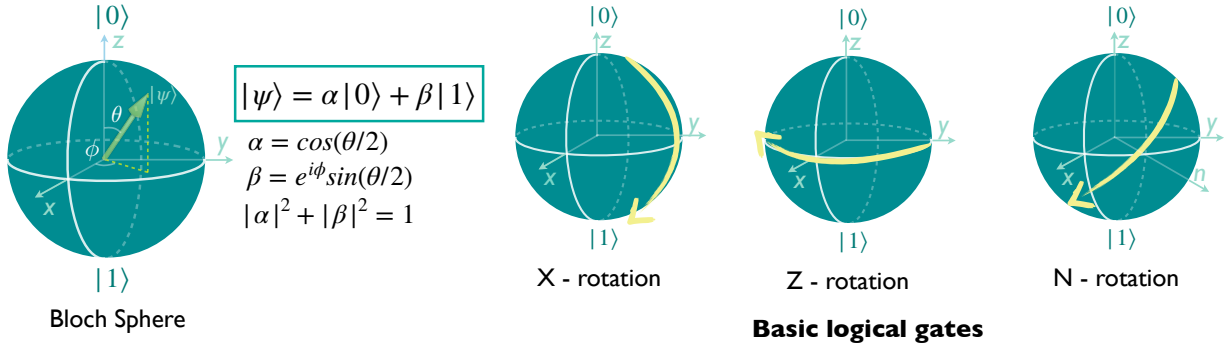

Figure 1.1: The superposition of two quantum states, $|0\rangle$ and $|1\rangle$, can be represented by positions on the surface of a sphere, called the Bloch sphere. $|0\rangle$ and $|1\rangle$ will be the poles of the sphere, and the linear combination of the two, $|\psi\rangle = \alpha|0\rangle + \beta|1\rangle$ brings you to a certain point on the sphere. To place the qubit in such a position, and thus form a qubit for viable use in a quantum computer, two-axis control of the Bloch sphere is needed. This can be achieved through basic logical gates like X and Z rotations, or else some combination of more arbitrary gates around an axis N.

1.3 DiVincenzo criteria

Although measurement of a single qubit is an amazing scientific feat, it alone will not be sufficient to actualize a quantum computer. This actualization can occur if a set of five requirements, as proposed by DiVincenzo [17], are met. These criteria have been useful to compare various qubit platforms or highlight areas which must still be addressed in order for a subfield to progress. The criteria are as follows:

1. **Scalable, well defined qubits:** As described above, a full scale quantum computer will need millions of qubits. This is well beyond the limit where each qubit can be independently tuned in the lab by some graduate student according to the qubit's unique characteristics. Instead, the qubits must be repeatable, well understood, and it must be feasible to get the qubit array to the million qubit level. At the single qubit level, there are specific parameters which must be known for the qubit to qualify as 'well defined'. These include: the internal Hamiltonian of the qubit; the presence of other states within the device, and the probability of leaking into said states; and couplings to other states, other qubits, and external fields.

2. **Initialization into a known state:** As is common in classical computing, it is important for the qubit array to be able to be initialized into a known value before starting a new computation. It is additionally required for quantum error correction to periodically have arrays of qubits reset to a known state, such as $|0\rangle$ [18–20]. This initialization can be achieved by waiting for some decay process between an excited and ground state, by pumping or driving the system into the desired state, or by measurement projection into a desired state. The various methods will each have constraints, but in general it will be important for error correction to be able to initialize the system quickly in comparison with qubit decoherence times.

3. **Decoherence compared with gate times:** The decoherence time of a qubit puts a bound on how long the qubit can be used before it's information is lost. The de-

coherence properties will depend on the qubit's interaction with its environment and the choice of the qubit's basis states. The goal is of course to have as many qubit operations as possible within the decoherence time limit; it is estimated that, using error correction schemes, a decoherence time $10^4 - 10^5$ times longer than the gate time will be viable [21]. This can additionally be addressed using error correction, where fault-tolerant computing can be achieved as long as the computational error rates are below a certain threshold, as discussed in Ref. [22].

4. **Universal gate set:** Similar to classical computation, where the logical gate NAND can be used to generate any other logical gate, it is important to have a method to generate all desired quantum gates. This can be achieved with two-axis control of each single qubit, and two qubit gates of just one type such as a cNOT gate. From these two requirements, all other more complex gates can be generated; of course, that may not always be the most efficient method. The rather flexible requirements on the types of gates are important, as each qubit system will be subject to it's natural gates and two-body interactions.

5. **Qubit specific readout:** With a large array of qubits, the ability to read out each qubit individually with high accuracy is crucial. Since a measured qubit value will be stored as a classical bit after computation, quantum algorithms should end with all the measured qubits as $|0\rangle$ or $|1\rangle$. Perfect accuracy of the qubit state after a single measurement would indicate 100% quantum efficiency; however, that level of efficiency is not physically possible. Instead, a more realistic solution is to have relatively high efficiency (i.e. in the high 90% limit), in conjunction with repeated measurement to increase confidence in the qubit's state before transferring it to the classical bit.

In addition to the five criteria for a large scale quantum computer listed above, there are also two additional criteria needed for quantum communication, an additional application of quantum computing attractive for high security transfer of information over long distances

(ie: secret key sharing). Both requirements involve flying qubits: qubits that will be transmitted between two locations. Note that the optimal platform for these flying qubits will almost surely be different from that of the local, stationary qubits, and will likely make use of optical fiber technology to encode the qubits as photons [23, 24]. The two necessary criteria for these flying qubits to be used for quantum communication are:

1. **Interfacing stationary and flying qubits:** If there are indeed different qubits used for transmitting the information and for local processing, it will be necessary to interface the two types of qubits and transfer information between them.

2. **Faithful transmission of flying qubits between specfied locations:** A key requirement of flying qubits will be successful transmission within the qubit's decoherence time. This is of course why optical fibers and photons are so attractive, as they will essentially be the fastest mode of transportation available.

Of course, even if these requirements are met, the problem of quantum computing requires addressing not only the qubit systems themselves, but the hardware, control, compilers, libraries, and algorithms. This 'quantum computing stack' or 'full stack' is summarized in Ref. [25]. It is sophisticated development of all of these technologies that will allow for a full scale quantum computer.

1.4 Thesis outline

This thesis covers a range of experiments using two Si/SiGe quantum dot devices, all of which were performed at the University of Wisconsin-Madison. Although the techniques vary between experiments, they were all focused on characterization and manipulation of multi-electron double quantum dots in regimes at or similar to the quantum dot hybrid qubit (QDHQ).

Chapter 2 outlines a tunable latched readout protocol for the QDHQ which allows for the mapping of spin states onto charge states at a longer time-scale and higher charge

sensitivity than traditional charge-mapped readout. The chapter starts with an introduction of semiconducting quantum dots and then compares the QDHQ to charge and single-spin qubits. Next, latched readout for a QDHQ is introduced, explaining the relevant tunnel rates and highlighting the 'readout zone' typical in a charge stability diagram. Tuning of the relevant tunnel rates into the necessary regime is demonstrated, and the chapter concludes with Rabi and Ramsey measurements of a QDHQ achieved with latched readout.

Chapter 3 discusses in detail the range of relevant Hamiltonian parameters that impact the QDHQ energy dispersion and how they translate to changes in the dispersion slope and curvature. Beginning with an explanation of the QDHQ dispersion, the dependence of the dispersion, slope, and curvature on changes in the relevant tunnel couplings is plotted. This is followed by a discussion on the importance of the dispersion's slope and curvature for single and two-qubit gates, and presentation of Ramsey data taken with three different energy dispersions. To compliment the above discussion, the last part of the chapter introduces an additional level to the QDHQ Hamiltonian and discusses the consequences with respect to both energy dispersions. This expanded Hamiltonian will be relevant for the following chapter.

Chapter 4 presents Rabi and Ramsey data of a QDHQ-like system where not one but 8 different transitions were coherently manipulated; this phenomena is explained with strong electron-electron interactions and Wigner molecule physics. Rabi and Ramsey data for two transitions is demonstrated first, followed by Rabi measurements at a third microwave frequency producing not one but two on-resonant Rabi oscillations. The chapter then introduces the Wigner molecule limit, where the electron-electron interaction energy is larger than the orbital confinement strength, and produces a similar density of states to those experimentally measured using tight-binding and FCI calculations. The chapter ends by plotting all of the seemingly separate Rabi and Ramsey data on a plot with energy dispersions of a 6-level Hamiltonian to good agreement when considering excitations from both the ground state and a low-lying excited state. After the main text, there is supplementary material which

includes additional data, and details of both the simulations and experimental methods.

Chapter 5 highlights measurements on a quantum dot chip which is connected to a separate superconducting resonator chip, presenting evidence of an enhanced coupling mechanism of the quantum dots to the cavity and demonstrating excited state spectroscopy of the singlet-triplet levels used in a QDHQ. The chapter first includes a quick introduction on dispersive readout. Next, data is shown explaining an enhanced coupling effect of the double quantum dots to the cavity produced by driving one of the quantum dots at the cavity frequency. Singlet-triplet spectroscopy of the double dot system, using the enhanced regime, is explained and data is presented. Finally, the chapter outlines a proposal for reducing the high-frequency cabling requirements for this and similar systems.

Chapter 2

Latched readout of a quantum dot hybrid qubit

This chapter describes a method for qubit readout in a quantum dot hybrid qubit using a latching process to hold the system in a metastable charge state, increasing the charge sensitivity and reducing bandwidth constraints of the system. First, semiconductor quantum dots are introduced, and the operation of a double-quantum-dot system is explained. This is followed by a brief explanation of basic types of qubits one could form in a quantum dot, and then an explanation of the quantum dot hybrid qubit (QDHQ), which is the qubit encoding used throughout the rest of this thesis. The second half of this chapter explains the benefits and protocols for implementing latched readout of a QDHQ, and demonstrates Rabi and Ramsey measurements performed using this readout method.

2.1 The quantum dot hybrid qubit

2.1.1 Semiconducting quantum dots

Forming qubits based on electrons within semiconducting quantum dots was proposed by Loss and DiVencenzo in 1998 [26], and has since been pursued by research groups across the

world realizing both single [27–33] and two qubit gates [34–40]. Although there are various types of qubit definitions depending on the total number of electrons or quantum dots per qubit, whether there is an applied magnetic field, etc, the general device structure is fairly similar. Starting with a semiconducting material stack, a 2D electron gas (2DEG) or 2D hole gas (2DHG) is generated, confining the particles to a 2D plane. Metal structures called gate electrodes (or gates) are deposited on top of the materials stack, on which positive or negative voltages can be applied relative to the 2DEG or 2DHG. These voltage values control the electric potential landscape that the carriers experience. This work is focused entirely on electrons, and so those carriers are in a 2DEG. Early Si/SiGe quantum dots used Schottky top gates [41, 42] and more recently top gates are fabricated on top of an oxide layer.

A schematic side-view of a commonly used overlapping structure [43, 44] is shown in Fig. 2.1(a). Positive voltages are applied to plunger gates (P) to attract electrons beneath them, forming an electric potential well called a quantum dot. Barrier gates (B) influence the ability for electrons to tunnel into or out of the potential well by raising the barrier (with a more negative voltage on B) or lowering the barrier (with a more positive voltage). Reservoir gates sit on either side of the channel and have positive voltages to accumulate the 2DEG, forming the electron reservoir from which electrons can tunnel into the quantum dots. Screening gates sit below most of the length of the plunger and barrier gates in order to suppress any 2DEG accumulation in unwanted regions and protect against spurious quantum dots or leakage channels. A small length of the plunger and barrier gates ($\sim 50 - 100$nm) is left unscreened by the screening gates in order to define and control the quantum dots.

Fig. 2.1(b) shows a schematic of the electric potential wells of two coupled quantum dots, with one electron in the left dot (L) and two electrons in the right dot (R). Tunneling from a reservoir to a quantum dot requires the chemical potential of an energy level (typically the ground state) within the quantum dot to be lower than the fermi level of the reservoir. Conversely, when the chemical potential of an occupied quantum dot is raised above the fermi level of a nearby reservoir, the electron within the quantum dot will empty out into

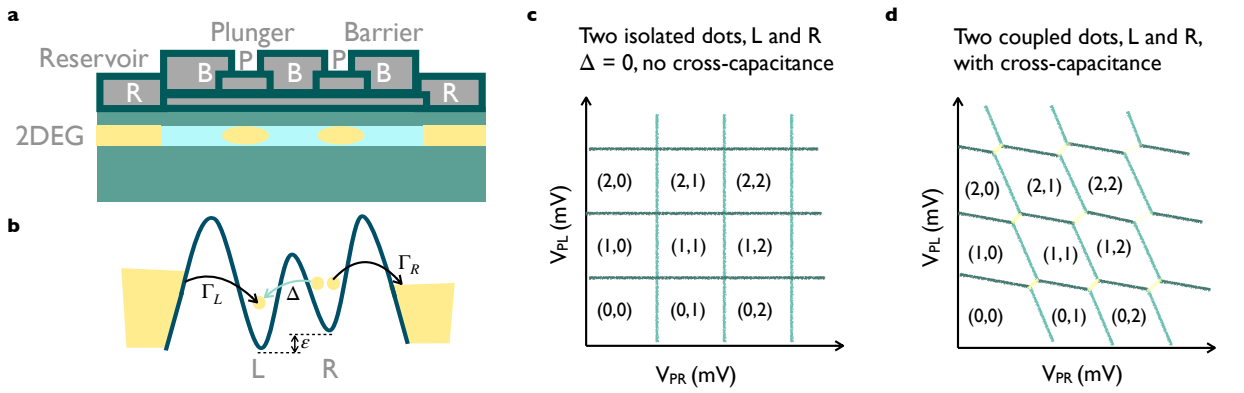

Figure 2.1: (a) Schematic of a semiconducting quantum dot device with overlapping gate architecture, with a DQD formed in the 2DEG. (b) Schematic of a tunnel-coupled, three-electron DQD where each dot has independent tunneling to its own reservoir. $\Gamma_{L,R}$ indicate tunneling to the left and right reservoirs, and Δ indicates tunneling between the quantum dots. (c) A charge stability diagram for two quantum dots under two plunger gates, PL and PR, where $\Delta \to 0$ and there is no cross-capacitance, meaning only voltage changes on the PR gate control the chemical potential of the right dot, and visa versa. This situation is unphysical but helpful to consider first. (d) A similar charge stability diagram, now with realistic cross-capacitance and finite Δ. The cross capacitance is seen in the slopes of the transitions since now voltage changes on both gates PL and PR impact the chemical potential on both dots. The tunnel coupling appears as the introduction of the yellow interdot-transition lines, or polarization lines, indicating movement of an electron between two quantum dots while conserving the total number of electrons in the DQD.

---

the reservoir. The double-dot detuning ε defines the relative difference in chemical potential between the quantum dots. For the case of three shared electrons shown in Fig. 2.1(b), where one quantum dot always has two electrons and the other has one, the charge configuration can either be (2,1) or (1,2) with notation convention (N_L, N_R). When ε is changed such that the chemical potential of L is lower than that of R, the configuration will change from (1,2) to (2,1) with tunnel rate Δ. Thus, by changing the level of a quantum dot's chemical potential, one can control the total number of electrons on the dot. This is done by changing the voltage on the plunger gates above the quantum dots. By sweeping the gate voltages and measuring changes in the electron occupation on the dot, these devices are able to empty the quantum dots and selectively load one electron at a time.

If the system is equipped with a charge sensor, which measures the total amount of charge

on each quantum dot [45–47], or a dispersive readout circuit, which measures movement of electrons within a certain bandwidth [48–50], then measuring these charge sensitive responses while sweeping the gate voltage on the gates which control the respective quantum dot electron occupation will generate a plot called a charge stability diagram. Fig. 2.1(c) shows a schematic of a charge stability diagram in the ideal case where only gate PL (Plunger L) controls the left dot, only gate PR controls the right dot, and there is no tunnel coupling between the two dots. As the voltage on PR V_{PR} is increased, the three vertical lines orthogonal to the V_{PR} axis indicates adding three electrons sequentially into the right dot, and similarly for the three horizontal lines orthogonal to the V_{PL} axis with respect to the left dot. This is enumerated by the coordinates in each rectangular region, so that moving across the plot in Fig. 2.1(c) at constant V_{PL} will bring you from (N_L, 0) to (N_L, 3), etc. However, it is nearly impossible to create devices where voltage changes on one gate, for example PR, do not have any impact on a nearby dot that is not its own, for example the left dot. This influence is called cross-capacitance, and results in transition lines that are not orthogonal to the gate axes but rather slanted at an angle, as shown in Fig. 2.1(d). The dot is typically attributed to the plunger which has the larger influence, the axis with respect to which a transition line is most orthogonal.

Finite tunnel coupling Δ between the left and right quantum dots is included in Fig. 2.1(d) as yellow lines between regions of conserved total number of electrons, for example between (2,1) and (1,2). These lines represent an interdot transition, and are called polarization lines. Polarization lines are essentially equipotential lines; along the polarization line, $\varepsilon = 0$ and electrons are equally likely to be in either charge configuration. The detuning axis is then defined to be orthogonal to the polarization, typically with positive ε favoring the right quantum dot.

More in depth description of quantum dot physics can be found in Refs. [51–53].

2.1.2 Charge, spin, and quantum dot hybrid qubit descriptions

When operating in a device with a tunable electric potential landscape, as described above, there are many different qubit platforms that have been investigated, with varying numbers of quantum dots and electrons. The two most basic types of qubits one could imagine would be a charge qubit and a single spin qubit. A schematic for a charge qubit is shown in Fig. 2.2(a), where the qubit is formed with an electron shared between two coupled quantum dots. The two-level system is then defined by the electron either being in the right quantum dot or the left quantum dot so that $|0\rangle_R = |R\rangle$, $|1\rangle_R = |L\rangle$, and similarly $|0\rangle_L = |L\rangle$, $|1\rangle_L = |R\rangle$. Charge qubits have been experimentally realized [54–56], and are attractive because they require only an ac electric field to drive qubit rotations. However, the energy levels are such that the qubit is highly sensitive to electrical field noise everywhere except the center of the polarization line, where a sweet spot is formed when $\varepsilon = 0$.

Another qubit definition, described in Fig. 2.2(b), is the Loss-DiVencenzo single spin qubit, which requires only one electron in one quantum dot to operate. In this system, a global magnetic field is applied so that the qubit levels are defined by the Zeeman splitting of the electron spin with respect to the global field, $|0\rangle = |\downarrow\rangle$,$|1\rangle = |\uparrow\rangle$. In order to rotate the spin of an electron from one orientation to another, an oscillating magnetic field is required. In addition, for more than one spin qubit it is necessary to be able to address each qubit individually, and therefore have slightly different resonant frequencies; this can be achieved by imposing a magnetic field gradient or tuning different g factors between dots. Such tuning can be achieved in materials with large spin-orbit coupling like GaAs [52] and Ge [57], or through the stark shift [36], with ac magnetic field generated by an ESR line [27, 30]. Alternatively, a micromagnet micromagnet [58, 59] can be used to induce magnetic field gradient. Because there is no charge-like component to this type of qubit, they are less sensitive to charge noise in the system and thus have been proven to be quite coherent [60, 61]. However, the qubit oscillations can be slow as compared with the charge qubit. An in depth comparison of experimental qubit coherence and operation times in semiconducting quantum dots can

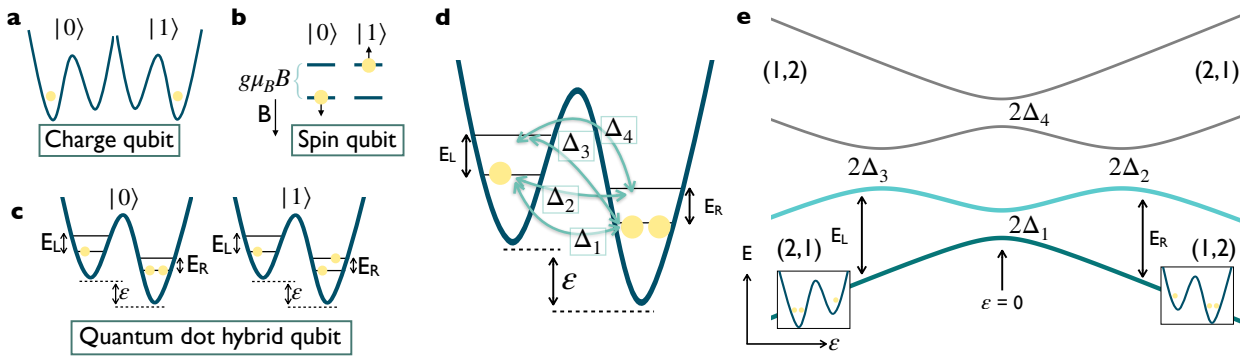

Figure 2.2: (a)Schematic of a charge qubit where a single electron is shared within a DQD. $|0\rangle$ ($|1\rangle$) is defined by the electron being in the left (right) quantum dot. (b) Schematic of a Loss-DiVencenzo single spin qubit, where an electron is in a single quantum dot with an applied magnetic field. $|0\rangle$ ($|1\rangle$) is defined by the spin of the electron being parallel (antiparallel) to the B-field. (c) Schematic of a quantum dot hybrid qubit (QDHQ) which has three electrons shared within a DQD. $|0\rangle$ ($|1\rangle$) is defined by the two electrons in the doubly occupied quantum dot being in a singlet (triplet) state. (d) Schematic showing all of the relevant tunnel couplings in a QDHQ, where tunneling can occur between the two ground states (Δ_1), two excited states (Δ_4), and between ground and excited states ($\Delta_{2,3}$). ε represents the double-dot detuning, the relative difference in chemical potential of the two quantum dots. $E_{L,R}$ are the singlet-triplet splittings in the left and right quantum dots. (e) Eigenvalues of the QDHQ Hamiltonian. The qubit can be formed in the (1,2) configuration, using E_R to define the qubit energy, or the (2,1) configuration, using E_L.

---

be found in Ref. [62].

The final type of qubit described in Fig. 2.2(c-e) is the quantum dot hybrid qubit (QDHQ), which consists of three electrons shared between two coupled quantum dots [33]. With this configuration, the qubit is formed in the doubly occupied quantum dot with the qubit splitting governed by the singlet-triplet splitting. A qubit formed in the (1,2) charge configuration is schematically drawn in Fig. 2.2(c) with qubit levels $|0\rangle_R = |\downarrow\rangle|S\rangle$ and $|1\rangle_R = \sqrt{\frac{1}{3}}|\downarrow\rangle|T_0\rangle$ - $\sqrt{\frac{2}{3}}|\uparrow\rangle|T_-\rangle$ [63]. This qubit is referred to as a "hybrid" qubit because the qubit levels have both charge and spin like components to them, making it a combination of the two types of qubits described in Fig. 2.2(a,b).

The singlet-triplet splitting for a two-electron dot is governed by the lowest excited state energy. In silicon or Si/SiGe devices, that lowest excited state energy is the valley splitting, resulting from silicon's conduction band degeneracy [53]. In Si/SiGe, this value has been

measured to be ∼50-150 μeV [64–70]. In Si-MOS devices, these values can be higher, ∼100-800 μeV [71,72]. In both Si/SiGe and Si-MOS quantum dots, disorder at the interface couples valley states to orbital states, and thus in both cases a more detailed understanding involves considering both degrees of freedom on equal footing [73]. In other material structures where there are no valley splittings, the excited state energy will be decided by the orbital splitting. This energy is directly related to the size and shape of the quantum dot and can typically range from 1-5meV [69, 74]. Though for other types of qubits, like the charge and Loss-DiVencenzo qubits, it is preferred to have excited states high enough in energy to be ignored as compared with the qubit levels, for the QDHQ it is desirable to have the singlet-triplet splitting in an energy regime small enough (∼40 μeV) to address with common microwave electronics. The QDHQ has thus been realized in GaAs devices by tuning the orbital energy small enough as to be accessible [75, 76].

Due to the presence of low-lying excited states in the qubit definition, tunnel rates between all possible states must be considered. This is depicted in Fig. 2.2(d), where tunneling between the two ground states (Δ_1), two excited states (Δ_4), and between ground and excited states ($\Delta_{2,3}$) are shown. In most qubit operations, only Δ_1 and either Δ_2 or Δ_3 will be relevant, depending on the singlet-triplet splitting being used.

Fig. 2.2(e) plots the eigenvalues of the QDHQ Hamiltonian as a function of ε. The qubit levels are the dark ($|0\rangle$) and light ($|1\rangle$) teal lines. There are four anticrossings corresponding to the four different tunnel rates shown in Fig. 2.2(d). Here we can start to see the charge and spin like nature of the QDHQ. Near $\varepsilon = 0$, the ground and excited state energies diverge with opposite slopes. This looks very similar to the energy levels of a charge qubit, and indicates that in this region, the ground and excited states have different charge configurations. At far positive (negative) detuning, the excited state energy level rolls over and becomes parallel with the ground state with energy splitting E_R (E_L). In this regime, both the ground and excited states have the same charge configuration, and the qubit states are entirely spin-based.

The charge-like nature of the qubit allows for qubit operations to be done with only an ac electric field, and no magnetic field or field gradient is required [77]. The spin-like nature of the qubit exhibited by the parallel levels at large ε allows for protection from noise manifested as fluctuations in detuning, as the qubit energy changes very little for small variations in ε. By changing ε, the total amount of charge and spin-like nature of the qubit can be tuned, so that an ac operation can be done at a location with larger charge-like nature, and the qubit can then be adiabatically transformed to a region with smaller charge-like nature to allow for noise protection and greater coherence [78]. These types of sequences will be described in more detail throughout the following chapters.

Since the qubit states can be adiabatically transformed from spin to charge-like, a natural way to read out the qubit state is to map the spin states on the charge states, and measure the charge occupation with a charge sensor. For this to be achieved, the main requirement is that the singlet-triplet splitting in the quantum dot not used for qubit control must be larger than the polarization line-width in order to resolve the charge projection. Looking at Fig. 2.2(e), consider a qubit formed in the right quantum dot, with (1,2) charge configuration. If a qubit operation is done at large positive ε such that the qubit is in the excited state, this state can be transformed by adiabatically lowering ε, through $\varepsilon = 0$, to negative ε in the region where the ground and excited energies are diverging. At this negative value of ε, the ground state of the system is (2,1), and $|0\rangle$ thus has a charge configuration of (2,1), while $|1\rangle$ maintains its charge configuration of (1,2). To get the maximum signal difference between the two qubit states, it is best to have the levels be as charge-like as possible. This makes asymmetric singlet-triplet splittings in the two quantum dots appealing; one dot with a low splitting can be used for qubit operation, and one dot with a large splitting can be used for charge projected readout [33, 75, 76].

2.2 Latched readout of a quantum dot hybrid qubit

The work in this section comprises a manuscript in preparation [79].

As described above, semiconductor quantum dots are a uniquely flexible platform for quantum information, where the combination of spin, charge, and orbital degrees of freedom allows for a variety of qubit architectures [26,80,81]. The quantum dot hybrid qubit (QDHQ) [33, 63] is one such architecture, where fast control is achievable due to the charge degree of freedom, and long coherence times are enabled from the embedded spin encoding in the logical states.

Many previous demonstrations of the QDHQ involve projection of the logical basis onto distinct charge states that are distinguishable by a nearby charge sensing dot [33,75,76]. For example, after manipulation, the logical states $|0\rangle$ and $|1\rangle$ are projected onto the (2,1) and (1,2) charge states, respectively, by adiabatically ramping the detuning of a double quantum dot. In this configuration, the excited charge state (1,2) can decay rapidly [82], setting the required readout bandwidth and making robust readout challenging.

In this Letter, we demonstrate a latched readout process where the excited charge state of a QDHQ is mapped to a tunnel-limited metastable charge configuration, extending the decay time up to 2.5 ms. The QDHQ is operated in the (4,1)-(3,2) charge configuration, and makes use of the (3,1) charge state to perform readout. The 5-electron QDHQ allows for a latched readout window that is larger and more tunable than other 3-electron configurations in silicon, because the size of the readout window is determined by the orbital splitting rather than the valley splitting.

2.2.1 Characterization of the multi-electron orbital splitting in a double-quantum-dot

Fig. 2.3 shows spectroscopic and electrostatic characterization of a 5-electron double quantum dot. Fig. 2.3(a) is a scanning electron miscroscope image of a nominally identical device to

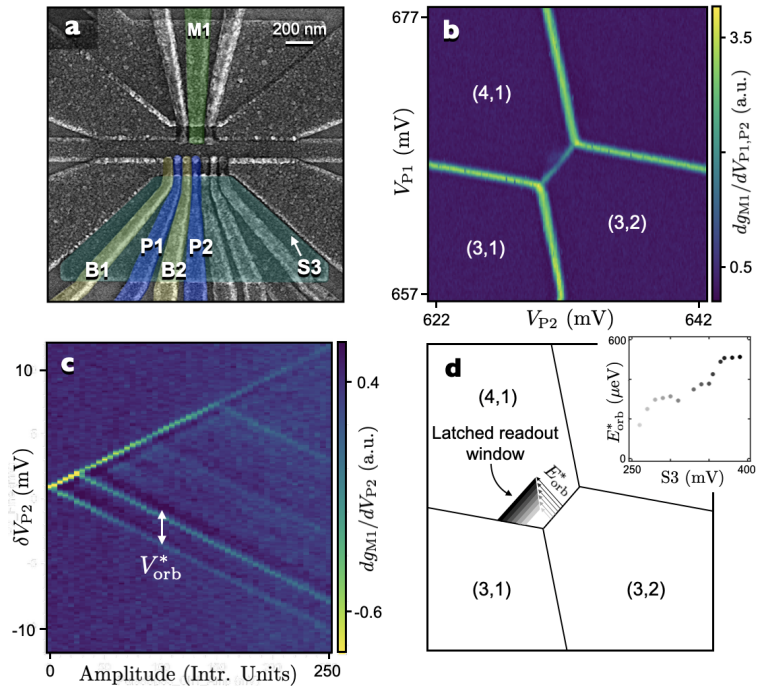

Figure 2.3: (a) False-colored scanning electron microscope image of a nominally identical device. A double dot is configured beneath plunger gates P1 and P2 (blue) near the (4,1)-(3,2) charge anticrossing. Barrier gates B1 and B2 (yellow) are used to control the tunnel coupling in and out of the P1 and P2 dots. (b) Stability diagram of the (4,1)-(3,2) anti-crossing where the 5-electron quantum dot hybrid qubit (QDHQ) is operated. (c) Measurement of the multi-electron orbital splitting (E^*_{orb}) where electron-electron interactions have suppressed the orbital splitting from the single-electron value. (d) Enhanced readout of the 5-electron QDHQ is enabled by using a latched readout scheme. The latched readout window is shown as the colored triangular regimes. The size of the readout window is based off of the multi-electron orbital splitting which is shown to be highly tunable in the inset.

---

the one measured here. The device is fabricated using a three-layer overlapping aluminum gate fabrication process as described in Ref. [83]. Gates that are integral to the experiment are false-colored. The sensor dot M1 is false-colored in green, the two plunger gates defining the double quantum dot are blue, the barrier gates controlling the tunnel rate between the dots and to the electron reservoirs are shown in yellow, and the screening gate S3 which is used to tune the orbital confinement of the dots is teal.

Figure 2.3(b) shows a charge stability diagram of a double quantum dot beneath gates P1 and P2, measured in the (N_{P1}, N_{P2}) $\rightarrow$ (4,1)-(3,2) regime via lock-in amplifier detection. By working in the (4,1)-(3,2) charge configuration, the first excited state in the P1 dot

(containing four electrons) is orbital-like such that two electrons fill the ground and first excited valley state [71,84,85]. Fig. 2.3(c) shows a pulsed-gate spectroscopy measurement of the multi-electron orbital splitting (E^*_{orb}) in the P2 quantum dot, measured to be between approximately 200–500 μeV. This is found to be significantly larger than the valley splitting in the two-electron regime, measured to be between 25–60 μeV [70]. Such small valley splittings would make charge-mapped readout difficult by limiting the window in which the qubit eigenvalues have different charge signatures. By simply adding two electrons to one of the quantum dots, the size of the readout window can be increased in devices where the valley splitting is small.

The multi-electron orbital splitting is also found to be highly sensitive to changes in the screening gate voltages, enabling tunability of the latched readout window. Fig. 2.3(d) shows how the multi-electron orbital splitting relates to the size of the latched readout window. The location of the latched readout window within the charge stability diagram is defined by the region where, simultaneously, the (3,1) charge state is lower in energy than the (3,2) charge state and the (3,2) ground state energy is lower in energy than the sum of the (4,1) ground state energy and the (4,1) multi-electron orbital splitting. This region is shaded gray in Fig. 2.3(d). The gradient of the shaded region is representative of the multi-electron orbital splitting measured at varying electrostatic configurations shown in the inset. Using the screening gate S3, the orbital confinement of a quantum dot can be tuned *in situ* as demonstrated in Ref. [70,86].

2.2.2 Explanation and demonstration of the latched readout regime

Figure 2.4 demonstrates latched readout of a 5-electron QDHQ. Fig. 2.4(a) shows the QDHQ energy eigenvalues, where the green and blue curves are the logical $|0\rangle$ and $|1\rangle$ states, respectively, and the qubit is operated with positive double-dot-detuning (ε) with far-detuned qubit energy given by the singlet-triplet splitting in the right dot (ST_R). After ac or dc manipulation at positive ε, the ε is adiabatically ramped to the latched readout region, shown

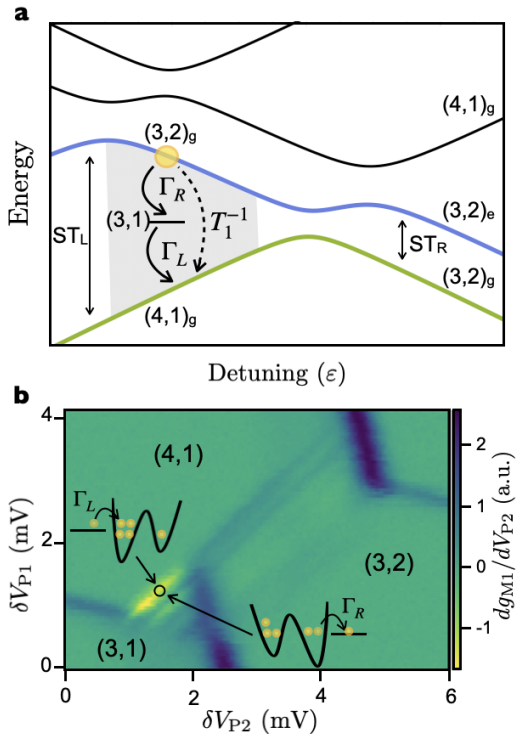

Figure 2.4: Latched readout of a 5-electron quantum dot hybrid qubit (QDHQ). (a) The energy eigenvalues of the qubit, where the logical $|0\rangle$ and $|1\rangle$ states are shown as the green and blue curves, respectively. Latched readout is possible in the gray region as long as the tunnel rate Γ_R is faster than the decay rate from $(3,2)_g$ to $(4,1)_g$. When this condition is met, the (3,2) charge state is latched to the (3,1) charge state. (b) Measured response in the charge sensor with a lock-in tone and Larmor pulse applied to gate P2. The bright yellow response shows enhanced sensitivity in the latched readout regime. When the (3,2) charge state tunnels into the (3,1) configuration, the (3,1) charge state persists until the tunneling process Γ_L occurs. Γ_L can be tuned to be much longer than the decay rate from $(3,2)_g$ to $(4,1)_g$, enhancing the readout signal.

---

shaded in gray. If the qubit is in the logical $|0\rangle$ or $|1\rangle$ state, the resulting charge configuration in the readout regime will be the $(4,1)_g$ or $(3,2)_g$ charge state, respectively. In this way, the logical basis is projected onto a charge basis that can easily be measured via the integrated charge sensing dot. Note that the decay from $(3,2)_g$ to $(4,1)_g$ does not require a spin-flip and is therefore expected to be fast, similar to a charge qubit [56, 82, 87, 88].

By incorporating a latching mechanism, enhanced readout is achieved, as demonstrated in Fig. 2.4(b) using lock-in detection. In Fig. 2.4(b), the double dot is initialized in the $(4,1)_g$ state by waiting within the the latching regime. Then, a Larmor pulse is applied,

diabatically pulsing the detuning to the polarization line where the Hamiltonian suddenly changes, populating the logical $|1\rangle$ excited state. After the Larmor pulse time, the detuning is pulsed back into the (4,1) charge configuration. The fringes both within and outside of the latched triangular region in Fig. 2.4(b) are indicative of Larmor oscillations resulting from the applied pulse. When the readout position lies within the latched readout regime, the charge-sensed signal is enhanced [54, 89], as observed by comparing the bright yellow fringes within the latched triangle to the blue ones outside the triangle in Fig. 2.4(b). Since the charge sensor is more sensitive to changes in total number of electrons, the capacitive shift for changes from (3,2) to (3,1) is larger than from (3,2) to (4,1).

In order for the latching mechanism to work successfully, the tunnel rate from $(3,2)_g$ to $(3,1)_g$, denoted as Γ_R in Fig. 2.4, must be faster than the decay rate from $(3,2)_g$ to $(4,1)_g$ ($\Gamma_1 = T_1^{-1}$). Once this condition is met, the latching time can be tuned *in situ* by changing the tunnel rate from $(3,1)_g$ to $(4,1)_g$, denoted as Γ_L in Fig. 2.4.

2.2.3 Measurement of tunnel rates which meet the latched readout requirements

Fig. 2.5 shows measurement of Γ_L and Γ_R at a single electrostatic tuning that is well suited for latched readout. For $\Gamma_L = \Gamma_{L1} + \Gamma_{L2}$ there are two tunneling processes that contribute: the tunnel rate from the reservoir to the left of the P1 quantum dot (Γ_{L1}) and the cotunneling rate from the right reservoir (Γ_{L2}). Each of these tunnel rates are individually measured using real-time detection of single electron tunneling events in and out of the P1 quantum dot. A single time trace is taken where the position of the excess electron is mapped out in real time by measuring the current through the charge sensor. Fig. 2.5(a) shows a sample trace for 10 seconds where the higher (lower) current corresponds to the excess electron off (on) the dot. The amount of time spent off the dot between each tunneling event is binned and plotted in Fig. 2.5(b) as red squares. The data is then fit using the results from Ref. [90] and plotted as the black line. From the fit, a tunnel rate of $\Gamma_{L1} = 6$ Hz is extracted.

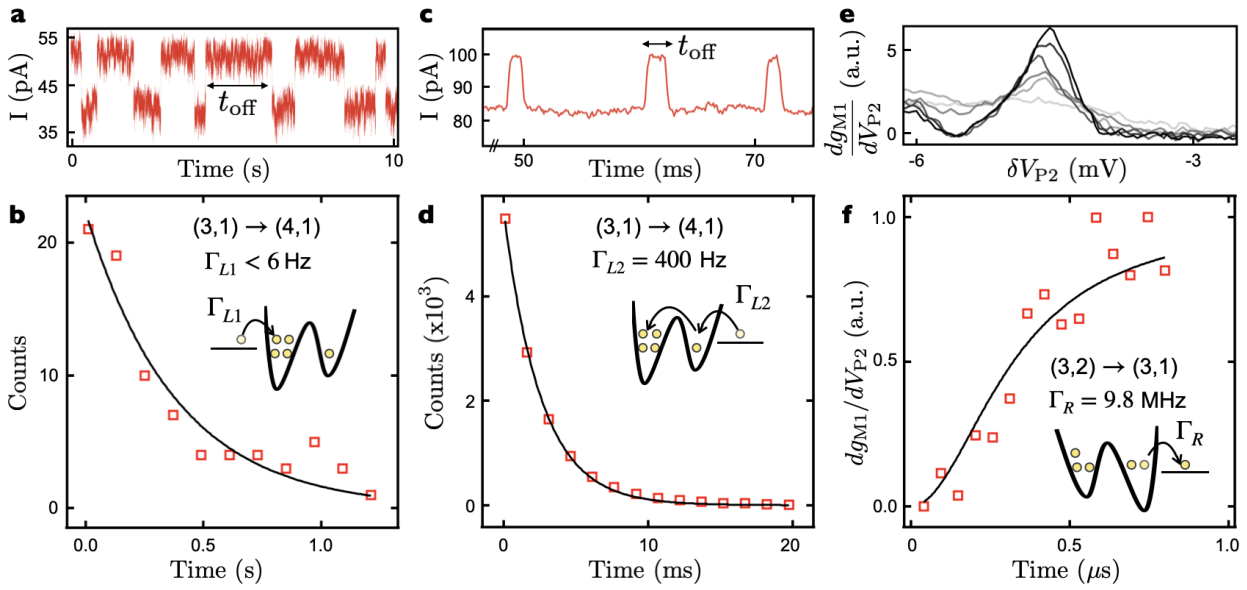

Figure 2.5: Measurement of tunnel rates Γ_R and Γ_L. (a, b) The tunnel rate between the left reservoir and P1 dot (Γ_{L1}) is measured by real-time detection of single electron tunneling events and binning the amount of time the electron spends off the dot. The result is fit to the black line, yielding a tunnel rate of less than 6 Hz. (c, d) The same technique is used to measure the cotunneling rate from the gate reservoir into the P1 dot (Γ_{L2}), where a faster tunnel rate of 400 Hz is measured. Thus, the tunnel rate from the left reservoir into the P1 dot is negligibly slow. (e, f) At the same electrostatic tuning, Γ_R is measured to be 9.8 MHz. This is determined by applying a lock-in tone and a square pulse to gate P2 and measuring the peak height of the lock-in response as a function of the square pulse frequency. Γ_R is purposefully made to be much faster than the other rates so that the tunneling event from $(3,2)_g$ to $(3,1)_g$ occurs before the $(3,2)_g$ to $(4,1)_g$ decay. The fast Γ_R causes the cotunneling rate Γ_{L2} to be the dominant process for the tunneling process Γ_L.

A similar procedure is used for extracting Γ_{L2}, as shown in Fig. 2.5(c, d). Here, instead of direct tunneling, cotunneling is the dominant process, yielding a cotunneling rate of $\Gamma_{L2} =$ 400 Hz. The direct tunneling rate from the left reservoir is purposefully made to be much slower than the cotunneling rate by lowering the voltage on gate B1. This maximizes the latching time, which for this electrostatic tuning is 2.5 ms.

The cotunneling rate is affected by both the interdot tunnel rate t_c and the tunnel rate from P2 into the right reservoir (Γ_R) [91]. The double dot system is set at an electrostatic tuning that is realistic for QDHQ operation with a tunnel coupling of several GHz and a Γ_R that is set to be fast such that it is comparable to the decay rate Γ_1. Fig. 2.5(e, f) shows

the results of measuring Γ_R. A lock-in tone and square pulse at frequency f_p are applied to gate P2 while measuring the amplitude of the lock-in signal as a function of the square pulse frequency. This procedure is discussed in greater detail in Ref. [92]. The peak heights are normalized and plotted as red squares in Fig. 2.5(f) as the pulse time $\tau_p = 1/2f_p$ is varied. The data is fit and shown as the black line, yielding $\Gamma_R = 9.8$ MHz. Given these values, single-shot readout of the QDHQ is possible in the future due to the long latching time of 2.5 ms.

2.2.4 AC manipulation of a QDHQ read out using the latched scheme

Fig. 2.6 shows resonant microwave control of the 5-electron QDHQ using lock-in measured latched readout. In Fig. 2.6(a), a stabilty diagram is measured with a Rabi pulse applied as pictured in the right-hand-side inset. With this pulse, the double quantum dot is initialized in the $(4,1)_g$ state and the detuning is adiabatically ramped into the $(3,2)_g$ charge regime. A resonant microwave burst is applied for a time t_{Rabi}, populating the logical $|1\rangle$ state of the QDHQ. The detuning is adiabatically ramped back into the $(4,1)_g$ configuration, where the latching mechanism occurs by tuning the $(3,2)_g$ to $(3,1)_g$ tunnel rate to be faster than the $(3,2)_g$ to $(4,1)_g$ decay rate. When this condition is met, enhanced readout is possible, shown as the yellow triangular region in Fig. 2.6(a). The bright diagonal line within the triangle indicates the location in detuning where the applied microwave is resonant with the qubit energy.

Figure 2.6(b,c) shows Rabi and detuned Ramsey oscillations measured using latched readout. The Rabi measurement in Fig. 2.6(b) is performed by sweeping both the length of the microwave drive and the position of the pulse sequence within the latched window, governed by δV_{P2}. In Fig. 2.6(c), Ramsey fringes are observed in the presence of the pulse sequence shown in the inset. Here, two $\pi/2$ microwave bursts are separated by a dc detuning pulse, which allows for efficient measurement of the characteristic Larmor oscillation frequency as

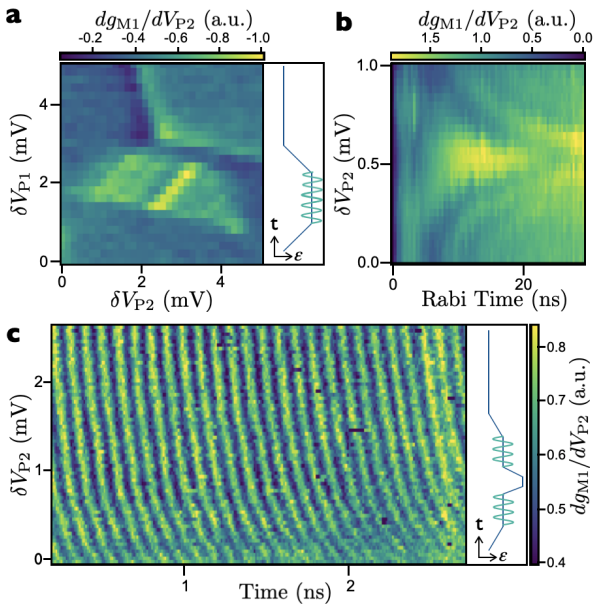

Figure 2.6: Microwave-driven QDHQ using latched readout. (a) Latched readout zone with a Rabi pulse applied, as shown in the Inset. The applied pulse height and microwave drive are chosen to match the qubit energy at a location in positive detuning, and the latched signal appears as a bright line within the triangular region. (b,c) Rabi and detuned Ramsey oscillations driven with microwave frequency 10 GHz. The Inset in (c) shows the Ramsey pulse sequence where two $\pi/2$ microwave bursts are separated by a dc detuning pulse.

---

a function of detuning [78,93]. The frequency of the microwave drive for both measurements is 10 GHz. The oscillations seen in Fig. 2.6(c) are measured as a function of the dc detuning pulse height and the wait time t_{Ramsey} at the top of the pulse. The parallel oscillations as a function of increased δV_{P2} are characteristic of the asymptotic qubit energy of a QDHQ at high detuning.

In summary, here we identify and experimentally measure key parameters necessary for achieving latched readout, and demonstrate latched readout of a 5-electron QDHQ. The tunnel rate from $(3,2)_g$ to $(3,1)_g$ is tuned to be faster than the $(3,2)_g$ to $(4,1)_g$ decay rate, and the direct tunnel rate from $(3,1)_g$ to $(4,1)_g$ is tuned to be slower than the cotunneling rate. These findings provide an important development for readout of QDHQs: the latched state persists much longer than that of a typical charge-mapped QDHQ excited state, providing a path for single-shot readout in the future. Additionally, cotunneling allows for latched

readout of the QDHQ with only a single reservoir. Future implementations of QDHQs may use this readout architecture for multi-qubit operation and readout.

Research was sponsored in part by the Army Research Office (ARO) under Grant Numbers W911NF-17-1-0274 and by the Vannevar Bush Faculty Fellowship program under ONR grant number N00014-15-1-0029. JC acknowledges support from the National Science Foundation Graduate Research Fellowship Program under Grant No. DGE-1747503 and the Graduate School and the Office of the Vice Chancellor for Research and Graduate Education at the University of Wisconsin-Madison with funding from the Wisconsin Alumni Research Foundation. We acknowledge the use of facilities supported by NSF through the UW-Madison MRSEC (DMR-1720415) and the NSF MRI program (DMR-1625348). The views and conclusions contained in this document are those of the authors and should not be interpreted as representing the official policies, either expressed or implied, of the Army Research Office (ARO), or the U.S. Government. The U.S. Government is authorized to reproduce and distribute reprints for Government purposes notwithstanding any copyright notation herein.

Chapter 3

Tunability of quantum dot hybrid qubit energy levels

This chapter focuses on the energy level structure and energy level dispersion of the quantum dot hybrid qubit (QDHQ), and their dependence on parameters like the double-quantum-dot tunnel coupling or on the presence of other nearby levels. The chapter begins by describing the energy eigenvalues of the QDHQ, and the importance of both the energy dispersion and curvature on qubit performance and operation. Next, the dependence of QDHQ dispersion and curvature on tunnel coupling is explored, discussing different regimes of operation and presenting Ramsey measurements at different tunings. Finally, an additional energy level is added to the QDHQ, and its impact as a function of tunnel coupling on the energy dispersion is presented.

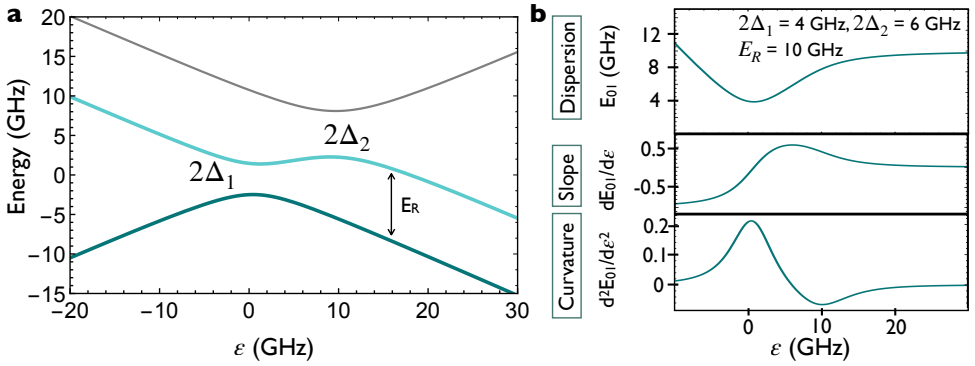

Figure 3.1: (a) Energy eigenvalues versus detuning of a quantum dot hybrid qubit operated in the right quantum dot, as seen in Fig. 2.2(e). (b) Energy dispersion, slope, and curvature for the QDHQ, the two lowest energy eigenvalues in (a).

3.1 Dependence of the quantum dot hybrid qubit dispersion on tunnel coupling

3.1.1 Quantum dot hybrid qubit dispersion and curvature

As discussed in the previous chapter, a major advantage of the quantum dot hybrid qubit (QDHQ) is the hybridization of the qubit states between different charge states ((2,1) and (1,2)) and different spin states ($|S\rangle$ and $|T\rangle$). This hybridization allows for adiabatic transformation of the qubit between a dominantly charge-like region to a dominantly spin-like region in order to benefit from the advantages of each. The charge and spin-like regions can be seen by examining the ground and excited state levels in Fig. 3.1(a), colored as dark and light teal, respectively. At negative ε, the levels diverge exactly like those of a charge qubit. At large positive ε, the states become parallel, indicating the two levels have the same charge configuration and are entirely spin-like.

It is useful to discuss the detuning-dependent changes in qubit energy and how they impact the spin and charge-like nature. Fig. 3.1(b) shows the qubit dispersion, the energy difference $E_{01} = E_1 - E_0$ between the two qubit energy eigenvalues, for the energy eigenvalues shown in Fig. 3.1(a) with Hamiltonian parameters $2\Delta_1 = 4$ GHz, $2\Delta_2 = 6$ GHz, and $E_R =$

10 GHz. It is straightforward to map the dispersion in Fig. 3.1(b) onto the energy eigenvalues in Fig. 3.1(a): near $\varepsilon = 0$, the qubit levels have an anticrossing with splitting $2\Delta_1$, so there will be a dispersion minimum at $\varepsilon = 0$. For negative ε, the energy eigenvalues diverge at a constant rate so that the qubit energy increases linearly. Finally, for large positive ε, the eigenvalues become parallel with separation E_R. This means that as ε is increased, the qubit energy will asymptote to E_R, creating an increasingly flat energy dispersion.

Plotted below the dispersion in Fig. 3.1(b) is the slope of the dispersion and curvature of the dispersion. The slope of the dispersion, $\frac{dE_{01}}{d\varepsilon}$, is the quantity which determines how sensitive the qubit is to noise-induced fluctuations in ε. If the slope is small, the qubit energy changes very little in the presence of fluctuations in ε, so that the qubit will stay approximately in resonance to an applied microwave drive meant to drive the qubit at some frequency f_R. This will result in higher coherence as compared to a tuning with higher $\frac{dE_{01}}{d\varepsilon}$.

Looking at the slope in Fig. 3.1(b), changes from negative to positive ε result in changes of $\frac{dE_{01}}{d\varepsilon}$ from negative to positive, as expected for local minimum. As the dispersion approaches the far-detuned value of E_R, the slope asymptotes to 0. For a QDHQ dispersion, there are two regions where $\frac{dE_{01}}{d\varepsilon} \to 0$ and the qubit is insensitive to charge noise; a localized "sweet spot" at $\varepsilon = 0$ and an "extended sweet spot" at far detuning. The extended sweet spot is investigated extensively in Ref. [78] where the decoherence rate is shown to be directly proportional to the dispersion slope and charge noise σ_ε. This demonstrates the benefit of tuning ε to regions with less charge-like nature (indicated by lower $\frac{dE_{01}}{d\varepsilon}$).

The curvature of the dispersion is the second derivative with respect to ε, $\frac{d^2(E_{01})}{d\varepsilon^2}$. Where the slope of the dispersion describes how insensitive the qubit is to external factors like noise, the curvature of the dispersion is an important characteristic to describe how strongly the qubit can couple to other nearby qubits or resonators. This is because the curvature relates to how easy it is to polarize electrons like a dipole within the quantum dots, and a primary way proposed of coupling to a QDHQ is through capacitive, dipolar coupling [88,94,95]. The curvature has finite value at the charge anticrossings where the qubit states are hybridized

across multiple charge states (i.e. (2,1) and (1,2)), and goes to zero in regions where the qubit states each have unique charge states regardless of whether those charge states are the same (at positive detuning in Fig. 3.1(a)) or different (at negative detuning in Fig. 3.1(a)). Note how at $\varepsilon = 0$, $\frac{dE_{01}}{d\varepsilon} = 0$ but $\frac{d^2(E_{01})}{d\varepsilon^2}$ is maximized; this is called a 'first order sweet spot', and is what allows charge qubits to couple strongly to each other and to resonators right at $\varepsilon = 0$ [96–99]. Higher-order sweet spots are also possible, if higher-order derivatives are also zero such as in Ref. [100].

.

3.1.2 Dependence on tunnel couplings

For a fixed electrostatic tuning of the quantum dots and therefore fixed tunnel couplings $\Delta_{1,2}$, ε can be chosen to optimize for desired coherence properties (small slope) or coupling properties (large curvature). However, if $\Delta_{1,2}$ are not optimized, even the best choices of ε may not be sufficient. So, it can be useful to understand how changing the tunnel couplings impact the qubit dispersion and its derivatives. Note that while variation in the ratios between $\Delta_{1,2}$ can be observed when changing the double dot tunnel coupling, independent control of Δ_1 and Δ_2 has not yet been demonstrated at the time this thesis was written.

Figure 3.2 describes how changing $\Delta_{1,2}$ can impact the qubit dispersion. In Fig. 3.2(a), three dispersions are shown for $2\Delta_1$ ranging from 2 GHz to 6 GHz with $2\Delta_2 = 2$ GHz and $E_R = 10$ GHz. Increasing Δ_1 clearly results in an increased minimum energy at $\varepsilon = 0$ and a rounder dispersion around that minimum. This roundness will result in a larger region of charge noise protection around $\varepsilon = 0$. Fig. 3.2(b) shows a similar analysis, now holding $2\Delta_1 = 2$ GHz and changing Δ_2. Here the minimum is unaffected, and instead it is the roll-over towards the asymptotic region that changes. At higher values of Δ_2, the asymptote is more gradual. This means there is a larger region at lower values of ε with lower $\frac{dE_{01}}{d\varepsilon}$, which will have higher coherence properties than a pure charge qubit. However, this comes at the cost of the asymptotic limit, which now is not reached until larger ε.

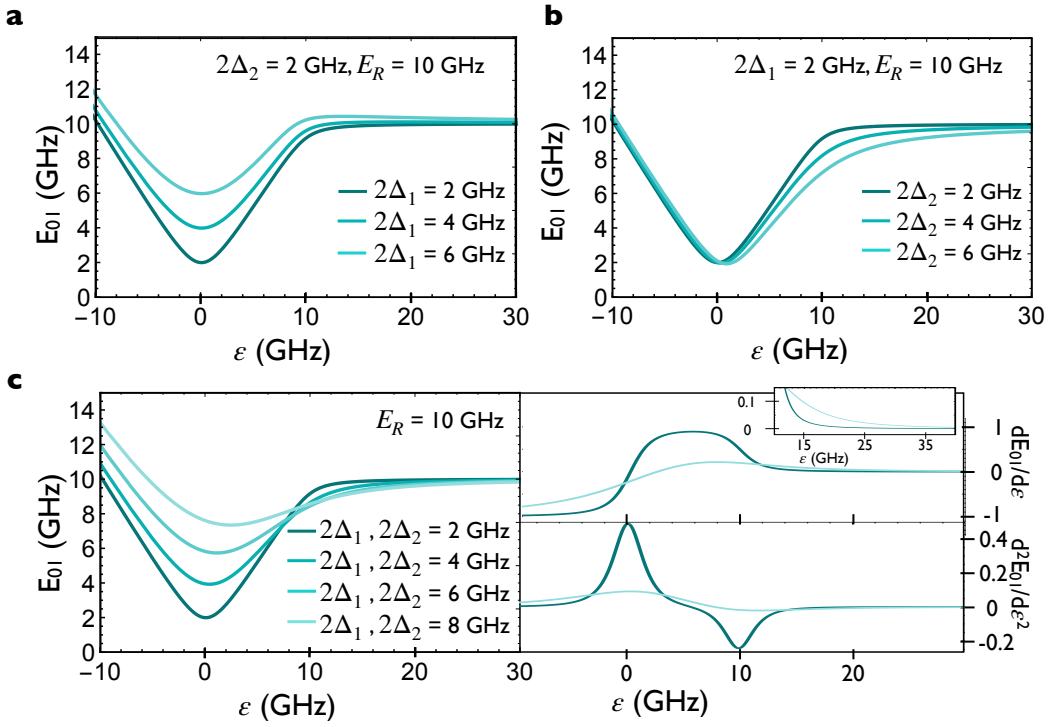

Figure 3.2: (a) QDHQ energy dispersion as a function of ε with $2\Delta_2 = 2$ GHz and $E_R = 10$ GHz, for $2\Delta_1 = 2$-6 GHz. Changes in Δ_1 lead to changes in the dispersion minimum. (b) QDHQ dispersion with now $2\Delta_1 = 2$ GHz for $2\Delta_2 = 2$-6 GHz. Changes in Δ_2 lead to changes in the roll-over and how quickly the qubit energy asymptotes towards E_R. (c) QDHQ dispersion, still fixing $E_R = 10$ GHz, with $2\Delta_1 = 2\Delta_2 = 2$-8 GHz. At higher values of $\Delta_1 = \Delta_2$, the qubit energy changes less rapidly and over a smaller range. This is exemplified in the slope ($\frac{dE_{01}}{d\varepsilon}$) and curvature ($\frac{d^2E_{01}}{d\varepsilon^2}$) plotted in the inset, comparing $2\Delta_1 = 2\Delta_2 = 2$ GHz and 8 GHz.

Figure 3.2(c) shows the qubit dispersion for $2\Delta_1 = 2\Delta_2 = 2$ to 8 GHz, with $E_R = 10$ GHz. Though it is not required or expected for the two tunnel couplings to be identically equal, these plots show how the dispersion will generally change with increasing tunnel couplings. In particular, as $2\Delta_1$, $2\Delta_2 \to E_R$, the minimum will approach the asymptotic limit and the dispersion will become much flatter. The insets of Fig. 3.2(c) show the slope and curvature of dispersions with $2\Delta_1$, $2\Delta_2 = 2$ GHz (dark teal) and $2\Delta_1$,$2\Delta_2 = 8$ GHz (light teal). When comparing the slopes, it becomes clear that though the light line with $2\Delta_{1,2} = 8$ GHz has a lower value for a wider range, the dark line approaches the 0 slope limit at least 15 GHz lower in detuning. Similarly, the curvature for the light line has a finite value over a wider

range, but has a peak value of around 5 (10) times smaller than the dark line at $\varepsilon = 0$ (10) GHz.

3.1.3 Implications for one and two-qubit operations

Single and two-qubit manipulation of the QDHQ have to be peformed at a location in detuning with finite curvature. For single-qubit manipulation, this is because ac driving of the QDHQ is made possible through virtual tunneling events [63], and this driving strength is therefore dependent on the amount of charge-like nature present in the qubit states. This transition becomes increasingly difficult to drive at more positive detuning when the qubit states become entirely spin-like, and the two levels have the same charge configuration. For two capacitively coupled QDHQs, the strongest qubit coupling occurs at the point of highest curvature [94]. Thus, the plots in Fig. 3.2(c) exemplify two conflicting modes of operation; optimal but localized coherence and coupling, or wide-range but suboptimal coherence and coupling.

For the former, the system would start in the region of high curvature for ac manipulation or two-qubit coupling, and the qubit state would then be adiabatically transformed to the $\frac{dE_{01}}{d\varepsilon} \rightarrow 0$ region to evolve with maximum protection from charge noise. Since the region with optimal curvature also has a large slope, the system will be quite sensitive to charge noise during ac manipulation, and as it adiabatically traverses through detuning. For the latter, ac driving and two-qubit coupling is possible over a much larger range; however, the coupling strength is small over this range and is accompanied by a relatively large slope. To compare quantitatively, for equal slopes of the light(high tunnel coupling) and dark(low tunnel coupling) lines of $\frac{dE_{01}}{d\varepsilon} = 0.158$ at $\varepsilon = 11.67$GHz , the curvature of the dark line is nearly 5 times larger (-0.1 compared -0.02). Additionally, for equal curvatures of -0.017 at ε = 14.26GHz, the slope of the dark line is 2.5 times smaller (0.04 compared to 0.1).

A third operational option would be to adiabatically tune the tunnel coupling as opposed to the detuning. For fixed detuning, the tunnel coupling could be increased or decreased to

switch between a highly coupled, manipulation state and a highly coherent isolation state. Based on Fig. 3.2, and depending on the coupling strength required, the optimal tuning for these two states may be a high tunnel coupling state (for manipulation) and low tunnel coupling state (for coherence). This is not an intuitive solution, as the high-tunnel coupling dispersion on average seems flatter and therefore would have better coherence properties. However, the low-tunnel coupling dispersion allows for lower slope (higher coherence) at lower double dot detuning, which is easier to obtain experimentally. Thus, a possible experimental procedure would be to sit at the location in detuning with the best coherence properties and then increase the tunnel couplings just enough to allow for ac driving or two-qubit coupling at that location before decreasing the coupling again for state evolution.

Theoretical description and investigation of operating regimes for one and two QDHQs coupled to a superconducting reservoir, related to the above discussions, can be found in Ref. [101].

3.1.4 Experimental measurement of different dispersions

The detuned Ramsey pulse sequences described in Chapters 2,4, and [78] are an efficient way to probe the Hamiltonian parameters for the QDHQ. The pulse sequence results in Ramsey oscillations at the characteristic frequency corresponding to the qubit energy as a function of detuning. Thus, one can fit the data for the frequency of the oscillations, and then fit those frequencies as a function of detuning for the qubit dispersion parameters ($\Delta_{1,2}$, E_R). Detuned Ramsey data at three different device tunings are shown in Fig. 3.3. Fig. 3.3(a,c,e) shows 2d data plots of the Ramsey measurements, where the x-axis is wait time between adiabatic ramps and the $\pi/2$ microwave pulses, and the y-axis is amplitude of the dc-detuning ramp. The point where amplitude = 0 indicates where the amplitude of the dc-detuning ramp switches from positive to negative; this is the location in detuning where the qubit is resonant with the applied microwave drive frequency. The amplitude values shown here are the instrument values before any insertion loss or attenuation. Fig. 3.3(b,d,f)

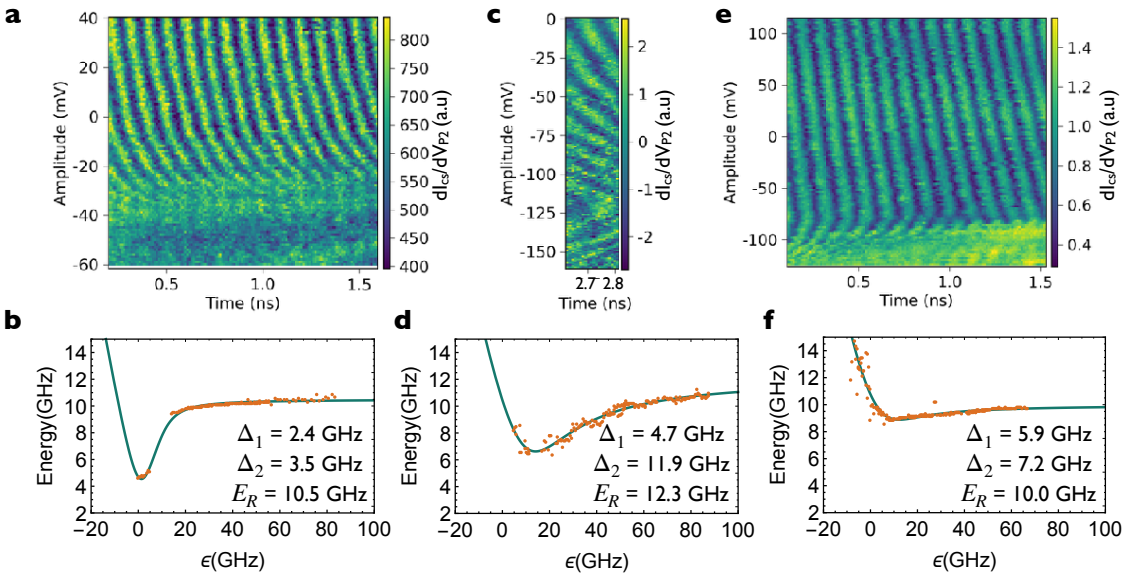

Figure 3.3: Extracted dispersions and Ramsey data at 3 different tunings, reflected in the three different combinations of Δ_1, Δ_2, and E_R. (a,c,e) are Ramsey measurements and (b,d,f) are extracted by fitting data in (a,c,e) for the frequency of oscillations at each point in amplitude.

---

show points extracted from Fig. 3.3(a,c,e) by fitting the 2d data at every point in amplitude for the frequency of oscillation. These points are then plotted and fit to using the QDHQ eigenvalues to extract the Hamiltonian parameters.

Figure 3.3(a,b) shows the 2d Ramsey data and extracted frequency points at a tuning with low tunnel couplings with respect to E_R. This can be seen in the 2d data by the fact that the oscillations are highly coherent above around -30 mV in amplitude but are non-existent below that point. Additional Larmor measurements were taken at this tuning which confirmed the characteristic oscillations at $E_R = 10$ GHz, and indicated charge qubit oscillations at the dispersion minimum of around 5 GHz. To align oscillations at the minimum and at the asymptotic QDHQ limit, a detuned Ramsey measurement was performed with a diabatic dc ramp. This was effectively a Ramsey-Larmor hybrid measurement, and resulted in faint oscillations of $\sim$5 GHz at the dispersion minimum, in agreement with the other Larmor measurements taken. The additional data is included in Sec. 6.1.

The transition from Fig. 3.3(a,b) to Fig. 3.3(c,d) and Fig. 3.3(e,f) occurred after small

subsequent changes in the barrier gate that controls the tunnel coupling between the two quantum dots. This can be seen in Fig. 3.3(c) by the presence of oscillations through the dispersion minima, as opposed to the rapid dephasing of oscillations seen in Fig. 3.3(a). Note that in the data shown in 3.3(c) the SNR of the oscillations gets worse after around -50mV in the dc-detuning pulse amplitude. In fact, in order to resolve the oscillations, a background signal was subtracted at every point in time to remove a dephased response to the two $\pi/2$ microwave pulses. This low signal is consistent with the slope of the dispersion in Fig 3.3(d) being nontrivial throughout the majority of the investigated detunings, as compared with the far positive ε slope in Fig 3.3(b).

The data in Fig. 3.3(e,f) by comparison is quite coherent through the dispersion minimum, and only loses coherence rapidly at negative detunings past $\varepsilon = 0$ where the qubit is effectively a charge qubit. This coherence can be attributed to the flat nature of the dispersion for a large range of detunings, as seen in Fig. 3.3(f). This dispersion allows for coherent, two-axis (Rabi and Ramsey) control at virtually every point in positive detuning past $\varepsilon = 0$, but would likely come at the cost of a lower coupling strength to other qubits or long-range coupling mechanisms like resonators.

3.2 Impact of additional levels on dispersion

3.2.1 Expansion of QDHQ Hamiltonian

The sections above describe how changing the tunnel coupling can tune the qubit energy dispersion of the QDHQ. However, similar changes can also occur due to the presence of other states lower in energy than the energy splitting of interest. Such nearby states can be brought about due to strong electron-electron interactions in the doubly occupied quantum dot, and will be discussed in detail in the following chapter. The last portion of this chapter will describe how the addition of extra levels to the QDHQ Hamiltonian can influence the energy dispersions.

The reduced QDHQ Hamiltonian, where only one singlet-triplet splitting (here choosing to use the one in the right dot) is considered and the other (in the left dot) is assumed to be large is as follows:

$$H = \begin{pmatrix} \varepsilon/2 & \Delta_1 & \Delta_2 \\ \Delta_1 & -\varepsilon/2 & 0 \\ \Delta_2 & 0 & -\varepsilon/2 + E_R \end{pmatrix}, \tag{3.1}$$

with axes, in the (2,1)-(1,2) configuration, taken as S(2,1), S(1,2), T(1,2). If instead there are two possible excited states in the (1,2) configuration which are each only coupled to S(2,1) and not to any (1,2) states, there will simply be another tunnel coupling term and energy term in the Hamiltonian. Since this new excited state is not necessarily a triplet state, it will be referred to here as E2(1,2), with energy separation from the ground state E_{R2}. The amended Hamiltonian is:

$$H_2 = \begin{pmatrix} \varepsilon/2 & \Delta_1 & \Delta_2 & \Delta_3 \\ \Delta_1 & -\varepsilon/2 & 0 & 0 \\ \Delta_2 & 0 & -\varepsilon/2 + E_{R1} & 0 \\ \Delta_3 & 0 & 0 & -\varepsilon/2 + E_{R2} \end{pmatrix}, \tag{3.2}$$

with axes S(2,1), S(1,2), T(1,2), E2(1,2). More complicated systems may include coupling terms between (1,2) energy levels, but this simplified Hamiltonian is enough to start to explore the energy landscape of a QDHQ-like multi-level system.

3.2.2 Dependence on ground and excited state dispersions on tunnel coupling

Similar to Fig. 3.2, this section will address how changes in the double quantum dot tunnel couplings can impact the energy dispersions. Note that the ground state dispersion, which describes transitions from $|0\rangle$ to $|1\rangle$ behaves the same as a function of tunnel couplings Δ_{1-3}

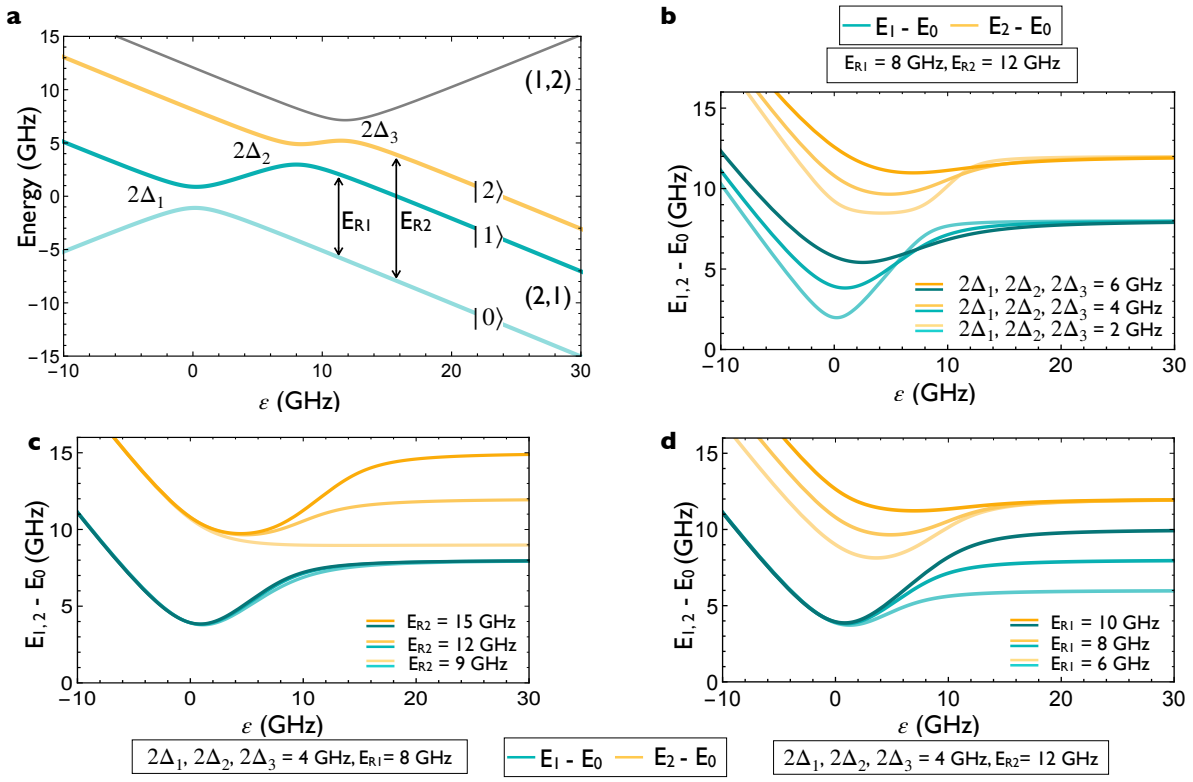

Figure 3.4: (a) Energy level diagram of a double quantum dot at the QDHQ charge regime (ie (2,1)-(1,2)) with two excited states in the right QD coupled to the left QD and not coupled to each other. This system now has three relevant tunnel couplings Δ_{1-3}, and two energy levels accessible from the ground state, with asymptotic energies E_{R1} and E_{R2}. (b) Difference between the ground and first (second) excited state plotted in teal (yellow) as a function of tunnel couplings with all three couplings set equal. (c) Difference between the ground and first (second) excited state plotted in teal (yellow) as a function of E_{R2}. (d) Difference between the ground and first (second) excited state plotted in teal (yellow) as a function of E_{R1}.

---

as in the single excited state case of Eq. 3.1. That is, it has no apparent dependence on Δ_3 or E_{R2}. However, the excited state dispersion, described by transitions from $|0\rangle$ to $|2\rangle$, does not behave as it would if described by Eq. 3.1. It instead is impacted by all the tunnel couplings. If E_{R2} and $\Delta_{1,2}$ are large enough such that the excited state dispersion can be ignored, then the ground state dispersion will operate as normal. This of course makes sense, because these systems always have orbital levels that are much larger, but which are not seen in microwave spectroscopy or qubit experiments. However, if the singlet-triplet splitting

is smaller than expected, it is possible to assume an excited state dispersion is the lowest energy dispersion and that is should behave as such as a function of tunnel coupling. This section is meant to highlight the differences in behavior with one extra level; note that this analysis can be expanded to even more levels as seen in the next chapter.

Figure 3.4(a) shows an energy level diagram for the Hamiltonian in Eq. 3.2, where the ground (first excited) state is colored light (dark) teal and the additional excited state is colored yellow. In this case, there will be two relevant qubit dispersions: the energy difference between $|0\rangle$ and $|1\rangle$ and the energy difference between $|0\rangle$ and $|2\rangle$. Examples of these dispersions for various Hamiltonian parameters are shown in Fig. 3.4(b,c). Fig. 3.4(b) shows the ground (excited) state dispersions in teal (yellow), with fixed E_{R1} and E_{R2} values of 8 and 12 GHz, respectively. The tunnel couplings $2\Delta_{1-3}$ are all set to be equal for simplification and changed from 2-6 GHz. Note how at $2\Delta_{1-3} = 2$ GHz, the excited state dispersion has a trapezoidal shape near $\varepsilon = 0$ with a plateau as opposed to a minimum; this is due to the location of the $\Delta_{1,2}$ anticrossings. The Δ_1 anticrossing determines the change from a linearly increasing energy to a minimum-like energy. Then, for the detuning range between the Δ_1 anticrossing and the Δ_2 anticrossing, $|2\rangle$ and $|0\rangle$ are actually parallel, causing the energy plateau. Finally, the Δ_2 anticrossing starts the dispersion's increase towards E_{R2} before Δ_3 causes an energy rollover.

An additional result to notice is how flat the excited state energy dispersion is when $2\Delta_{1-3} = 6$ GHz, particularly for an asymptotic energy of $E_{R2} =$ 12GHz. As seen above in Fig. 3.2(c), a traditional QDHQ energy dispersion becomes flat when $2\Delta_1$ and $2\Delta_2$ are a large fraction of the singlet-triplet splitting (typically 70-80%). What is seen in Fig. 3.4(b) is that flatness of an energy dispersion can be generated with smaller tunnel couplings with respect to the energy splitting (50% in this example), if there is an additional energy level below the level in question. These results raise the question of whether the flat dispersion seen in Fig. 3.3(e,f) was produced simply from tunnel coupling tuning or because of the presence of one or more low-lying energy levels. Though there is no concrete answer, the

data shown in the following chapter (taken in the same device at nearly identical tuning) argue that indeed extra levels helped attain such a flat dispersion. The presence of excited states to induce flat dispersions can be a useful tool if the states are well isolated; the data taken at the tunings in Chapters 2 and 4 had lower coherence times than expected for the dispersion slope, suggesting leakage to other nearby levels.

Figure 3.4(c) (Fig. 3.4(d)) shows for completeness the energy dispersions for the two excited states with fixed tunnel couplings and E_{R1} (E_{R2}), changing only the other energy splitting. As expected, Fig. 3.4(c) demonstrates that changes in E_{R2} only affect the second excited state dispersion. It is worth noting for the lowest plotted value, $E_{R2} = 9$ GHz, the tunnel couplings $2\Delta_{1-3} = 4$GHz are high enough such that there is no dispersion minima near $\varepsilon = 0$, and instead the dispersion has a negative slope until it's asymptote to E_{R2}. This behavior occurs for a traditional QDHQ dispersion when $2\Delta_{1,2}$ are larger than the singlet-triplet splitting, highlighting again the strong influence the presence of nearby levels can have on a qubit dispersion even if the relevant tunnel couplings are quite small. Conversely, Fig. 3.4(d) shows that changes in E_{R1} do impact the excited state dispersion, with larger E_{R1} pushing the excited state dispersion minimum up higher, thereby creating a flatter dispersion near $\varepsilon = 0$.

Chapter 4

Impact of electron-electron interactions on the two-electron energy spectrum

Section 4.1 is reprinted with permission from *Physical Review Letters*, Ref. [93]

4.1 Coherent Control and Spectroscopy of a Semiconductor Quantum Dot Wigner Molecule

Multielectron semiconductor quantum dots have extremely desirable properties for constructing and operating qubits. For single spin qubits, manipulating electrons above closed shells makes electric field driving more effective [102, 103], and certain qubits like quantum dot hybrid qubits [33] rely on multiple electrons to define the qubit states. Two-electron eigenstate energies are particularly important, since singlet-triplet splittings allow for Pauli spin-blockade readout [104] used in singlet-triplet qubits [34, 105, 106], exchange based qubits [28, 31], quantum dot hybrid qubits [33, 63], and single spin qubits [107], especially for high temperature operation [102, 108, 109].

When the characteristic interaction energy between electrons becomes larger than the orbital confinement energy, electronic states develop correlations and localize, forming Wigner molecules [110–119]. Imaging of such localization has been achieved using scanning electronic [120] and near-field optical [121] methods. The lowest-lying excited states in Wigner molecules have been studied using both optical [122, 123] and transport spectroscopy [124, 125], and the latter method has been used to observe a reduction in symmetric-antisymmetric orbital splittings [126]. While Wigner-type localization is known to reduce the gap between the ground and first orbital excited state, the impact on higher lying states and quantum control of such states has not been observed in experiments.

This Letter reports pulsed microwave coherent control and spectroscopy of an electrostatically confined semiconductor double quantum dot in the Wigner-molecule regime. We report coherent Rabi control of eight transitions ranging in frequency from 3.3 to 8.3 GHz, corresponding to energies far smaller than the single-particle confinement energy. With Ramsey spectroscopy, we map the energy as a function of double-dot detuning for 2 of these transitions. Using full configuration interaction (FCI) calculations, we argue that this dense manifold of states results from strong correlations and Wigner-molecule physics. Time-domain simulations of the Rabi experiments are used to explain the Rabi oscillations as a function of detuning energy. The full set of experimental spectroscopy results can be fit by a simple model consisting of two-electron states in the right quantum dot tunnel coupled to the lowest-lying state in the left dot.

Figure 4.1(a) describes the quantum dots, which are formed in an undoped Si-SiGe heterostructure with three layers of overlapping gates [44]. Fabrication details can be found in Ref. [83]. While the device can form three dots, we form two dots under gates $P1$ and $P2$, accumulating the rightmost dot as part of the right electron reservoir. We operate the double quantum dot (DQD) with five electrons near the (4,1)-(3,2) anticrossing, as shown schematically in Figs. 1(b)-(d). Tunnel rates between the two dots and to the reservoirs are set by gates $B1$, $B2$, and $B3$. Charge sensing is performed with dot CS, and its current is

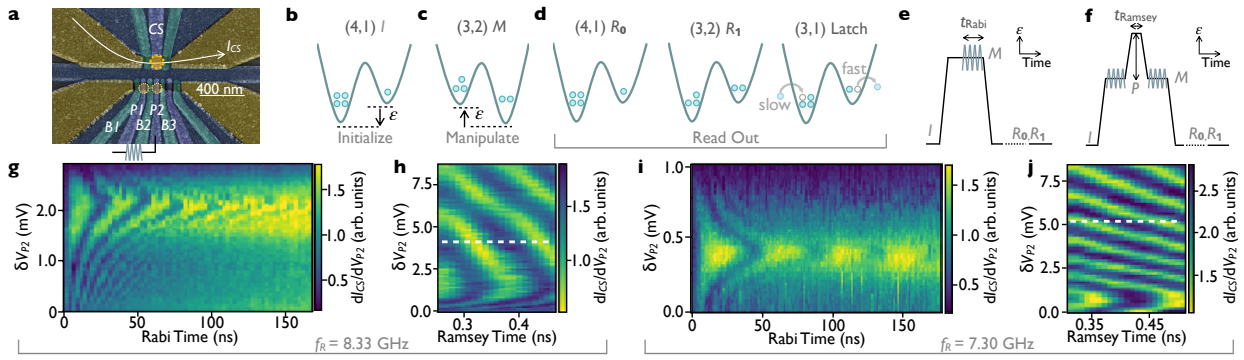

Figure 4.1: (a) False-color micrograph of a device lithographically identical to that measured here. Quantum dots are formed under $P1$ and $P2$. A current I_{CS} flows through the dot controlled by gate CS and is used to detect the electron occupation of the $P1$ and $P2$ dots. (b) The ground state for the five-electron system at negative ε is the charge configuration (4,1), used for initialization (I). (c) The ground state at positive ε is (3,2), used for manipulation (M). (d) Readout of the ground state, R_0, maps onto (4,1), while the excited states, R_1, maintain the (3,2) configuration. The tunnel rates to both reservoirs are tuned for a long decay time from (3,1), enabling latched readout. (e) Rabi pulse sequence used in this work. (f) Ramsey pulse sequence used in this work, composed of two $\pi/2$ pulses and a detuning pulse with amplitude P. (g)-(j) Rabi and detuned-Ramsey measurements of two coexisting states. For (g),(i), δV_{P2} corresponds to a relative shift of the entire pulse sequence; for (h),(j) δV_{P2} corresponds to relative changes in P. Dashed lines in (h,j) denote the value of δV_{P2} for which $P = 0$. (g),(h) Rabi and Ramsey oscillations using $f_R = 8.33$ GHz. (i),(j) Rabi and Ramsey oscillations using $f_R = 7.30$ GHz, taken at the same device tuning but different ε from (g),(h).

---

measured using a two-stage cryogenic high-electron-mobility transistor amplifier [127] mounted on a separate printed circuit board (PCB) connected to the sample PCB by stainless steel coax.

We initialize at setting I, shown in Fig. 4.1(b), in the (4,1) ground state, which has a large splitting between the ground and first excited states. We ramp the DQD detuning ε across the interdot transition line to a manipulation point (M) at positive ε, as shown in Fig. 4.1(c), where we apply microwave pulse sequences. Rabi and detuned-Ramsey pulses at Mdrive coherent rotations between two-particle states in the right quantum dot while maintaining the (3,2) configuration. To perform readout, we adiabatically ramp across the interdot transition line: the (3,2) ground state then maps onto the (4,1) ground state (R_0), while the excited states (R_1) maintain their (3,2) configuration, as indicated in Fig. 4.1(d).

Latched measurement [89] is used to enhance readout fidelity: for the excited states (R_1), an electron rapidly tunnels into the right reservoir to form a metastable (3,1) charge state, which slowly returns to the (4,1) ground state. The latch duration is determined by the left barrier, which is tuned to have a long tunnel time.

Figures 4.1(e)-(j) demonstrate coherent control of two different DQD transitions performed by applying pulse sequences to gate $P2$ at 8.33 and 7.30 GHz. Fig. 4.1(e) shows the Rabi sequence, a continuous drive of frequency f_R, and Fig. 4.1(f) shows the Ramsey sequence, two $\pi/2$ microwave pulses of frequency f_R surrounding a detuning ramp. This Ramsey sequence enables the efficient measurement of energy splittings as a function of ε, and can be performed at any known Rabi resonance location [78]. The resulting Rabi and Ramsey oscillations are shown in Fig. 4.1(g)-(j). The vertical axis δV_{P2} determines ε, and the centers of the Rabi chevrons in Figs. 4.1(g) and 4.1(i) occur at the ε values where f_R is resonant with the transition energy. The dependence of the Rabi oscillations on ε directly reflects changes in the corresponding energy levels, providing a characteristic fingerprint for

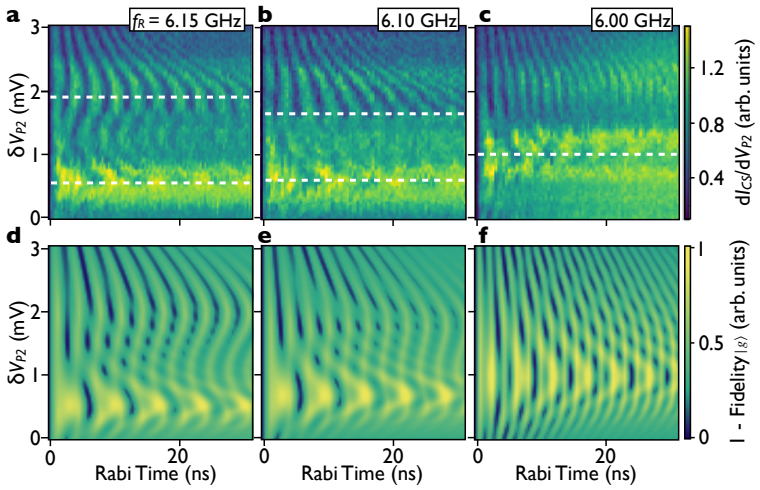

Figure 4.2: (a) Rabi oscillations with $f_R = 6.15$ GHz, with the centers of two on-resonance oscillations marked by dashed lines. (b) Rabi oscillations with $f_R = 6.10$ GHz, where the two resonances move closer together in ε as compared with (a). (c) Rabi oscillations with $f_R = 6.00$ GHz, where the on-resonance locations have completely merged. (d)-(f) Simulated Rabi oscillations corresponding to (a)-(c) using a simplified, four-level model

each transition.

Figure 4.2 shows Rabi oscillations with two distinct resonances visible in the same plot as indicated by dashed lines at the on-resonant locations. As the driving frequency is reduced from $f_R = 6.15$ to 6.00GHz, the centers of the oscillations overlap at $\delta V_{P2} = 1$mV. Numerical simulations of these oscillations are shown in Fig. 4.2(d)-4.2(f), using a four-level model, where two closely spaced states make transitions to two higher states. A key feature of these two oscillations is the difference in width as a function of δV_{P2}; this behavior is reproduced in the theoretical model by different slopes for the respective energy dispersions, where a flatter slope corresponds to longer-lived oscillations [78]. The unusual merging of the resonances is reproduced in the model with a level crossing.

Figures 4.1 and 4.2 report four transitions as a function of the gate voltages defining the quantum dot. Additional Rabi oscillations were measured with microwave frequencies ranging from 3.25 to 7.6 GHz (S4 in Sec. 4.2). These data demonstrate Rabi driving of eight distinct transitions below 10 GHz, an unusual density of transitions that cannot be described by noninteracting two-electron physics. We must therefore consider how electron-electron interactions influence the excited energy level spectrum [113, 128, 129].

A dimensionless measure of the interaction strength is $R_W = E_{\mathrm{ee}}/E_{\mathrm{orb}}$ [111], the ratio of the electron-electron interaction energy E_{ee} and the lowest quantum dot orbital excitation energy E_{orb}. To estimate E_{orb} we use FCI methods to diagonalize the Hamiltonian of a parabolically confined two-electron quantum dot, including the effects of valley splitting, valley-orbit coupling, and electron-electron interactions, obtaining the energy eigenvalues and eigenstates [117, 130–133]. Good correspondence between theory and experiment is found with a valley splitting of 3.81 GHz and an orbital confinement energy $E_{\mathrm{orb}}/h = 59.2$ GHz. Approximating E_{ee} as the Coulomb energy of two point charges separated by the characteristic length scale of the quantum dot, $E_{\mathrm{ee}} = \frac{e^2}{4\pi\epsilon}\sqrt{\frac{m_t\omega_x}{\hbar}}$, yields $R_W = 12.7$ for a dot radius of 40 nm. This estimate is consistent with a quantum dot situated in a 90 nm wide channel below a 70 nm wide gate. Although this R_W is greater than that observed in carbon

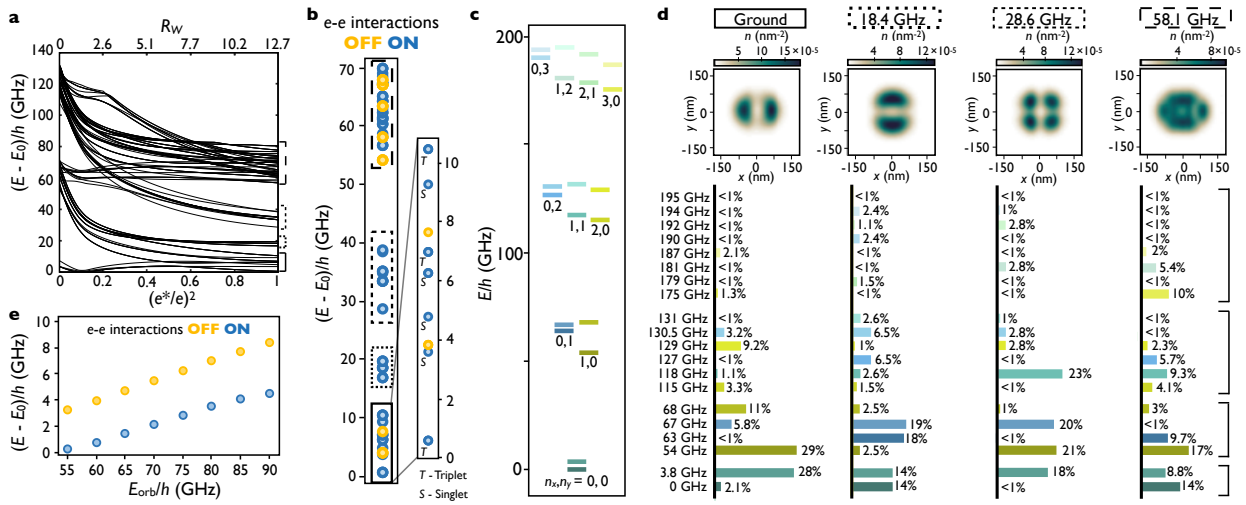

Figure 4.3: FCI calculations performed using parabolic confinement potentials with $E_{\text{orb}}/h = \omega_x/2\pi = 59.2$ GHz and $\omega_y = 1.07\omega_x$. (a) Two-electron excited state energies ($E_1 - E_0$) plotted as a function of the relative interaction strength $(e^*/e)^2$ (bottom) and the Wigner parameter R_W (top). (b) Excited state energies with ($e^* = e$, blue) and without ($e^* = 0$, yellow) interactions. The spectrum is grouped into manifolds, indicated by boxes, with the lowest manifold in the inset. (c) The single-electron energy levels used to construct the interacting two-electron wave functions in (b), with the orbitals labeled as n_x, n_y. Each grouping of orbital excitations forms a valley-split doublet. (d) Electron density distributions of the lowest-energy singlet wave functions in each of the four manifolds in (b), identified by the corresponding border style. The bar plots below indicate the contributions from each of the single-electron wave functions in (c). (e) Two-electron singlet-triplet splitting with (blue) and without (yellow) electron-electron interactions as a function of orbital confinement, demonstrating large variation as a function of E_{orb} when interactions are strong.

---

nanotubes ($R_W = 1.64$ [126]) and Ga[Al]As quantum dots ($R_W = 1.55$ [124]), recent Si-SiGe quantum dot experiments report values of $R_W \approx 3.6$ ($E_{\text{orb}}/h = 725$ GHz [74]) and $R_W \approx 5.2$ ($E_{\text{orb}}/h = 362$ GHz [69,134]), suggesting that interactions may play an important role in many quantum dot and spin qubit experiments. Confinement energies are also suppressed in multielectron dots, which are frequently employed as qubits [103]; in such cases, we expect to observe large R_W values deep in the Wigner-molecule regime.

To understand the impact of electron-electron interactions on the two-electron energy spectrum, it is instructive to tune the Coulomb interactions in the FCI simulations by artificially introducing an effective charge e^* with $e^*/e \leq 1$, so that $R_W = \frac{e^{*2}}{4\pi\epsilon}\sqrt{\frac{m_t}{\hbar^3\omega_x}}$. Fig-

ure 4.3(a) shows the two-electron energy splittings from the ground state as e^* is changed. With increasing interaction strength, we observe that the energy eigenstates are composed of a growing number of valley and orbital basis states, and the electron positions become increasingly anticorrelated. Importantly, this hybridization results in a densely packed array of energy levels in the strong interaction regime, $e^*/e = 1$.

Figure 4.3(b) shows the noninteracting spectrum at $e^* = 0$ (yellow) and the fully interacting spectrum at $e^* = e$ (blue), revealing for the interacting case a manifold structure highlighted with solid and dashed boxes. Each of these manifolds contains both singlet and triplet states, all of which have similar electron densities. This similarity in energy and spatial density within a manifold can be understood by looking at the corresponding combinations of single-particle basis states. These single-particle states up to 195 GHz are shown in Fig. 4.3(c) and consist of x and y orbital excitations (n_x,n_y) and valley state excitations. Figure 4.3(d) reports the in-plane electron density and the fractional contribution of the single-particle states for the first singlet level within each manifold shown in Fig. 4.3(b). The transitions between manifolds in Fig. 4.3(b) correspond to quantitative changes in the contributions of single-particle states. For example, Fig. 4.3(d) reveals the largest contributions to the ground state singlet are from two states: the (n_x,n_y)=(0,0) high energy valley eigenstate and the (n_x,n_y)=(1,0) low energy valley eigenstate. In the next manifold, there are roughly equal contributions from each valley eigenstate for a given single-particle state and a switch from (1,0) to (0,1). The evolution in the contributions from the single-particle orbital modes is revealed both in the bar graphs and the electron density plots.

An important characteristic of the large R_{W} regime is that relatively small changes in E_{orb} lead to rapid changes in the lowest-energy gap in the system (the singlet-triplet splitting). Figure 4.3(e) plots these theoretically calculated energy splittings with (blue) and without (yellow) electron interactions as a function of lateral confinement strength. Changing the confinement from 55 to 90 GHz (less than a factor of 2 change) in the presence of interactions results in variation of the singlet-triplet splitting by more than a factor of 20.

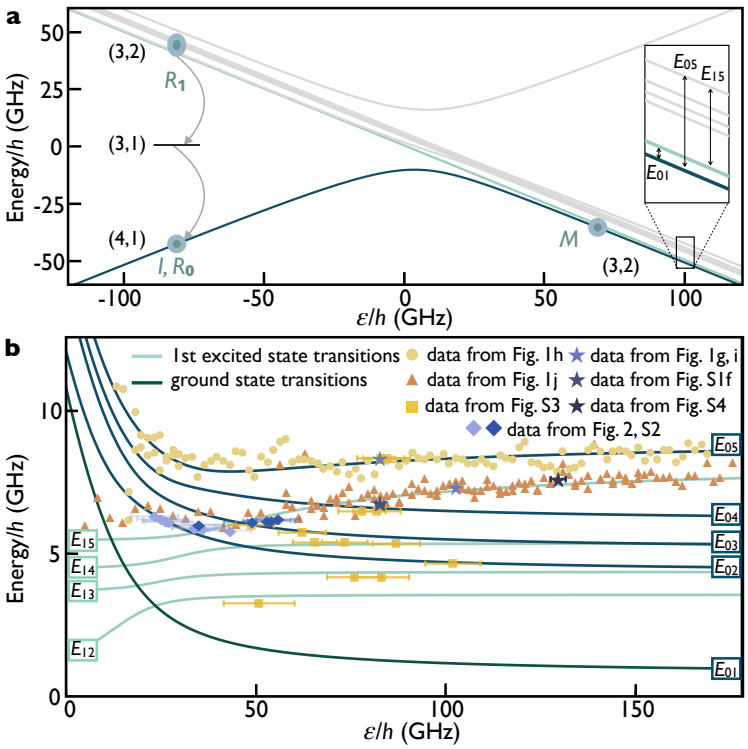

Figure 4.4: (a) Energy eigenvalues versus ε of a Hamiltonian motivated by the electron interaction effects reported here. Measurement locations from Fig. 1 are indicated. Inset: excited state spectrum with example transitions shown. (b) Frequencies versus ε of the eight transitions reported here, $E_{02}-E_{05}$, and $E_{12}-E_{15}$, and E_{01} which is inferred but not directly observed. The dark teal lines are the energy differences between the ground state and energy level n, defined in (a); the light teal lines are differences between the first excited level and the same energy levels in (a). Symbols plotted correspond to frequencies extracted from the experiment, as described in the legend.

Figure 4.4 summarizes the experimental results on DQD detuning plots. Figure 4.4(a) shows the eigenvalues of a Hamiltonian with five uncoupled excited states in the right quantum dot, each coupled to the left quantum dot's ground state, used to fit the Rabi and Ramsey data reported in this Letter. We anticipate that both singlet and triplet spin configurations are present among these two-electron excited states based on the FCI calculations in Fig. 4.3. Transitions between such spin states are mediated by virtual tunneling events similar to the quantum dot hybrid qubit (QDHQ), as described in Ref. [63].

The excited state energies in the infinite-detuning limit E_1-E_5 are motivated by the

energy levels reported in Fig. 4.3. Figure 4.4(b) plots in dark teal the difference in energy between the ground and excited states E_{01}-E_{05}, which depend on ε. It plots in light teal the difference between the higher excited states and the first excited state energy E_{12}-E_{15} ($E_1/h = 0.75\,\mathrm{GHz}$). Though the energy splitting E_{01} is not directly observed, its presence is motivated by the FCI calculations described above, and we infer its existence and energy from the data plotted in Fig. 4.4(b). We believe this state has nonzero initialization occupation because of both nonadiabaticity of the pulse sequence and thermal excitation caused by electron temperatures of about 100 mK ($k_BT = 2.1\,\mathrm{GHz}$).

The data shown in Fig. 4.4(b) correspond to all the Rabi and Ramsey spectra reported in this Letter, as described in the legend. We plot the spectra from Figs. 4.1(h) and 4.1(j) as light yellow circles and orange triangles, and fit to them the transitions E_{05} and E_{15}, corresponding to the differences between the ground and first excited states to the fifth excited state. The resonant frequencies from Figs. 4.2(a)-4.2(c) that move up (down) between Figs. 4.2(a) and 4.2(c) are shown as light (navy) blue diamonds.

The merging of these points with decreasing f_R provides additional evidence that these Rabi oscillations are driven from the ground and first excited state; if these two resonances belonged to the same dispersion, they would merge into a single chevron at the dispersion minimum instead of overlapping. If both transitions occurred as excitations from the ground state, a level crossing would only occur if one of the tunnel couplings was anomalously low (≤ 0.1 GHz) which is not supported by the shape of the Ramsey spectra. Finally, the yellow squares in Fig. 4.4(b) show energies corresponding to Rabi oscillations with a 4.4 GHz range of microwave frequencies. The density of transitions in frequency space as compared with the FCI calculations supports the necessity to consider both E_0 and E_1 transitions. In total, Fig. 4.4 summarizes the coherent control of eight transitions in this Wigner molecule, E_{02}-E_{05}, and E_{12}-E_{15}, and highlights how these transitions depend on ε.

As shown in Fig. 4.3(e), for large R_W, the singlet-triplet splitting becomes highly tunable, offering opportunities and pitfalls for applications in quantum dot qubits. For qubits like the

QDHQ, where it is useful to tune the singlet-triplet splitting to a desired value, interactions can amplify small changes in confinement-defining gate voltages into large and useful changes in singlet-triplet splittings. However, for other qubits such as Loss-DiVincenzo, singlet-triplet, and exchange-only qubits, unexpectedly large shifts in the singlet-triplet splitting could weaken or prevent read-out mechanisms like the Pauli spin blockade. Furthermore, as seen in this Letter, a suppressed singlet-triplet splitting may be accompanied by additional low-lying energy levels, which can interfere with the two-level system required for a qubit.

In conclusion, we have studied a quantum dot in the limit of large R_W, where the electron-electron interaction energy scale surpasses the orbital energy splitting. In this regime, we identify and coherently control eight separate resonances. Based on theoretical calculations we have argued that these states arise from strong interactions and Wigner-molecule physics. We use a six-level model, motivated by both experiment and FCI calculations, to explain how the dense set of energy levels in a single dot affects the DQD spectrum as a function of ε. The observation of Wigner molecules in silicon quantum dots suggests that small changes in confinement can have a strong effect on the qubit energy splitting in this system. This could be harnessed as a tool for controlling qubit energy splittings, but if unanticipated, this phenomenon could also lead to qubit interference from low-lying levels or the suppression of level-dependent qubit readout.

The Supplemental Material below provides additional raw data and technical details on the models used in Fig. 4.2 and Fig. 4.4, the FCI calculations, the estimations of state populations, the experimental setup, and includes Ref. [135–137].

This research was sponsored in part by the Army Research Office (ARO), through Grant No. W911NF-17-1-0274, and by the Vannevar Bush Faculty Fellowship program under ONR Grant No. N00014-15-1-0029. J.C. acknowledges support from the National Science Foundation Graduate Research Fellowship Program under Grant No. DGE-1747503 and the Graduate School and the Office of the Vice Chancellor for Research and Graduate Education at the University of Wisconsin-Madison with funding from the Wisconsin Alumni Research

Foundation. We acknowledge the use of facilities supported by the NSF through the UW-Madison MRSEC (DMR-1720415) and by the NSF MRI program (DMR-1625348). The views and conclusions contained in this Letter are those of the authors and should not be interpreted as representing the official policies, either expressed or implied, of the ARO, NSF, or the U.S. Government. The U.S. Government is authorized to reproduce and distribute reprints for government purposes notwithstanding any copyright notation herein.

4.2 Supplementary material for 'Coherent control and spectroscopy of a semiconductor quantum dot Wigner molecule'

These supplemental materials provide additional data, details of the theoretical simulations, and explanations of the measurement and analysis procedures.

4.2.1 S1: Additional information for Figure 1

The data in Fig. 4.1 presents two distinct dispersions that are individually addressable. The light yellow circles in Fig. 4.4(b) are produced by fitting the resulting data from Fig. 4.5(a,b) for the frequency of oscillation. The orange triangles in Fig. 4.4(b) are produced by fitting the results from Fig. 4.5(c,d).

In order to map the dispersions from Fig. 4.1(h,j) relative to each other, Fig. 4.1(g,i) are repeated at the same detuning, achieved using the microwave drives of $f_R = 8.33\,\mathrm{GHz}$ and $f_R = 6.75\,\mathrm{GHz}$, as shown in Fig. 4.5(e,f). Rabi frequencies extracted from Fig. 4.5(e,f) are represented in Fig. 4.4(b) by including the $f_R = 6.75\,\mathrm{GHz}$ purple star at the same detuning as the $f_R = 8.33\,\mathrm{GHz}$ light purple star. Though we do not observe off resonant oscillations from one spectrum in measurements of the other, it does appear that the region of suppressed coherence in Fig. 4.5(e) is the region of enhanced coherence in Fig. 4.5(f) and visa versa.

The resonance in Fig. 4.5(f) belongs to the same energy level as that in Fig. 4.1(i), as can be seen by comparing Ramsey spectroscopy taken at the two f_R locations, as shown in Fig. 4.5(g,h). The general shape of the data in Fig. 4.5(g,h) is consistent, and the only difference is a relative shift in δV_{P2} by 0.96 mV. To produce the points in Fig. 4.4(b), we shifted the data in Fig. 4.5(d,h) by $\delta V_{P2} = 0.96\text{mV}$, using the dispersion minima as reference, so that they match the detuning in Fig. 4.5(g). The data in Fig. 4.4(b) is converted from gate voltage to detuning with a detuning alpha of $\alpha_{\varepsilon,P2} = 0.085 \pm 0.009\,\text{meV/mV}$.

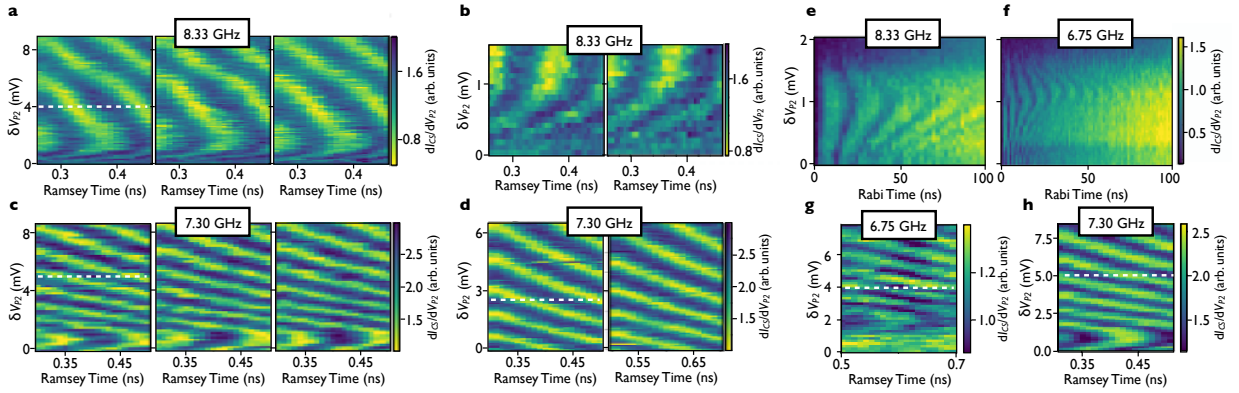

Figure 4.5: Ramsey oscillation averaging and alignment. (a) Ramsey oscillations with $f_R = 8.33$ GHz taken consecutively. These data are averaged together to produce Fig. 4.1(h). (b) Ramsey oscillations with $f_R = 8.33$ GHz taken consecutively. These data are averaged together, and the oscillations, in addition to those from (a), are fit to produce the light yellow circles in Fig. 4.4(b). (c) Ramsey oscillations with $f_R = 7.30\,\text{GHz}$ taken consecutively. These data are averaged together to produce Fig. 4.1(j). (d) Ramsey oscillations with $f_R = 7.30$ GHz taken consecutively. The oscillations in these data are fit and the corresponding fits are averaged together. These points and the points resulting from (c) produce the orange triangles in Fig. 4.4(b). (e) Rabi oscillations for the same resonance as Fig. 4.1(g), with $f_R = 8.33$ GHz. (f) Rabi oscillations for the same energy level as Fig. 4.1(i) but a different detuning, now with $f_R = 6.75$ GHz. This data set is taken directly after (e), with the only change being the microwave drive. The centers of the two chevrons correspond to $\delta V_{P2} = 1.1$ mV. (g) Ramsey fringes corresponding to the resonance in (f) taken at $f_R = 6.75$ GHz. (h) Ramsey fringes, taken at a different detuning from (g) , with the same $f_R = 7.3$ GHz as Fig. 4.1(j). The dashed lines in (a,c,d,g,h) denote the value of δV_{P2} for which the Ramsey detuning is zero.

Table 4.1: Sets of on-resonance oscillations discussed in Fig. 4.2 and Fig. 4.6.

Set1		Set2	
f_R (GHz)	Figure	f_R (GHz)	Figure
6.30	Fig.4.6(a)	6.15	Fig.4.2(a)
6.15	Fig.4.6(c)	6.10	Fig.4.2(b)
6.00	Fig.4.6(d)	6.00	Fig.4.2(c)
5.90	Fig.4.6(e)	5.90	Fig.4.6(f)

Set3		Set4	
f_R (GHz)	Figure	f_R (GHz)	Figure
5.85	Fig.4.6(g)	6.20	Fig.4.6(b)
5.80	Fig.4.6(h)	-	

4.2.2 S2: Additional Rabi data and four-level simulation details

For the interested reader, Fig. 4.6 contains additional oscillations used as diamonds in Fig. 4.4(b), where each diamond represents the center of a Rabi oscillation for a given drive frequency. As seen in Fig. 4.2, 4.6, many of the data sets have two clear on-resonance oscillations. In these cases, both centers are plotted with the same frequency and a different value of δV_{P2}. All of the extracted data from these two figures can be seen in Fig. 4.6(i), where the different markers correspond to different sets of data taken consecutively (before the device shifted). These sets are enumerated in Table 4.1. The uncertainty in Fig. 4.6(i) is the uncertainty in the center of the oscillation, while the uncertainty in these points in Fig. 4.4(b) includes uncertainty in their location relative to zero double-dot detuning.

The Rabi measurements shown in Fig. 4.2 indicate multi-level structure. We find that the best model that reproduces the main features of the experimental measurements in a simple way consists of four relevant states: two partially populated lower levels, separated by a small energy E_{01}, that make transitions to two excited states under detuning driving

fields. The effective Hamiltonian of this four-level system is

$$H_0^{\text{toy}} = \begin{pmatrix} 0 & 0 & 0 & 0 \\ 0 & E_{01} & 0 & 0 \\ 0 & 0 & f(\varepsilon) & 0 \\ 0 & 0 & 0 & g(\varepsilon) + E_{01} \end{pmatrix}, \tag{4.1}$$

where $f(\varepsilon)$ and $g(\varepsilon)$ are interpolation functions based on the energy measurements, shown as blue and orange lines in Fig. 4.6(i). We set $E_{01}/h = 3$ GHz, which is compatible with the small energy gap between the lowest two states observed in the experiment and large enough to avoid undesired interactions. The driving field is characterized by

$$H_1^{\text{toy}} = \delta\varepsilon \cos(\omega t) \begin{pmatrix} 0 & 0 & R_{02} & 0 \\ 0 & 0 & 0 & R_{13} \\ R_{02} & 0 & 0 & 0 \\ 0 & R_{13} & 0 & 0 \end{pmatrix} \tag{4.2}$$

where R_{02} and R_{13} are fitting parameters. The only other fitting parameter is the ground state population ρ_{00}, assuming $\rho_{11} = 1 - \rho_{00}$. The fitting parameters used for each case are shown in Table 4.2. We find that an even simpler model, such as a three-level system with a singly-populated ground state and two interacting excited states, might also be an explanation. However, the simulations with this simpler model added more unobserved interference phenomena. We note that the simple four-level model is rather limited since the values of the Rabi parameters R_{02} and R_{13} should depend on detuning. Moreover, the energy level landscape is more complicated than a four-level system. Nevertheless, this simple model captures the main features in the measurements.

Finally, to simulate the presence of noise in Fig. 3, we perform a Gaussian convolution with $\sigma_\varepsilon = 7.1\mu$eV. This number is extracted by averaging the $\sigma_\varepsilon = \frac{\sqrt{2}\hbar}{|\frac{dE}{d\varepsilon}|T_2^*}$ computed with T_2^* and $\frac{dE}{d\varepsilon}$ from the 7.30 GHz and 8.33 GHz resonances shown in Fig. 4.2.

Table 4.2: Parameters R_{02} and R_{13} from Eq. 4.2, in addition to the drive frequency f_R and ground state population ρ_{00}, which are all used for the simulations in Fig. 4.2(d-f).

	Fig.4.2(d)	Fig.4.2(e)	Fig.4.2(f)
f_R (GHz)	6.15	6.1	6.0
$R_{02} \times 10^3$	0.443	0.463	0.616
$R_{13} \times 10^3$	0.925	0.984	1.626
ρ_{00}	0.7	0.7	0.65

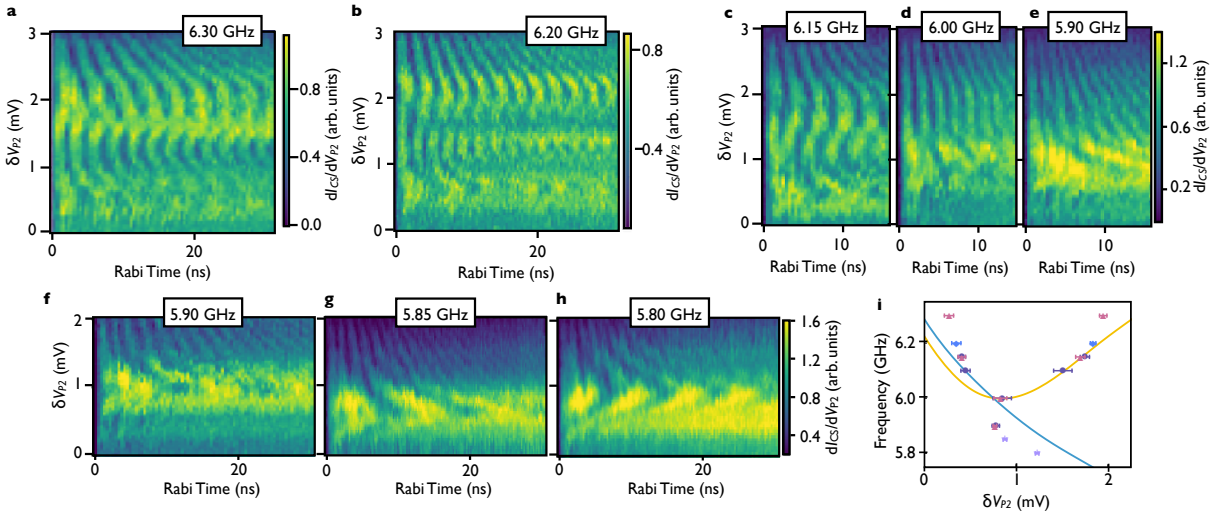

Figure 4.6: Additional level crossing data corresponding to the diamonds in Fig 4.4(b). (a,b) Rabi oscillations at $f_R = 6.30\,\text{GHz}$ and $f_R = 6.20\,\text{GHz}$. (c,d) Additional Rabi oscillations at $f_R = 6.15\,\text{GHz}$ and $f_R = 6.00\,\text{GHz}$ used to combine multiple sets of data with different V_{P2} offsets. (e,f) Rabi oscillations with $f_R = 5.90\,\text{GHz}$, again used for combining multiple data sets. (g) Rabi oscillations with $f_R = 5.85\,\text{GHz}$. (h) Rabi oscillations with $f_R = 5.80\,\text{GHz}$. (i) All of the data from the navy blue and light blue diamonds in Fig 4.4(b). Blue and orange lines correspond to the interpolation functions $f(\varepsilon)$ and $g(\varepsilon)$, respectively, which are described in section S2.

4.2.3 S3: Additional data for Figure 4

Figure 4.7, 4.8 contains the measured Rabi oscillations corresponding to the plots in Fig 4.4(b). The data in Fig. 4.7 is grouped in four sets, (a-e), (f-i), (j,k), and (l), as shown in (m). Each set represents a portion of data that is taken without any drift of the DQD device, and without changing any pulse-shape parameters besides microwave frequency. Each extracted

point is obtained by looking at line-cuts in time through the data and estimating the center point of the oscillation in gate voltage. Note that all the data in these figures span 3 mV on the gate which dictates the quantum dot detuning, P_2. The drastic changes in size, shape, and frequency of these oscillations in the same relative window of detuning supports the interpretation that these oscillations correspond to different energy level transitions. The location of (e,l) relative to the polarization line, which should be at the zero detuning point for the DQD, is approximated using their resonant locations within the latched readout region, stability diagrams and the pulse height.

The data in Fig. 4.8 appears as a dark purple star in Fig. 4(b).

As shown in Fig. 4.9, time-domain measurements searching for Rabi were performed at four other microwave frequencies: $f_R = 6.93\,\text{GHz}$, $7.88\,\text{GHz}$, $8.9\,\text{GHz}$, and $9.8\,\text{GHz}$. Included in Fig. 4.9(a,c) are two measurements taken at the same device tuning and with the same microwave amplitude as (b) and (d-f), respectively, in order to compare the shape, signal strength, and oscillation frequencies. Comparing Fig. 4.9(b) with Fig. 4.9(a), one sees that in Fig. 4.9(b) there is no clear peak in the oscillations as a function of detuning, whereas in

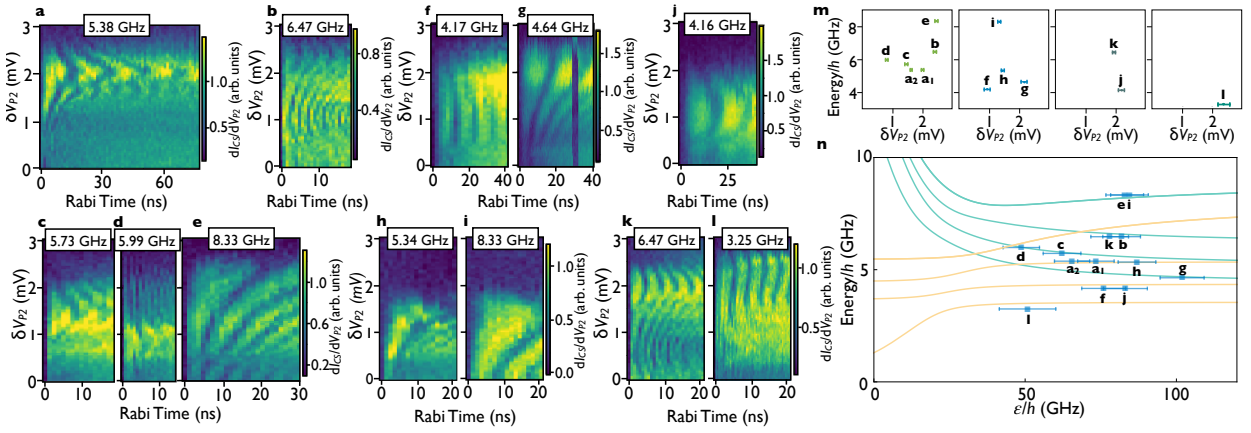

Figure 4.7: Rabi oscillations associated with the yellow squares in Fig 4.4(b), with frequencies (a) $f_R = 5.38\,\text{GHz}$, (b) $f_R = 6.47\,\text{GHz}$, (c) $f_R = 5.73\,\text{GHz}$, (d) $f_R = 5.99\,\text{GHz}$, (e) $f_R = 8.33\,\text{GHz}$, (f) $f_R = 4.17\,\text{GHz}$, (g) $f_R = 4.64\,\text{GHz}$, (h) $f_R = 5.34\,\text{GHz}$, (i) $f_R = 8.33\,\text{GHz}$, (j) $f_R = 4.16\,\text{GHz}$, (k) $f_R = 6.47\,\text{GHz}$, (l) δV_{P2}= 3.25 GHz. The points in (m) represent the location in relative P_2 of the center of the Rabi oscillation for a given driving frequency. (n) These four sets are then placed onto the model by simultaneously matching (e,i), and (b,k), as well as looking at the distance of (e,l) from the approximate polarization line.

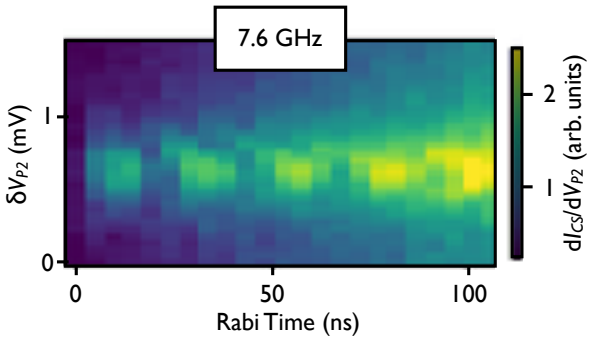

Figure 4.8: Rabi oscillations associated $f_R = 7.60$ GHz, shown as a dark purple star in Fig. 4.4(b).

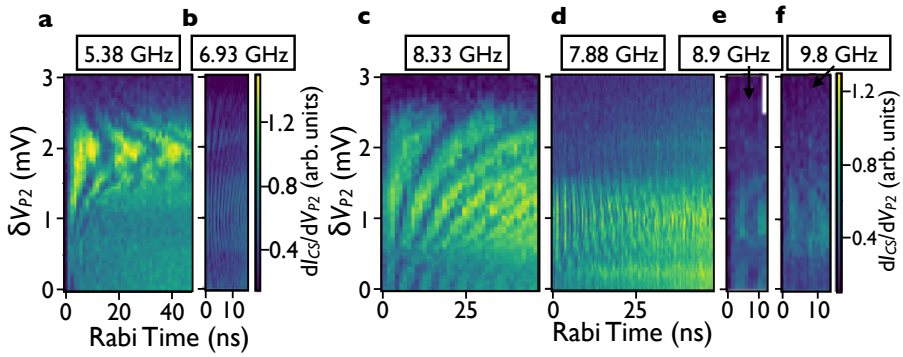

Figure 4.9: Comparison of Rabi data for different driving frequencies, including those not included in the model. All panels were taken at the same device tuning. (a) $f_R = 5.38$ GHz oscillations shown in Fig. 4.7, which display a chevron pattern typical of Rabi oscillations. (b) Off-resonant oscillations observed at the applied microwave frequency $f_R = 6.93$ GHz. The applied amplitude (100mV_{pp}) is the same as in (a). (c) The same $f_R = 8.33$GHz oscillations as shown in Fig. 4.7, which display relatively slow detuning-dependent oscillations characteristic of Rabi oscillations. (d-f) Off-resonant oscillations at the applied microwave frequencies f_R = 7.88 GHz, 8.9 GHz, and 9.8 GHz, displaying fast oscillations, but not the characteristic detuning dependence typical of Rabi oscillations. The applied amplitude ($190\,\text{mV}_{\text{pp}}$) is the same as in (c).

Fig. 4.9(a) there are actually two clear peaks around 2 mV and 1.6 mV. Additionally, the oscillations in Fig. 4.9(b) have much lower signal strength and are much faster, all indications of off-resonant oscillations. These same parameters can be used to compare Fig. 4.9(d-f) with Fig. 4.9(c). Fig. 4.9(d) has comparable signal strength to Fig. 4.9(c) but no oscillation peaks and the oscillations are much faster. Fig. 4.9(e,f) have much lower signal strength with

no clear oscillation peak. Alhough these frequencies produced oscillations, there was not strong enough evidence to claim they correspond to their own resonance; thus they were not included in Fig. 4(b).

4.2.4 S4: Simulation details for Figure 3

The simulation results shown in Fig. 4.3 are performed by combining a full configuration interaction (FCI) approach with the empirical tight-binding (TB) theory of Boykin et al. [135, 136], as described in detail in Ref. [133]. In the TB model, the nearest-neighbor and the next nearest neighbor hopping parameters $t_1 = 0.6829$ eV and $t_2 = 0.6119$ eV are chosen such that the location of the resulting band minima coincide with the location of bulk silicon's conduction band minima, and the effective mass, determined by the curvature of the conduction band at its minima, is equal to the lateral effective mass of bulk silicon. With an additional hopping parameter t_3 = - 0.026 eV, chosen such that the transverse effective mass of bulk Si is obtained, the model becomes two-dimensional in the x-z plane. We are thus able to study the effects of different interface profiles by simply assigning on-site terms E_{Si} and E_{SiGe} to grid points in different patterns. Resulting wave functions have fast oscillations in z that are responsible for the breaking of valley degeneracy, and disorder at the interface causes valley and orbital degrees of freedom to couple. In the calculations, we treat the third dimension y analytically with the assumption that the confinement potential is parabolic.

While TB provides an accurate description of single electron wave functions by capturing the valley physics of silicon and allowing modeling of the quantum well interface disorder, FCI allows us to calculate two electron energies by including the effects of electron-electron interactions. After adding the spin degree of freedom, we generate all possible two-electron Slater determinants based on the 45 lowest energy TB eigenstates, which constitute the basis for the FCI calculation. We calculate the full Hamiltonian, including the electron-electron interaction term (with dielectric constant 11.4 [137]), in this basis and diagonalize it to obtain

the two-electron energy eigenvalues and eigenstates. For the simulation in Fig. 4.3, we used a tilted quantum well interface with a tilting angle of $\sim 0.2°$, quantum well width of 9.1 nm and an electric field of 0.6 MV/m perpendicular to the interface. The atomic step height is a/4 where a = 0.543 nm is the Si lattice constant, the distance between steps is 33.8 nm, and the distance from the dot center to the nearest step is 6.1 nm. With these parameters, valley splittings range from 2.4 to 4.8 GHz (10 to 20 μeV) in the considered $\hbar\omega_x$ domain, and in particular is 3.81 GHz (14 μeV) for the $\omega_x/2\pi = 59.2$ GHz used in Fig. 4.3(a). We pick the location of the center of the dot with respect to the uniform steps at the interface to obtain the best agreement with the experimental data.

4.2.5 S5: Choice of Hamiltonian Parameters for Figure 4

The lines in Fig. 4.4(a) are the eigenvalues of

$$H = \begin{pmatrix} \varepsilon/2 & \Delta_0 & \Delta_1 & \dots & \Delta_5 \\ \Delta_0 & -\varepsilon/2 & 0 & \dots & 0 \\ \Delta_1 & 0 & -\varepsilon/2 + E_1 & \dots & 0 \\ \Delta_2 & 0 & 0 & \ddots & 0 \\ \Delta_3 & 0 & 0 & \dots & 0 \\ \Delta_4 & 0 & 0 & \dots & 0 \\ \Delta_5 & 0 & 0 & \dots & -\varepsilon/2 + E_5 \end{pmatrix}, \tag{4.3}$$

which describes a system of five excited states in the right quantum dot coupled to the left quantum dot. The values for energies E_n and tunnel couplings Δ_n are listed in Table 4.3. Though we have a large quantity of data, including two detuned-Ramsey measurements of different levels (Fig. 4.1(h,j)), Rabi measurements of eight different levels(Fig. 4.1(g,i), Fig. 4.7), and Rabi measurements of two merging levels(Fig. 4.2(a-c), Fig. 4.6), the five-level model from Fig. 4.4(b) based on Eq. 4.3 is still under-constrained. It has 11 independent parameters: five energies, E_1-E_5, and six tunnel couplings, Δ_0-Δ_5.

The detuned Ramsey data from Fig. 4.1(h) (light yellow circles in Fig. 4.4(b)) provides an approximate value for E_5 and Δ_5, which respectively govern the high-detuning asymptote and low-detuning shape of E_{05}. Similarly, the set of detuned Ramsey data from Fig. 4.1(j) (orange triangles in Fig. 4.4(b)) places strong constraints on E_{15}. Since $E_{05} - E_{15} = E_{01}$, these two Ramsey sets of data together constrain the high-detuning asymptote and low-detuning shape of E_{01}, thereby dictating the values of E_1 and Δ_0. With this constraint on E_{01}, the relation $E_{0n} - E_{1n} = E_{01}$ narrows the values of the other energies E_2-E_4. Each energy E_n has at least two Rabi measurements (one for E_{0n} and one for E_{1n}) to define its value. Table 4.3 shows the percent change in each energy E_n which degrades the fit.

The individual tunnel couplings Δ_1-Δ_4 are not as firmly constrained as the energy values. However, as all the eigenvalues are interdependent, the individual tunnel couplings as well as the sum of the tunnel couplings are constrained to be within a certain range. For example, having any or all of Δ_n too large will push both E_{01} downward and E_{05} upward, both of which are well constrained, as discussed above. Table 4.3 shows the percent change in each tunnel coupling Δ_0 and Δ_5, as well as the percent change for all the tunnel couplings Δ_1-Δ_4 which are set equal, that degrades the fit.

Table 4.3: Parameters for Eq. 4.3 chosen to best fit the data and percent change in each parameter that degrades the fit.

Energy			Tunnel Coupling		
E_n	E/h (GHz)	δE (%)	Δ_n	Δ/h (GHz)	$\delta\Delta$ (%)
-	-	-	Δ_0	6	10
E_1	0.75	20	Δ_1	1.5	30
E_2	4.3	10	Δ_2	1.5	30
E_3	5.1	8	Δ_3	1.5	30
E_4	6.1	5	Δ_4	1.5	30
E_5	9	4	Δ_5	10.5	10

4.2.6 S6: Estimations of excited-state populations

In the experiment, the qubit is initialized at very negative detuning values. In this region, the ground state is well-separated from the first-excited state, ensuring proper initialization. To manipulate the qubit, the detuning is pulsed from this region to positive detuning. Due to the large number of low-lying excited states, some excited states may be populated during this process. To estimate the excited-state populations, we simulate the initialization pulse to the positive detuned regime.

To describe the qubit, we consider the effective model given by Eq. 4.3. This model, while an approximation, provides intuition on the interactions with the excited states. In the experiment, the initial detuning value

ranges from -400 to $-300\,\mu$eV (-97 to -73 GHz). Since the experimental pulses go from the negative far-detuned regime to the positive detuned regime, the exact initial detuning position is not relevant; hence, we choose $\varepsilon_0 = -350\mu$eV. The simulated pulse is simply $\varepsilon(t) = \varepsilon_0 + \varepsilon_h/t_g \cdot t$, where ε_h is the pulse height and t_g the duration of the pulse.

We consider the four different experimental pulses in Table 4.4, which are representative of the pulses used in this work. The three states with the highest initialization population are also shown in the table. The results show that the ground state is the most populated, and that there is non-negligible population in the first excited state, consistent with the experimental results reported in the main text. The third excited state, which has the next highest initialization population, is less populated and not observed in the experiments.

Table 4.4: Expected ground (ρ_0) and excited state ($\rho_{1,3}$) populations based on the pulse sequence used.

	Pulse 1	Pulse 2	Pulse 3	Pulse 4
ε_h (μeV)	680	646	612	816
t_g (ns)	6	6	6	9
ρ_0	0.841	0.873	0.872	0.864
ρ_1	0.082	0.083	0.082	0.076
ρ_3	0.054	0.023	0.026	0.038

4.2.7 S7: Pulses and pulse corrections

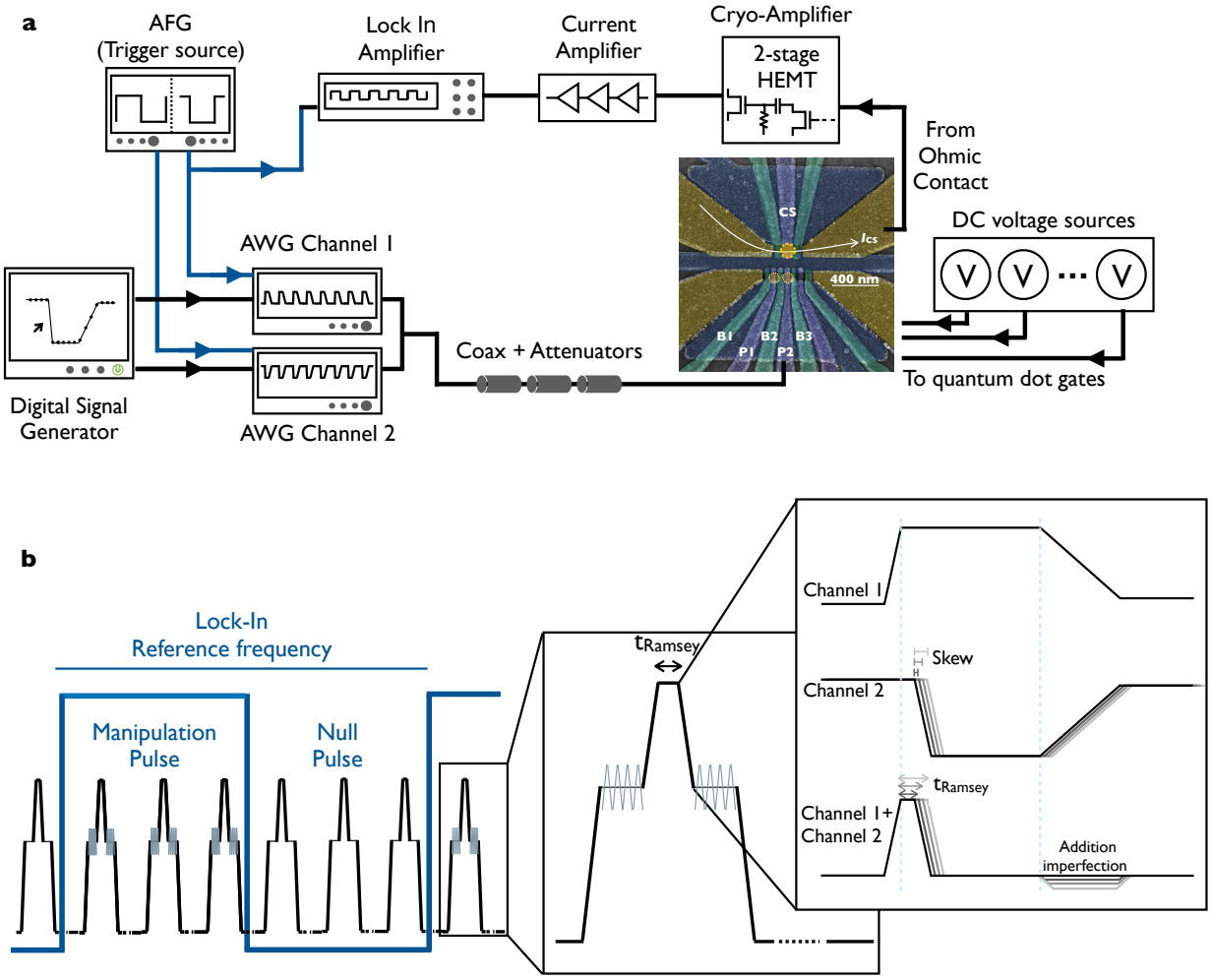

Figure 4.10: (a) Schematic of the experimental set up. The two AWG channels are needed only for Ramsey experiments to get the finest possible time step. (b) Schematic of the comparative pulse measurement as well as the two AWG channel combination method used for Ramsey sequences. .

Figure 4.10(a) shows the full electronics setup used in this experiment. Waveforms are produced digitally, and then pulses are generated using a two-channel Textronix AWG 70002A, which has a 25 GS/s sample rate. To achieve finer then a 40ps time steps for Ramsey sequences, the two channels can be combined and the relative skew between the two channels swept, resulting in a 5ps minimum time step. This channel addition is shown in Figure 4.10(b). We perform lock-in measurements at the frequency with which we modulate on and

off the manipulation pulses. For both the Ramsey and Rabi measurements, the null pulse used for comparison has the same DC structure without any microwave drive. Each pulse consists of a short manipulation phase followed by a longer measurement phase of typical duration 1.2μs. The typical modulation frequency used for lock-in reference is around 10kHz. The reported Ramsey fringes are the amplitude of the lock-in signal.

The pulse sequences we use consist of quasi-dc changes in detuning combined with ac microwave bursts. Because of the frequency dependent attenuation down the dilution refrigerator, we apply pulse corrections to make our dc pulses more similar to the intended shape. We use S21 measurements of the high frequency lines to determine the frequency dependent attenuation expected. We then take a FFT for a step function, and weight the spectrum according to our S21 measurements. An inverse FFT is taken to obtain the corrected pulse segment, which becomes the building block for our new pulse sequence. We apply the corrected building block for every change in dc level to our intended dc pulse sequence. This pulse sequence visually looks like an overcorrection of the pulse in order to counteract the measured finite rise-time. We finally add in any ac components to our pulses. After these pulse corrections, there is still an observable drift in the top of the pulse as a function of time for short times (Ramsey measurements). To place points on Fig. 4.4(b) it is important to know the detuning. Thus, we perform additional post-processing to the Ramsey data by shifting line scans with the function $A(1 + be^{-t/\tau})$ in order to align the dispersion minima of consecutive Ramsey oscillations. This allows us to accurately plot detuned Ramsey data for small times, such as the light yellow circles and orange triangles in Fig. 4.4(b). Here, A is the detuning pulse amplitude, $b = 0.2$, and $\tau = 1.8$ ns.

Chapter 5

Novel operation regimes of a 3D integrated cavity-dot system

This chapter presents measurement of a double-quantum-dot coupled to a superconducting cavity performed by driving the cavity with a microwave pulse sent from the quantum dot gate. This gate-based driving results in an enhanced transmission through the cavity at the interdot transition which is tunable with tunnel coupling between the two quantum dots. One potential explanation based on modulated longitudinal coupling between the dots and the cavity is presented and used to fit the transition peak under different regimes. Excited state readout of a QDHQ is performed using rapid dc pulses, and used to extract the singlet-triplet splitting in each dot. Finally, a proposal for reduced coax operation of such systems is included, based off the presented measurements.

5.1 Dispersive readout

All of the work presented in the previous chapters was performed using an auxilliary quantum dot coupled to the qubit as an integrated charge sensor. Since the charge sensing dot was capacitively coupled to the two dots which make up the qubit, changes in charge occupation at the double-quantum dot resulted in capacitive shifts of the charge sensor, affecting the

current measured through the dot. This is a widely used method of quantum dot qubit measurement, but requires an electron reservoir, barrier gates, screening gates and a plunger gate for each charge sensor and is therefore expensive in terms of space on sample and DC lines inside the fridge.

Another method of charge sensing is through gate-based dispersive readout either with an LC tank circuit [138–140] or coupled resonator [50, 141–143], as described in Fig. 5.1. This method is also made possible by the capacitance between the qubit and readout circuit, as shown in Fig. 5.1(a) which provides schematically a simplified circuit diagram for the sample described later in this chapter. Here, the dispersive measurement is achieved using a high impedance coplanar wave guide (CPW) which has capacitive connections to the lab on its input and output, as well as a DC tap and capacitive coupling to two quantum dot devices. The circuit has a relatively high-Q resonance, and the frequency of that resonance will experience capacitive shifts in response to changes in the qubit system as depicted in Fig. 5.1(b) with the dark (unshifted) and light (shifted) lines. Unlike a quantum dot charge sensor or QPC, dispersive readout mechanisms are not sensitive to total charge differences; instead, they are sensitive to changes in electron occupation with tunnel rates at or above the circuit's resonant frequency [138, 144–146].

Figure 5.1(c) shows schematically the two types of transitions that the cavity is most sensitive to: tunneling from a quantum dot to a reservoir with tunnel rate near or above the cavity frequency, and tunnel coupling between two coupled quantum dots with coupling rate near or above the cavity freqeuncy. Fig. 5.1(d) shows a charge stability diagram of a double-quantum dot measured using a CPW resonator with resonance frequency around 1.3 GHz. Here, a constant microwave drive at the resonance frequency was sent to the cavity input, and changes in the magnitude and phase of the transmitted signal were measured. Note how the transition lines fade out at too high and too low voltages. Though the axes in Fig. 5.1(d) are plunger gate voltages and not barrier gates, the cross-capacitance in the device means that increases in the plunger gate voltage will act to increase the effective barrier gate

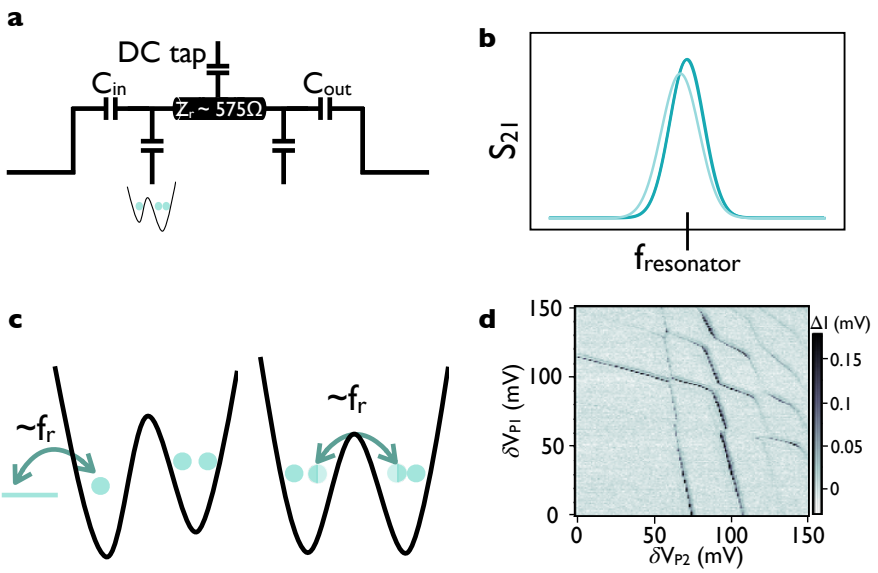

Figure 5.1: (a) Simplified circuit diagram for a cavity coupled to a quantum dot device similar to the one used in the experiments described below. (b) Dispersive readout is performed by probing the resonator circuit using a microwave tone at the resonance frequency and measuring transmission through the cavity. When charge movement occurs in the capacitively coupled quantum dots, the circuit experiences a capacitive shift of the resonance peak, leading to suppression of the transmission. (c) The cavity is most sensitive to movement in charge, particularly at rates near the cavity frequency. Such charge motion can arise from tunneling from a quantum dot to the electron reservoir, or tunneling between two quantum dots. (d) An example of a DQD sensed using dispersive readout. Faded transition lines indicate tunnel rates that are either above (higher values of $V_{P1,2}$) or below (lower values of $V_{P1,2}$) the cavity frequency.

---

voltage, softening the barrier and increasing the tunnel rate in the absence of any tuning compensation. Thus, the regions of strong and faded signal indicate an optimal voltage where the tunnel rates are most in resonance with the cavity. As suggested in Ref. [146], at tunnel rates below the resonant frequency, tunneling events between the dot and the reservoir are too slow to couple to the cavity fields; at tunnel rates above the resonant frequency, the transition lines broaden and the peak height decreases. This highlights how the dispersive method greatly reduces the total number of lines per sensor at the cost of bandpass filtering the readout signal.

For completeness, it is important to comment that CPW resonators have an additional benefit of potential long-range coupling of qubit clusters. Long range coupling of two spins

mediated by a cavity has been demonstrated [147,148], and shows a very promising approach for scaling to large numbers of qubit arrays. It also allows for a larger qubit-to-sensor ratio as compared with a quantum dot charge sensor, which has best sensitivity if limited to sensing 2-3 nearby quantum dots. An important part of the cavity mediated coupling between spin or charge qubits is strong coupling between qubit and cavity, and energy exchange between the electron and a single photon [87, 98, 149–151]. This limit was not investigated and is therefore outside the scope of the following work.

5.2 Dot-gate driven enhanced transmission

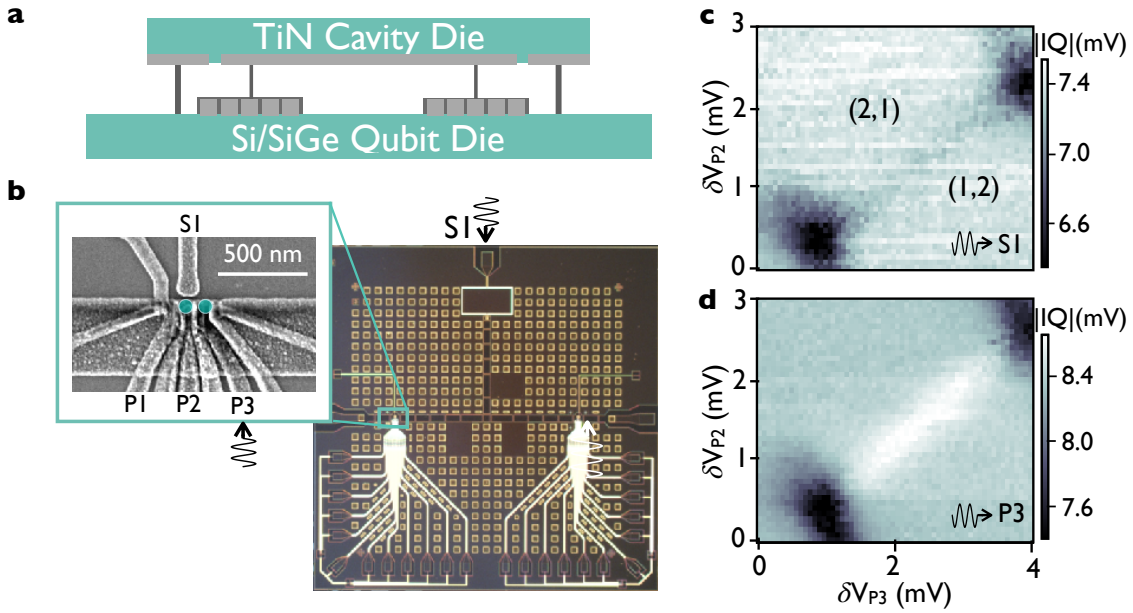

Figure 5.2: (a) Schematic of 3D integrated sample, where a high-impedance TiN resonator die is galvanically connected to a Si/SiGe quantum dot die. (b) Dark field optical microscope image of a completed qubit die chip. Inset shows a scanning electron microscope image of a sample nominally identical to the one used in these experiments. In this work, the cavity is driven using high-frequency lines connected to P3, and S1. (c,d) Dispersive measurements of a double quantum dot at the $(N_{P2}, N_{P3}) \rightarrow$ (2,1)-(1,2) charge configuration, measured by probing the cavity with a modulation on (c) S1 and (d) P3, with no changes in the electrostatic configuration of the quantum dots.

The work in Section 5.2-5.4 comprises a manuscript in preparation [152].

The sample used in this experiment is a 3D-integrated, high-impedance TiN $\lambda/2$ coplanar waveguide resonator die coupled to a Si/SiGe quantum dot die, consistent with that presented in Ref. [153]. The 3D nature of the device relieves both wiring and fabrication constraints; wiring by allowing more space on the qubit die for qubit lines and fanout, fabrication because the qubit and cavity chips are no longer constrained to have the same lithographic processes for fabrication. Fig. 5.2(a) shows a schematic of the device, where the qubit chip is capacitively coupled to the resonator chip through gate S1. A $\lambda/4$ segment shunted by a large parallel plate capacitor on the quantum dot die is used for voltage biasing of the coupling gate, S1. Galvanic contact between both dies is achieved using underbump metal pads placed at the voltage antinodes and at the end of the $\lambda/4$ DC tap. A dark field optical image of a completed qubit die chip is included in Fig. 5.2(b) with the inset showing a scanning electron microscope image of a device nominally identical to the one used in this experiment.

Figure 5.2(c,d) shows the interdot transition of a three-electron double quantum dot formed using gates P2 and P3 at the (N_{P2}, N_{P3}) $\rightarrow$ (2,1)-(1,2) charge configuration, measured by sending a modulation at the cavity frequency down gates S1 (Fig. 5.2(c)) and P3 (Fig. 5.2(d)). Because of the capacitive coupling between the qubit gates and the cavity through the coupling pin S1, these drives generate a cavity response with Q and SNR similar to driving the cavity at the input port. As compared with the dip in cavity transmission at the interdot transition when probing just the cavity via S1 (Fig. 5.2(c)), there is a clear enhancement in transmission when the drive is applied using P3 (Fig. 5.2(d)). There are no electrostatic changes to the tuning of the double dot between these scans, indicating the enhanced signal is unique to probing the cavity with P3 as opposed to S1. Since the double-quantum-dot is defined under dot gates P2 and P3, the microwave drive on gate P3 also generates a drive on double-dot-detuning ε, with strength $\alpha_{\varepsilon,P3}V_{ac}$.

Figure 5.3(a) demonstrates the dependence of the enhanced transmission response on the interdot tunnel coupling. At low tunnel coupling (i), the interdot transition produces a faint

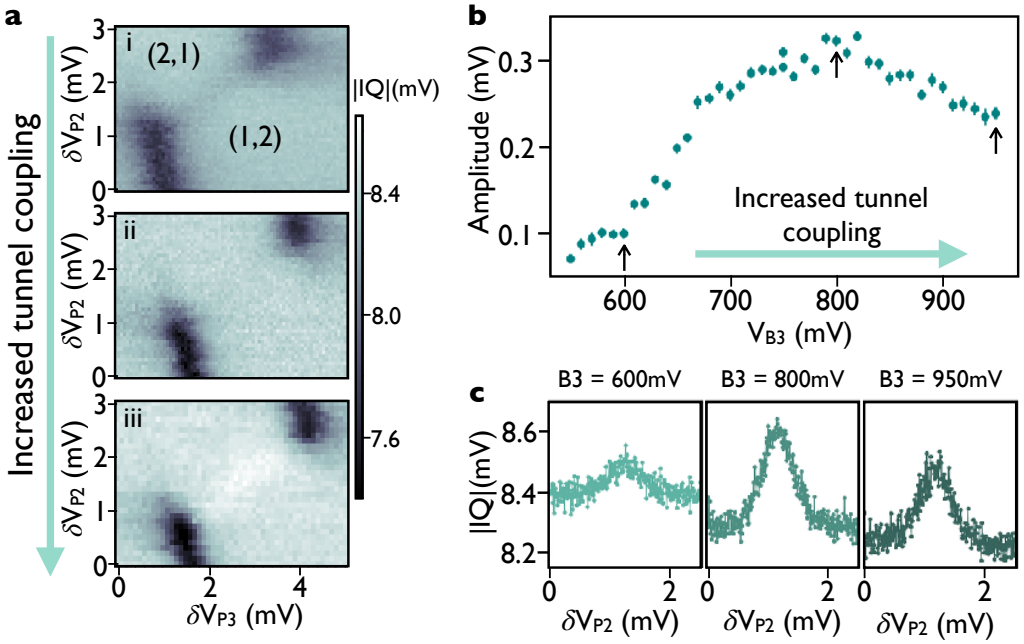

Figure 5.3: (a) Tunnel-coupling dependent enhancement of the cavity transmission across the interdot transition with modulation applied on gate P3, for three different tunings (i-iii). The cavity transmission shifts from a dip in (i) to a peak in (iii), passing through a region of no transmission change (ii). (b) Interdot transition transmission peak as a function of tunnel coupling, tuned using the barrier gate B3 between the two dots. There is first an increase in peak height from near zero to a maximum around 0.3mV, after which the peak starts to decay at even larger tunnel couplings. (c) Three line cuts at B3 values V_{B3} = 600, 800, and 950 mV.

---

suppression of the cavity transmission, more similar to the transmission dip in Fig. 5.2(c). At a larger tunnel coupling value (ii), there is no visible interdot transition, and at an even larger tunnel coupling (iii) the cavity transmission is enhanced across the interdot transition. The P3-driven plot in Fig. 5.2(d) is at a fourth tuning of larger tunnel coupling than (iii).

Further characterization of the transmission peak's tunnel coupling dependence is shown in Fig. 5.3(b), where the tunnel coupling is tuned by the barrier gate B3 between the two quantum dots. Here the peak of the interdot transition is fit with a $cosh^{-2}$ and the peak amplitude is extracted. Moving from lower to higher tunnel couplings within the range of V_{B3} = 550 to 700mV results in increased peak amplitude. At high enough tunnel couplings, this growth in amplitude slows and then starts to decrease in the range V_{B3} = 800 to 950mV.

The change from negative, to zero, to positive peak amplitude in Fig. 5.3(a) and the increase in peak amplitude in Fig. 5.3(b) from $V_{B3} = 550$ to 700mV is likely due to a 'turning-on' of an interaction or coupling, which we will call $g_?$. When this $g_?$ is low, the transmission peak is negative (ie Fig. 5.3(a)(i)), similar to a dispersive interaction from transverse coupling, $g_\perp$. When $g_?$ is equal in strength to $g_\perp$, these two couplings will cancel so that no peak is observed (Fig. 5.3(a)(ii)). As the $g_?$ strength is increased, the peak amplitude will also increase, as seen in Fig. 5.3(b). The decrease in peak amplitude at higher tunnel couplings Fig. 5.3(b) is likely similar to the decrease in charge-sensed, interdot-transition signal due to the line broadening.

5.3 Modulated longitudinal coupling

As mentioned earlier, cavity-based readout of quantum dot devices is a promising path towards long-range coupling of qubit clusters, with demonstrations of both spin-photon interactions [98,142,150,151] and photon mediated spin-spin interactions [147]. These works have focused on field-field coupling between the qubit and cavity, known as transverse coupling. However, there are many other types of couplings, like energy-energy interactions commonly denoted as longitudinal couplings. These longitudinal couplings are expected to be stronger, allow for faster gates, and be QND [154–159]. Both static [160–163] and modulated longitudinal couplings [164, 165] have been demonstrated experimentally in the superconducting qubit community. Though there have been many theoretical proposals about investigating these couplings in quantum dot qubits coupled to resonators, and recent work has measured a longitudinal coupling strength via interactions with a qubit [166], resonator readout of modulated longitudinal couplings has yet to be implemented.

Figure 5.4(b-d) shows schematically the three types of couplings expected for a qubit

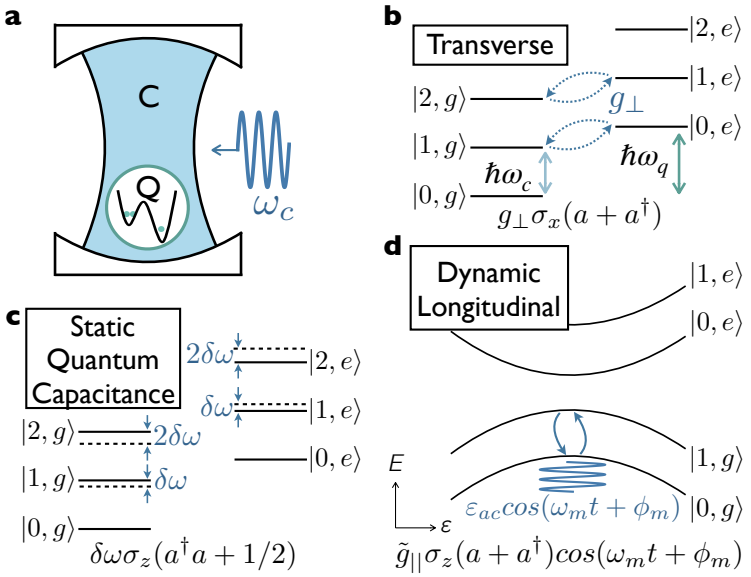

Figure 5.4: (a) Basic experimental setup, where a double quantum dot qubit is placed inside a cavity field. (b) Transverse coupling of the form $\sigma_x(a+a^\dagger)$ allows for transfer of energy between the qubit and cavity. (c) Static longitudinal coupling of the form $\sigma_z(a^\dagger a)$ generates energy shifts in the cavity (qubit) depending on the state of the qubit (cavity). (d) Dynamic longitudinal coupling of the form $\sigma_z(a+a^\dagger)cos(\omega_m t)$ generates changes in the cavity state and field strength due to both modulation of the qubit energy and the qubit state.

---

placed inside the field of a cavity, as seen in Fig. 5.4(a), using the dressed state of the qubit-cavity system, $|c,q\rangle$. Fig. 5.4(b) describes an interaction of the qubit and cavity fields $H_\perp/\hbar = g_\perp\sigma_x(a+a^\dagger)$, characterized by transverse coupling strength $g_\perp$. With transverse couplings, an excitation of the qubit state from $|g\rangle$ to $|e\rangle$ is accompanied by a reduction in the number of photons in the cavity. The next two couplings described in Figure 5.4(c,d) are considered 'curvature couplings', because their coupling strength is proportional to the curvature of the qubit's energy levels, $\frac{d^2(E_{01})}{d\varepsilon^2}$. The static longitudinal coupling $\delta\omega$, commonly known as the quantum capacitance, is depicted in Fig. 5.4(c), and is an interaction $H_{\delta\omega}/\hbar = \delta\omega(aa^\dagger+1/2)$ between the qubit and cavity energies. In this case, changes in the qubit state or photon number result in shifts in the energy ladder.

Figure 5.4(d) describes a dynamical longitudinal coupling $H_{||}/\hbar = \tilde{g}_{||}\sigma_z(a+a^\dagger)cos(\omega_m t+\phi_m)$ which is turned on when the qubit is driven at some ω_m near the cavity resonance

frequency. This dynamical coupling has two effects; modulation in the qubit detuning over regions of high curvature causes changes in the total number of photons in the cavity, and changes in the qubit state shift the overall field strength of the cavity. This type of coupling has been described in detail in Ref. [158, 159].

To investigate the origin of the enhanced interdot transmission described in the previous section, it is interesting to consider the possibility of a dynamical longitudinal coupling, as the measurement scheme includes an oscillating detuning drive at the resonator frequency. The IQ magnitude of the cavity transmission for a qubit in the ground (-) state as a function of detuning, measured using a homodyne detection scheme, is estimated as [152]

$$IQ_{-}(\varepsilon) = \frac{B(\tilde{\varepsilon}_d + \frac{1}{2}[\tilde{g}_{||}^{S1}(\varepsilon) - \tilde{g}_{||}^{P3}(\varepsilon)])}{\sqrt{[\chi(\varepsilon) + \delta\omega(\varepsilon)]^2 + \frac{\kappa^2}{4}}}. \tag{5.1}$$

Here, $\tilde{\varepsilon}_d$ is a classical drive on the cavity, $\tilde{g}_{||}^{S1}(\tilde{g}_{||}^{P3})$ is a longitudinal coupling induced by a detuning drive from the cavity coupling gate S1 (P3), $\chi(\varepsilon)$ is the usual transverse dispersive coupling, $\delta\omega(\varepsilon)$ is the static quantum capacitance coupling described in Fig. 5.4(c), and κ is the resonator damping.

To compare accurately with the experiments described in Fig. 5.2, $\tilde{g}_{||}^{P3}$ is nonzero only when the modulation is applied to P3, and $\tilde{g}_{||}^{S1}$ will always be finite with magnitude given by the effective drive on S1, causing small fluctuations in ε. Because of the large singlet-triplet splittings in each double quantum dot, as discussed below, $\tilde{g}_{||}$, χ, and $\delta\omega$ are computed for a charge qubit, resulting in

$$\tilde{g}_{||} = \frac{\omega_r}{2}\frac{\eta}{\hbar}\frac{4t_c^2}{[\varepsilon^2 + 4t_c^2]^{3/2}} e\tilde{V}_{m(,c)}, \tag{5.2}$$

$$\chi = \frac{g_{\perp}^2}{\Delta} = \left(\frac{\omega_r}{2}\frac{\eta}{\hbar}\right)^2 \frac{4t_c^2}{[\varepsilon^2 + 4t_c^2]}\frac{1}{\omega_r - \omega_q}, \tag{5.3}$$

$$\delta\omega = \hbar\left(\frac{\omega_r}{2}\frac{\eta}{\hbar}\right)^2 \frac{8t_c^2}{[\varepsilon^2 + 4t_c^2]^{3/2}}. \tag{5.4}$$

$\tilde{\varepsilon}_d$ is approximated as $\tilde{\varepsilon}_d = \frac{\Delta x_0 F_0}{2\hbar}$ with zero point fluctuation $\Delta x_0 = \sqrt{\frac{\hbar}{2\omega_r L_r}}$ and force amplitude $F_0 = \alpha \tilde{V}_{m,c}$ [152]. Here, $V_{m,c}$ is used to refer the the voltage modulation on the cavity pin, S1, used in $\tilde{g}_{||}^{S1}$ and $\tilde{\varepsilon}_d$, and V_m is reserved for voltage modulation on the P3 dot gate. A global negative is in front of $\tilde{g}_{||}^{P3}$ in Eq.5.1 because of the opposite dependence on ε a modulation from P3 will have as compared with modulations from the cavity pin, S1.

Fig. 5.5(a,b) plot in teal line cuts across the interdot transition lines seen in Fig. 5.2(c,d). In yellow are fits as a function of double-quantum dot detuning ε to Eq.5.1. An estimated cavity Q = 9000 and the cavity resonance frequency f_r = 1.3 GHz were used in each fit, as well as an estimated detuning alpha with respect to gate P2 $\alpha_{\varepsilon,P2} = 0.13$, used to convert the data from volts to μeV. Fig. 5.5(a) was fit holding $\tilde{g}_{||}^{P3} = 0$, extracting an overall constant B = 0.00228, coupling to the cavity α_c=0.058, tunnel coupling t_c=7.47 GHz, and voltage

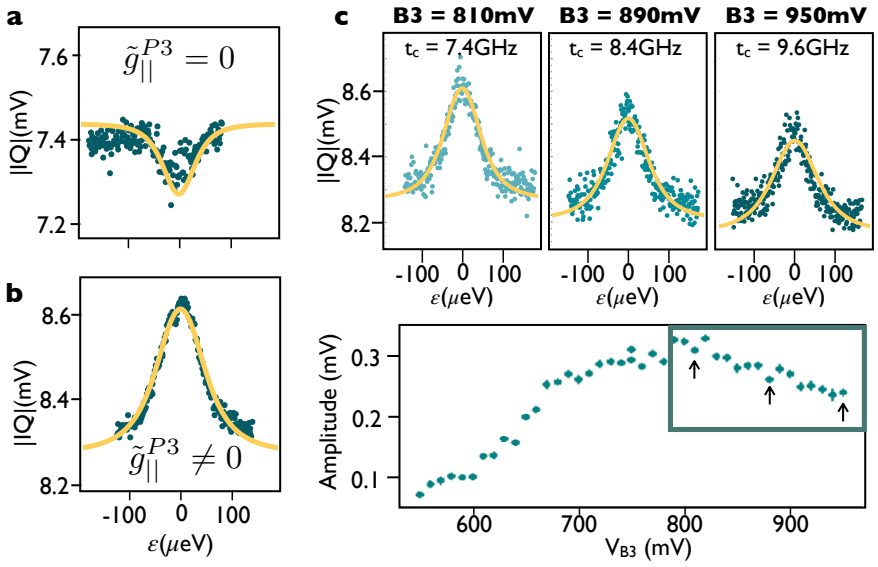

Figure 5.5: (a,b) Line cuts across the interdot transition lines of the plots shown in Fig. 5.2(c,d) with fits in yellow using the expression for IQ given by Eq. 5.1. (c) The same data showing the interdot peak amplitude as a function of coupling as seen in Fig. 5.3(b,c), now with three line cuts at B3 values V_{B3} = 810, 890, and 950 mV. Each line cut is fit to Eq. 5.1 resulting in t_c = 7.4, 8.4, and 9.6 GHz, respectively.

modulation $V_{m,c} = 18\ \mu$V.

Using all of these values, Fig. 5.5(b) is then fit for both $V_{m,c}$ and V_m, the modulation in detuning on P3 used in $\tilde{g}_{||}^{P3}$. $V_{m,c}$ is re-fit since the experimental drive is slightly different between driving on the S1 and P3 gates, as seen in the different background value of $|IQ|$ in Fig. 5.5(a,b). The fitted values for Fig. 5.5(b) are $V_{m,c} = 19.7\ \mu$V and $V_m = 147.5\ \mu$V. This value of V_m is consistent with the on-chip peak-to-peak voltage estimates given the attenuation in the lines and power applied, and indicates the voltage at the sample. To get the voltage on the dot, these values would be multiplied by the corresponding gate-to-dot lever arms, which in these fits are lumped in to the overall constant B. The ratio $V_{m,c}/V_m$=0.13 gives an estimate for relative drive strength going to the cavity when driving using the P3 gate.

Figure 5.5(c) looks at three line cuts for $V_{B3} = 810$, 890, and 950 mV, and fits them using Eq. 5.1 with fits plotted in yellow. For each fit, the parameters from Fig. 5.5(b) are held constant, and are fit for t_c and α_c. A slight change in α_c with changing t_c can be understood with movement of the quantum dots; a higher tunnel coupling will bring the two quantum dots closer together, and a lower tunnel coupling will separate them further apart. These changes can then impact how strongly the cavity coupling gate will couple to the double-quantum-dot system.

The resulting tunnel couplings for each curve in Fig. 5.5(c) are $t_c = 7.4$, 8.4, and 9.6 GHz, with $\alpha_c = 0.0584$, 0.058, and 0.0577 respectively. For Eq. 5.1, the peak height at $\varepsilon = 0$ increases as t_c decreases and approaches f_R, which is not seen in the experimental data. As Eq. 5.1 describes the system in the dispersive, adiabatic limit ($t_c >> f_r$), it is likely only valid at the large tunnel coupling limit $V_{B3} = 800$ to 950mV. The increasing amplitude in the range $V_{B3} = 500$ to 800mV could be due to the system becoming more adiabatic with respect to the applied drive, such that more curvature is sampled and the modulated longitudinal coupling is increased.

It is worth noting that Fig. 5.5(c) presents a relatively wide range of tunnel couplings,

all larger than the cavity frequency, that have finite peak height. This is compared with typical dispersive readout of double quantum dots where the maximum transmission amplitude signal at the polarization line occurs when the qubit energy ($2t_c$) is near the resonant frequency [142]. The decoupling of tunnel coupling and cavity frequency will allow for wider flexibility of qubit Hamiltonians, particularly for that QDHQ for which the shape of the qubit energy dispersion is governed by ground and excited state tunnel couplings, as described in Chapter 3. Relaxing the constraint that $2t_c \approx f_r$, particularly in favor of $2t_c > f_r$, will make this readout regime more easily attainable while maintaining favorable qubit parameters.

5.4 Excited-state readout of a QDHQ

As described above, a readout resonator coupled to a double quantum dot will be sensitive to charge movement, both from a dot to an electron reservoir and between two quantum dots. For a QDHQ, where the qubit Hamiltonian is engineered to have charge and spin-like regimes, locations in ε where cavity-based readout is possible are limited. Fig. 5.6(a) highlights the far detuned limits of the qubit energy eigenvalues in red; in these regions, the qubit is spin-like and both levels have the same charge configuration. Thus, there is no charge movement when transitioning between qubit levels and the cavity will be insensitive to these changes. Fig. 5.6(a) highlights the Δ_1 charge anticrossing in orange; while there is charge movement at this anticrossing and readout is possible, the qubit would have to be adiabatically transformed from the manipulation region (far detuned) to the anticrossing ($\varepsilon = 0$). This brings the qubit through the region most sensitive to charge noise and could introduce dephasing.

Readout can instead be performed at the excited state anticrossings, highlighted in yellow in Fig. 5.6(a). Here, the qubit can be manipulated in the far positive (negative) ε and adiabatically pulsed to a detuning value centered with the Δ_2 (Δ_3) anticrossing. If the qubit is in the ground state, no readout will occur; however, if the qubit is in the excited state,

it will be brought to the $\Delta_{2,3}$ anticrossing and excited-to-ground state tunneling events are allowed. After this readout, initialization through decay process or state pumping must be

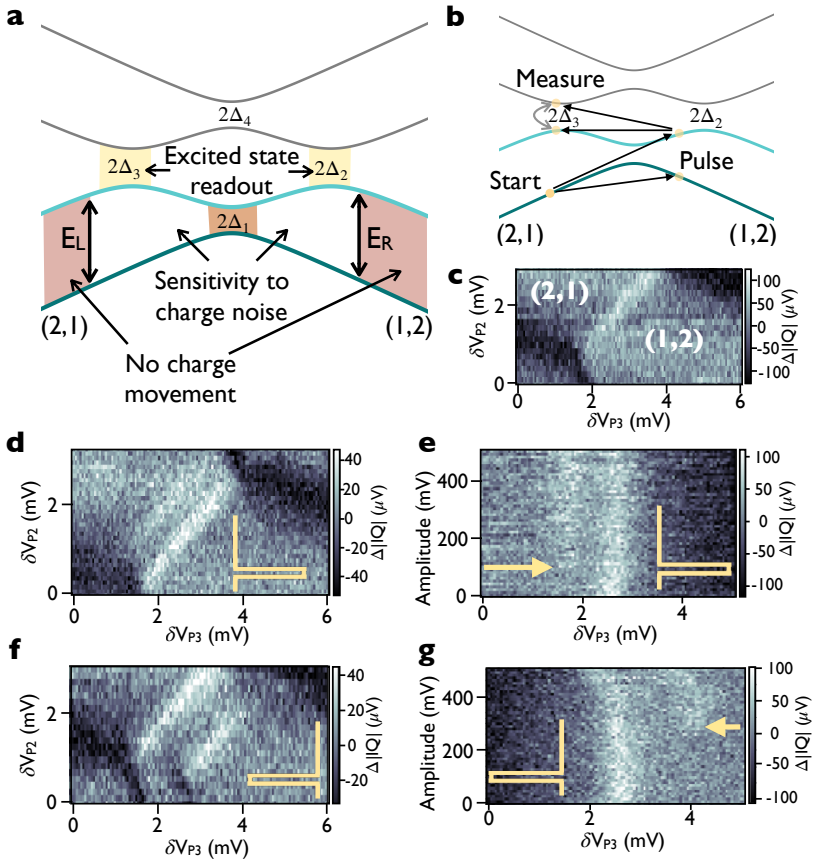

Figure 5.6: (a) Constraints for resonator-based readout of a QDHQ. (b) Experiment description for a right-moving pulse. Starting in the (2,1) configuration, a rapid dc pulse through $\varepsilon = 0$, across the polarization line, will result in a beam splitting effect and finite population into the excited state branch. Returning the pulse to the start location will maintain excited state occupation, and allow for tunneling events at the $2\Delta_3$ anticrossing, which can be sensed by the cavity. A similar experiment can be done pulsing the other direction, and will result in $2\Delta_2$ tunneling events. (c) Polarization line at the (2,1)-(1,2) region, with no dc pulse applied for comparison. (d) The same polarization line as in (c) at the same device tuning, now with a right-moving dc pulse, as described in (b). This produces a doubled polarization line to the left of the original. (e) Measuring across the doubled polarization line as a function of dc pulse amplitude. An amplitude threshold must be met in order for the doubling to occur, after which the spacing between both peaks remains constant. (f) The same experiment as in (d) except with a left-moving dc pulse. This produces a doubled polarization line the right of the original. (g) The same experiment as in (d) except with a right-moving dc pulse. Note the difference in threshold amplitude and distance between original and doubled polarization line peaks, indicating asymmetry in the $\Delta_{2,3}$ anticrossing locations.

performed.

The rest of Fig. 5.6 demonstrates excited-state readout of a QDHQ at its excited-to-ground state charge anticrossings by applying a fast dc pulse similar to the Larmor experiments described in Ref. [54, 65]. Fig. 5.6(b) describes the diabatic pulsed experiment for a right-moving (positive detuning) pulse traversing the QDHQ energy levels, where the logical $|0\rangle$ ($|1\rangle$) is shown in dark (light) teal. The pulse starts at negative ε such that the ground state of the system is the (2,1) configuration. Then, ε is changed abruptly to positive ε. Traversing the Δ_1 charge anticrossing in this way will have a beam-splitting effect, generating finite population in the excited state with Landau-Zener probability $P_1 = P_{LZ} = exp(\frac{-2\pi\Delta_1^2}{4v})$ where v is the pulsing velocity [167]. After a short wait time, ε is changed again to return to its original value. This will leave some fraction of the state population in the excited state, roughly given by $P_1(1 - exp(\frac{-2\pi\Delta_3^2}{4v}))$, allowing for $2\Delta_3$ tunneling events to occur at the excited state anticrossing. For qubit operation, this method will allow for mapping of the qubit state from large negative (positive) detuning to the Δ_3 (Δ_2) anticrossing; the cavity will only generate a response when the qubit is in state $|1\rangle$, not $|0\rangle$. Because the excited state anticrossing is located at the qubit dispersion rollover, and this rollover occurs where $\varepsilon \approx E_{ST}$, measuring the location of this anticrossing is also a good approximation to the singlet triplet splitting, similar to the spectroscopy done in Ref. [168].

Figure 5.6(c) shows a stability diagram at the (2,1)-(1,2) anticrossing with no pulse applied; the cavity is being driven by sending a microwave pulse at the resonance frequency down an rf-line connected to the P3 gate, as described above, resulting in positive changes in the magnitude of the cavity transmission, as seen at the polarization line in Fig. 5.6(c). To generate a sufficiently diabatic pulse for this experiment, the ground-to-ground state tunnel coupling Δ_1 had to be somewhat small, and thus the peak amplitude at the charge anticrossing in Fig. 5.6(c) is relatively small as compared with other data at higher tunnel couplings shown in the previous sections.

Figure 5.6(d) shows a stability diagram at the same tuning as Fig. 5.6(c) with the pulse

described in Fig. 5.6(b) applied. Since the pulse is right-moving, the doubled polarization line appears to the left of the original. Note that the doubled polarization line also generates enhancement in the cavity transmission signal of similar strength; this indicates that $\Delta_3 \approx \Delta_1$. Fig. 5.6(e) plots the polarization line doubling as a function of dc pulse amplitude. At a threshold voltage of around 100 mV, the doubling appears, and at higher voltages the two lines remain parallel. This threshold indicates the distance from the excited state anticrossing to the ground state anticrossing; if the pulse is too short to reach $\varepsilon = 0$, no beam splitting will occur and no excited state population is generated. Once the pulse can cross $\varepsilon = 0$, excited state population is always generated and is not dependent on the pulse amplitude.

Figure 5.6(f,g) are the same measurements as Fig. 5.6(d,e) except with a left-moving (negative detuning) pulse instead of a right-moving one. This generates a doubling of the polarization line to the right of the original, indicating excited state transitions at the Δ_2 anticrossing. When comparing Fig. 5.6(e,g), it becomes clear that the singlet-triplet splittings in the two quantum dots are different. This can be seen in the difference in threshold voltage and the separation between the original and doubled polarization lines, both of which equate to the singlet triplet splitting. Using an estimated α_ε of 0.13, the singlet-triplet splitting in the left (right) dot is estimated to be 116 (195) μeV. Due to such high singlet-triplet splittings, microwave operation of these qubits were out of reach of the physical instruments in the lab; however, this work presents the viability of such operation and measurement in the future.

5.5 Proposals for reduced-coax readout

Though dispersive readout reduces the number of DC lines needed for device operation as compared with quantum dot charge sensors, it increases the number of high frequency coaxial cables (rf coax) which are larger than dc lines and can take up more surface area per line

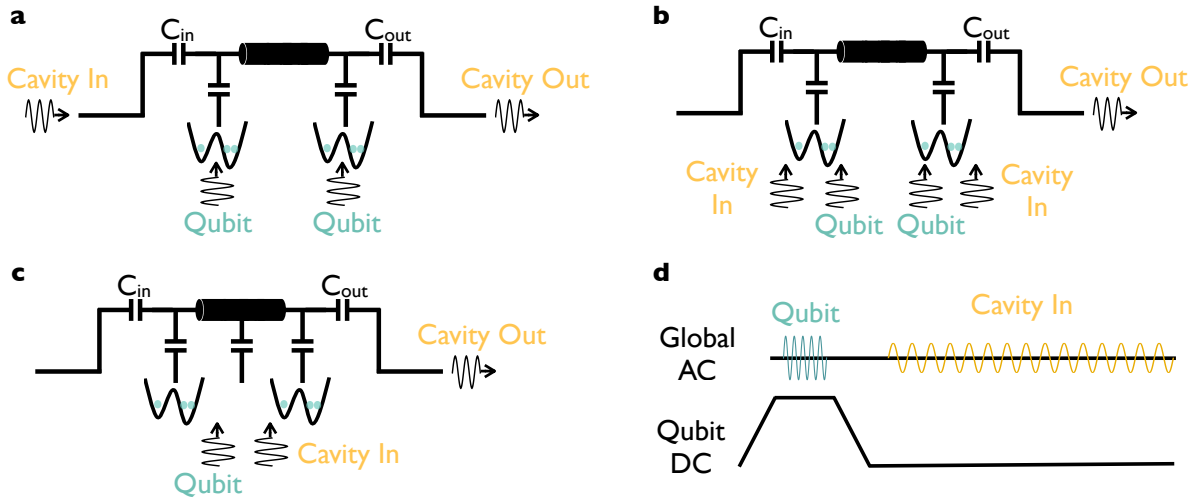

Figure 5.7: (a) Intended operation for the device used in the experiments above, and other state-of-the-art experiments of cavity mediated two-qubit coupling. (b) Proposed measurement scheme using the setup presented above, where the cavity is instead driven with the rf coax dedicated for qubit control. This reduced the number of coaxial lines by 1 for a two qubit device mediated and measured by a cavity. (c) Further reduction achieved with a global rf gate, more similar to the idea of an ESR line, which would send microwave pulses for all the qubits present as well as the cavity. This would lower the bandwidth requirements to just dc pulsing for the qubit rf (or mid frequency) lines. (d) Operation of a global rf gate would just require synching of the microwave pulses and dc pulses, such that the qubit microwave drive is sent down during the manipulation portion of the dc pulse and the cavity drive is sent down at the measurement portion.

---

on the cold plates of the dilution refrigerator due to the requirements for attenuation and thermalization. Thus, for true scalability, the number of rf coax has to be minimized, as expressed in proposals for large scale spin qubit arrays [107, 108].

Figure 5.7 describes two methods to reduce the total number of rf coax, based on the previously demonstrated experiments. Fig. 5.7(a) plots a simple circuit schematic similar to the one shown in Fig. 5.1(a), where there are four rf coax required for two qubits coupled by a CPW resonator; the cavity input and output lines and two control lines for each qubit. This model itself could be reduced by one line by optimizing the readout circuit for reflection as opposed to transmission. An alternative to the traditional setup as described in Fig. 5.7(a) is that shown in Fig. 5.7(b), where the rf coax intended for qubit control can also send down a microwave drive for the cavity, reducing the cavity's rf coax requirement to just an output

line. This is what was achieved in the above experiments.

Fig. 5.7(c,d) describes an even further reduction of rf cabling, where there is only one local rf gate for each qubit cluster. This gate would send down microwave pulses for both the qubit and cavity, leaving the qubit lines only requiring dc pulsing. For most qubit control, the dc pulses are adiabatic which have much lower frequency bandwidth constraints as compared with those intended for rf control. A combination of pulse sequences is shown schematically in Fig. 5.7(d), where a microwave pulse for qubit control is synchronized with the manipulation portion of the dc pulse, and a microwave pulse for cavity readout is synchronized with the measurement portion of the dc pulse. With this method, the two qubit cluster that originally needed 4 rf coax to control both qubits and to read out the cavity only needs 2 rf coax: one to send down qubit and cavity microwave pulses and one to measure the cavity response. If each arm of the cavity had not one but multiple qubits, such as two or three single-spin qubits, the benefit of a global rf gate would be even greater. Manipulation of individual qubits with different qubit energies would involve sequential microwave pulses at different frequencies, similar to multi-qubit experiments done with ESR lines [36]. This may be coupled with dc pulsing of the qubit detuning or other parameters to avoid off-resonance driving of qubits which share a global rf gate.

Chapter 6

Appendix

6.1 Additional Ramsey and Larmor data

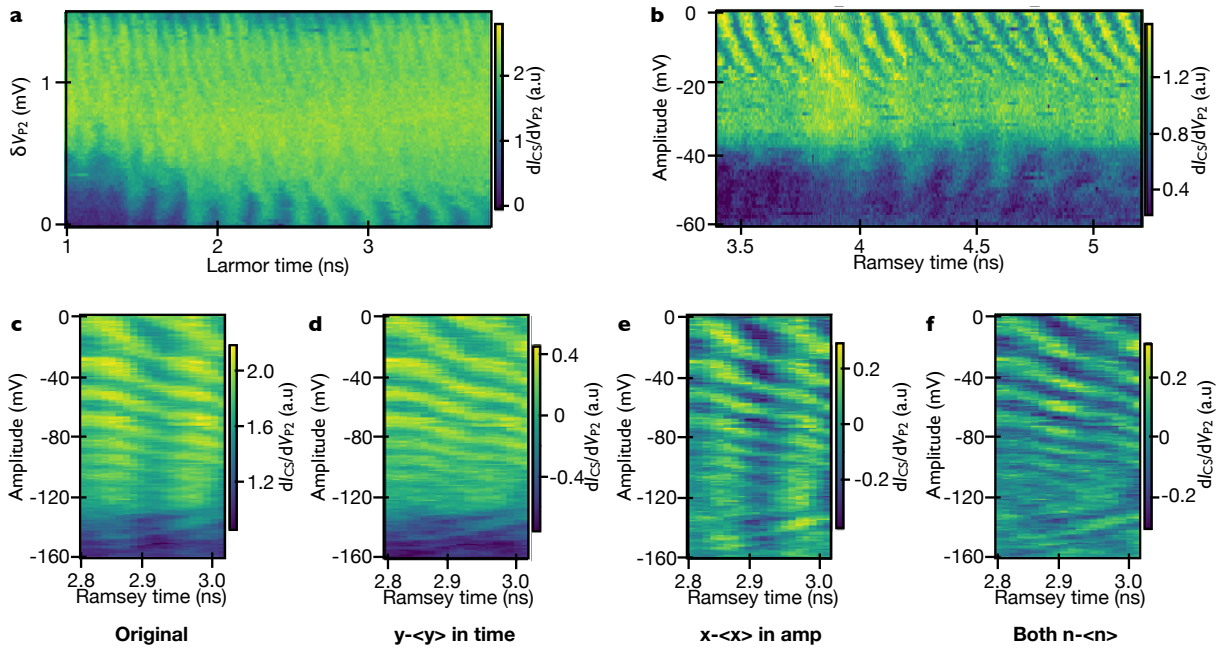

Figure 6.1: (a) Larmor oscillations at the same tuning as Fig. 3.3(a,b). (b) Ramsey oscillations with diabatic dc pulse used for the points near zero detuning in Fig. 3.3(b). (c) Original data from Fig. 3.3(c). (d) Background subtracted from (c) for every time step/amplitude sweep. (e) Background subtracted from (c) for every amplitude step/time sweep. (f) Background subtracted from (c) in both the time and amplitude directions.

Figure 6.1 includes additional data for use in understanding Fig. 3.3. Fig. 6.1(a) shows Larmor oscillations taken at the same device tuning as the measurements in Fig. 3.3(a), where the pulse sequence consists of a diabatic dc pulse with with no explicit ramp time which stays at it's dc height for some time given by the x axis, Larmor time. In this measurement, the resulting oscillations occur with characteristic frequency given by the qubit energy at a given location in detuning. The oscillations in Fig. 6.1(a) have a high frequency (fast oscillations) around 10 GHz for far detuning (high δV_{P2}) and a low frequency (slow oscillations) around 5 GHz at low detuning. These two values give estimates for the QDHQ qubit dispersion as governed by the singlet triplet splitting $E_{ST}/\mathrm{h} = 10$ GHz, and the charge anticrossing energy as governed by $2\Delta_1 = 5$ GHz.

Figure 6.1(b) shows similar measurements at the same device tuning performed using a detuned-Ramsey pulse sequence. As compared with the other detuned-Ramsey measurements described in Chapters 2, 3, and 4, here the detuning pulse between the two $\pi/2$ pulses has zero ramp time and is therefore more similar to a Larmor pulse. The intention in this measurement was to measure Ramsey measurements similar to those plotted in Fig. 3.3(a) while also probing the dispersion minimum at $\varepsilon = 0$, allowing for more accurate estimation of the dispersion minimum and the Hamiltonian parameters. The faint oscillations in Fig. 6.1(b) around -40mV in amplitude have oscillation frequency and shape very similar to those around $\delta V_{P2} = 0$ in Fig. 6.1(a), and so were attributed to the charge anticrossing and used for the points at the minimum in Fig. 3.3(b).

The data in Fig. 6.1(c-e) demonstrate the various signal subtractions used to get the data in Fig. 3.3(c), which is replotted in Fig. 6.1(f). Starting with the unmanipulated, raw data in Fig. 6.1(c), Fig. 6.1(d) shows the data with background subtracted for a set point in time. This is done by averaging all the points for a set time (i.e. 2.8ns), and subtracting that value from every point at that time. Fig. 6.1(e) does a similar operation, except subtracting the average background for a set amplitude (i.e. -80mV). In comparing Fig. 6.1(d) and Fig. 6.1(e), it is clear that subtracting the background in time gets ride of the

global enhancement in signal in the 2.8-2.9 ns ranges and 2.9-3.0 ns ranges that is present at essentially every point in amplitude, while subtracting the background in amplitude gets ride of the global changes in background and peak signal present as a function of amplitude, likely due to changes in the readout quality. Fig. 6.1(f) demonstrates the signal with both background subtractions, with which you can more easily make out oscillations at amplitudes below -80 mV.

6.2 DC Pulse correction

When doing Larmor or Ramsey measurements at short time scales, frequency dependent attenuation in the cabling used to send the dc pulses can cause signal drift as a function of detuning. This is because the attenuation will cause an unintended rise time of the dc pulse, so the pulse at short times is not reaching as far in amplitude as the pulse at longer times. This can make it difficult to accurately fit the data as a function of detuning, particularly if the oscillations in question are not as coherent at longer time scales when the pulse sequence is more stable. This section will discuss a signal correction method used to adjust for an expected rise time by overcorrecting the pulse.

A piecewise function was generated to fit the frequency-dependence of the S_{21} transmission measurments through the high frequency line of the fridge shown in Fig. 6.2(a). Note that these measurements do not include any effects of the sample board or the sample itself. However, transmission measurements could be done of board using wirebonds from one rf pad to another to characterize the board and typical wirebond performance, allowing for better estimates of any frequency dependent performance of these elements.

For a given frequency, the amount of frequency dependent attenuation is calculated as attenuation = $10^{(\Delta S_{21})/20)}$ where ΔS_{21} indicates the difference of transmission as compared with the low frequency value, 23.6dB. Using the piecewise function, the frequency dependent correction for a single impulse (ie: an immediate step from 0 to 1) is calculated by first

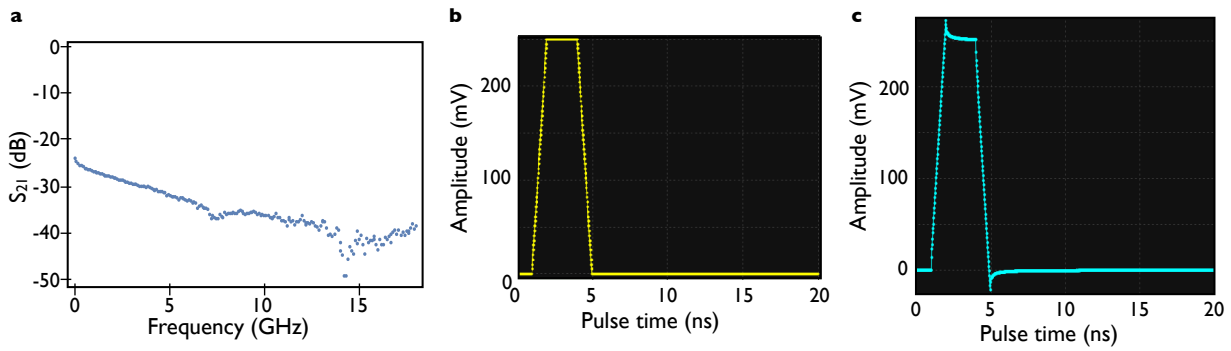

Figure 6.2: (a) S_{21} transmission for the high-frequency line used in the experiments in Chapters 2-4. (b) Intended dc pulse for a qubit operation, as generated on a digital waveform generator. (c) Corrected pulse from (b), generated by taking the FFT of an extrapolated version of (a) and using it as a transfer function for (b).

---

generating a step function and taking it's Fourier transform. It is important to shift the spectrum so that it's zero-frequency component is at the center (fftshift in python). Next, an array of discrete Fourier transform sample frequencies is generated to reflect the experimental time-step corresponding to the outgoing signal's point spacing (fftpack.fftfreq). A transfer function T is created using this discrete array of frequencies as inputs to the piecewise transmission function, such that the corrected FFT will be $\frac{FFT}{T}$.

The final correction to a single impulse will be the inverse FFT of the corrected Fourier spectrum. Once this is calculated, the impulse correction has to be applied for the entire dc waveform. This can be done in many ways — in the current version of the FFT corrected Badger Signal Generator, the code looks for each instance of a change in voltage in the dc waveform, and for each change multiplies the correction for a single impulse by the magnitude of the voltage change. Thus, larger, more abrupt steps in voltage will get a larger correction, and more adiabatic changes will need less correction.

All of this is currently done before adding in any microwave pulses to the sequence. The microwave pulses will also be impacted by the frequency dependent attenuation by making certain drive frequencies (particularly larger frequencies) weaker on chip for the same strength drive at the instrument level.

Figure 6.2(b) shows an example dc pulse that may be used for qubit control, and Fig. 6.2(c) shows the corrected version of the pulse using the transmission from Fig. 6.2(a). Note how both the increasing and decreasing portions of the pulse receive corrections. On a practical level, it is important to ensure the corrections fall within the voltage range of the AWG in use, which for the Tektronix 70001,2 is $\pm$ 250mV.

Bibliography

[1] Paul Benioff. The computer as a physical system: A microscopic quantum mechanical hamiltonian model of computers as represented by turing machines. *J Stat Phys*, 22:563, 1980.

[2] Richard P. Feynman. Simulating physics with computers. *International Journal of Theoretical Physics*, 21(6):467, May 1982.

[3] Paul Benioff. *Phys Rev Lett*, 48:1581–1585, Jun 1982.

[4] D Deutsch. Quantum-theory, the church-turing principle and the universal quantum computer. *P. Roy. Soc. Lond. A Mat.*, 400(1818):97–117, Jan 1985.

[5] Artur K. Ekert. Quantum cryptography based on bell's theorem. *Phys. Rev. Lett.*, 67:661, 1991.

[6] S Lloyd. Universal quantum simulators. *Science*, 273(5278):1073–1078, Jan 1996.

[7] Michael A. Nielsen and Isaac L. Chuang. *Quantum Computation and Quantum Information: 10th Anniversary Edition*. Cambridge University Press, Cambridge, Jan 2011.

[8] Juan Yin, Yuan Cao, Hai-Lin Yong, Ji-Gang Ren, Hao Liang, Sheng-Kai Liao, Fei Zhou, Chang Liu, Yu-Ping Wu, Ge-Sheng Pan, Li Li, Nai-Le Liu, Qiang Zhang, Cheng-Zhi Peng, and Jian-Wei Pan. Lower bound on the speed of nonlocal correlations without locality and measurement choice loopholes. *Phys. Rev. Lett.*, 110:260407, Jun 2013.

[9] Craig Gidney and Martin Ekerå. How to factor 2048 bit RSA integers in 8 hours using 20 million noisy qubits. *Quantum*, 5:433, 2021.

[10] Frank Arute, Kunal Arya, Ryan Babbush, Dave Bacon, Joseph C Bardin, Rami Barends, Rupak Biswas, Sergio Boixo, Fernando G S L Brandao, David A Buell, Brian Burkett, Yu Chen, Zijun Chen, Ben Chiaro, Roberto Collins, William Courtney, Andrew Dunsworth, Edward Farhi, Brooks Foxen, Austin Fowler, Craig Gidney, Marissa Giustina, Rob Graff, Keith Guerin, Steve Habegger, Matthew P Harrigan, Michael J Hartmann, Alan Ho, Markus Hoffmann, Trent Huang, Travis S Humble, Sergei V Isakov, Evan Jeffrey, Zhang Jiang, Dvir Kafri, Kostyantyn Kechedzhi, Julian Kelly, Paul V Klimov, Sergey Knysh, Alexander Korotkov, Fedor Kostritsa, David Landhuis, Mike Lindmark, Erik Lucero, Dmitry Lyakh, Salvatore Mandr, Jarrod R Mcclean, Matthew Mcewen, Xiao Megrant, Anthony andMi, Kristel Michielsen, Masoud

Mohseni, Josh Mutus, Ofer Naaman, Matthew Neeley, Charles Neill, Murphy Yuezhen Niu, Eric Ostby, Andre Petukhov, John C Platt, Chris Quintana, Eleanor G Rieffel, Pedram Roushan, Nicholas C Rubin, Daniel Sank, Kevin J Satzinger, Vadim Smelyanskiy, Kevin J Sung, Matthew D. Trevithick Trevithick, Amit Vainsencher, Benjamin Villalonga, Theodore White, Jamie Yao, Yeh Ping, Adam Zalcman, Hartmut Neven, and John M. Martinis. Quantum supremacy using a programmable superconducting processor. *Nature*, 574:505–510, Oct 2019.

[11] Yullin Wu, Wan-Su Bao, Sirui Cao, Fusheng Chen, Ming-Cheng Chen, Xiawei Chen, Tung-Hsun Chung, Hui Deng, Yajie Du, Daojin Fan, Ming Gon, Cheng Guo, Chu Guo, and more. Strong quantum computational advantage using a superconducting quantum processor. 2021. preprint arXiv:2106.14734.

[12] Abhinav Kandala, Antonio Mezzacapo, Kristan Temme, Maika Takita, Markus Brink, Jerry M Chow, and Jay M Gambetta. Hardware-efficient variational quantum eigensolver for small molecules and quantum magnets. *Nature*, 549:242–246, Sept 2017.

[13] Frank Arute, Kunal Arya, Ryan Babbush, Dave Bacon, Joseph C. Bardin, Rami Barends, Sergio Boixo, Michael Broughton, Bob B. Buckley, David A. Buell, Brian Burkett, Nicholas Bushnell, Yu Chen, Zijun Chen, Benjamin Chiaro, Roberto Collins, William Courtney, Andrew Demura, Sean andDunsworth, Edward Farhi, Austin Fowler, Brooks Foxen, Craig Gidney, Marissa Giustina, Rob Graff, Steve Habegger, Matthew P. Harrigan, Alan Ho, Sabrina Hong, William J. Ioffe Lev Huang, Trentand Huggins, Sergei V. Isakov, Evan Jeffrey, Zhang Jiang, Cody Jones, Dvir Kafri, Julian Kechedzhi, Kostyantyn Kelly, Seon Kim, Paul V. Klimov, Alexander Korotkov, Fedor Kostritsa, David Landhuis, Pavel Laptev, Mike Lindmark, Erik Lucero, Orion Martin, John M. Martinis, Jarrod R. McClean, Anthony McEwen, Matt Megrant, Xiao Mi, Masoud Mohseni, Wojciech Mruczkiewicz, Josh Mutus, Matthew Naaman, Ofer Neeley, Charles Neill, Hartmut Neven, Murphy Yuezhen Niu, Thomas E. O'Brien, Andre Ostby, Eric Petukhov, Harald Putterman, Chris Quintana, Pedram Roushan, Nicholas C. Rubin, Kevin J. Sank, Daniel Satzinger, Vadim Smelyanskiy, Doug Strain, Marco Sung, Kevin J. Szalay, Tyler Y. Takeshita, Amit Vainsencher, Theodore White, Nathan Wiebe, Z. Jamie Yao, Ping Yeh, and Adam Zalcman. Hartree-fock on a superconducting qubit quantum computer. *Science*, 369:1084–1089, 2020.

[14] PW Shor. Polynomial-time algorithms for prime factorization and discrete logarithms on a quantum computer. *SIAM J. Comput.*, 26(5):1484–1509, Jan 1997.

[15] Fabrice Boudot, Pierrick Gaudry, Aurore Guillevic, Nadia Heninger, Emmanuel Thomé, and Paul Zimmermann. Comparing the difficulty of factorization and discrete logarithm: A 240-digit experiment. In Daniele Micciancio and Thomas Ristenpart, editors, *Advances in Cryptology – CRYPTO 2020*, pages 62–91, Cham, 2020. Springer International Publishing.

[16] LK Grover. Quantum mechanics helps in searching for a needle in a haystack. *Phys. Rev. Lett.*, 79(2):325–328, Jan 1997.

[17] D. P. DiVincenzo. The physical implementation of quantum computation. *Fortschr. Phys.*, 48(9-11):771–783, Jan 2000.

[18] P.W. Shor. Fault-tolerant quantum computation. *Proceedings of 37th Conference on Foundations of Computer Science*, 1996.

[19] Raymond Laflamme, Cesar Miquel, Juan Pablo Paz, and Wojciech Hubert Zurek. Perfect quantum error correcting code. *Physical Review Letters*, 77(1):198, 1996.

[20] Austin G. Fowler, Matteo Mariantoni, John M. Martinis, and Andrew N. Cleland. Surface codes: Towards practical large-scale quantum computation. *Phys. Rev. A*, 86:032324, Sep 2012.

[21] David S. Wang, Austin G. Fowler, and Lloyd C. L. Hollenberg. Surface code quantum computing with error rates over 1%. *Phys. Rev. A*, 83:020302, Feb. 2011.

[22] Emanuel Knill, Raymond Laflamme, and Wojciech H. Zurek. Resilient quantum computation. *Science*, 279:342–345, 1998.

[23] Hai-Rui Wei and Gui Lu Long. Hybrid quantum gates between flying photon and diamond nitrogen-vacancy centers assisted by optical microcavities. *Scientific Reports*, 5:12918, Feb 2015.

[24] Raju Valivarthi, Samantha I. Davis, Cristián Peña, Si Xie, Nikolai Lauk, Lautaro Narváez, Jason P. Allmaras, Andrew D. Beyer, Yewon Gim, Meraj Hussein, George Iskander, Hyunseong Linus Kim, Boris Korzh, Andrew Mueller, Mandy Rominsky, Matthew Shaw, Dawn Tang, Emma E. Wollman, Christoph Simon, Panagiotis Spentzouris, Daniel Oblak, Neil Sinclair, and Maria Spiropulu. Teleportation systems toward a quantum internet. *PRX Quantum*, 1:020317, Dec 2020.

[25] Yuri Alexeev, Dave Bacon, Kenneth R. Brown, Robert Calderbank, Lincoln D. Carr, Frederic T. Chong, Brian DeMarco, Dirk Englund, Edward Farhi, Bill Fefferman, Alexey V. Gorshkov, Andrew Houck, Jungsang Kim, Shelby Kimmel, Michael Lange, Seth Lloyd, Mikhail D. Lukin, Dmitri Maslov, Peter Maunz, Christopher Monroe, John Preskill, Martin Roetteler, Martin J. Savage, and Jeff Thompson. Quantum computer systems for scientific discovery. *PRX Quantum*, 2:017001, Feb 2021.

[26] D. Loss and D. P. DiVincenzo. Quantum computation with quantum dots. *Phys. Rev. A*, 57(1):120–126, 1998.

[27] F. H. L. Koppens, C. Buizert, K. J. Tielrooij, I. T. Vink, K. C. Nowack, T. Meunier, L. P. Kouwenhoven, and L. M. K. Vandersypen. Driven coherent oscillations of a single electron spin in a quantum dot. *Nature*, 442:766–771, 2006.

[28] L. Gaudreau, G. Granger, A. Kam, G C. Aers, S. A. Studenikin, P. Zawadzki, M. Pioro-Ladrière, Z. R. Wasilewski, and A. S. Sachrajda. Coherent control of three-spin states in a triple quantum dot. *Nat. Phys.*, 8:54–58, 2012.

[29] B. M. Maune, M. G. Borselli, B. Huang, T. D. Ladd, P. W. Deelman, K. S. Holabird, A. A. Kiselev, I. Alvarado-Rodriguez, R. S. Ross, A. E. Schmitz, M. Sokolich, C. A. Watson, M. F. Gyure, and A. T. Hunter. Coherent singlet-triplet oscillations in a silicon-based double quantum dot. *Nature*, 481(7381):344–347, 2012.

[30] Jarryd J. Pla, Kuan Y. Tan, Juan P. Dehollain, Wee H. Lim, John J. L. Morton, David N. Jamieson, Andrew S. Dzurak, and Andrea Morello. A single-atom electron spin qubit in silicon. *Nature*, 489:541–545, 2012.

[31] J. Medford, J. Beil, J. M. Taylor, E. I. Rashba, H. Lu, A. C. Gossard, and C. M. Marcus. Quantum-dot-based resonant exchange qubit. *Phys. Rev. Lett.*, 111:050501, Jul 2013.

[32] M. Veldhorst, J. C. C. Hwang, C. H. Yang, A. W. Leenstra, B. de Ronde, J. P. Dehollain, J. T. Muhonen, F. E. Hudson, K. M. Itoh, A. Morello, and A. S. Dzurak. An addressable quantum dot qubit with fault-tolerant control-fidelity. *Nat. Nanotechnol.*, 9(12):981–985, 2014.

[33] Dohun Kim, Zhan Shi, C. B. Simmons, D. R. Ward, J. R. Prance, Teck Seng Koh, John King Gamble, D. E. Savage, M. G. Lagally, Mark Friesen, S. N. Coppersmith, and M. A. Eriksson. Quantum control and process tomography of a semiconductor quantum dot hybrid qubit. *Nature*, 511:70–74, 2014.

[34] J. R. Petta, A. C. Johnson, J. M. Taylor, E. A. Laird, A. Yacoby, M. D. Lukin, C. M. Marcus, M. P. Hanson, and A. C. Gossard. Coherent manipulation of coupled electron spins in semiconductor quantum dots. *Science*, 309:2180–2184, 2005.

[35] K. C. Nowack, M. Shafiei, M. Laforest, G. E. D. K. Prawiroatmodjo, L. R. Schreiber, C. Reichl, W. Wegscheider, and L. M. K. Vandersypen. Single-shot correlations and two-qubit gate of solid-state spins. *Science*, 333(6047):1269–1272, 2011.

[36] M. Veldhorst, C. H. Yang, J. C. C. Hwang, W. Huang, J. P. Dehollain, J. T. Muhonen, S. Simmons, A. Laucht, F. E. Hudson, K. M. Itoh, A. Morello, and A. S. Dzurak. A two-qubit logic gate in silicon. *Nature*, 526:410, 2015.

[37] T. F. Watson, S. G. J. Philips, E. Kawakami, D. R. Ward, P. Scarlino, M. Veldhorst, D. E. Savage, M. G. Lagally, Mark Friesen, S. N. Coppersmith, M. A. Eriksson, and L. M. K. Vandersypen. A programmable two-qubit quantum processor in silicon. *Nature*, 555:633, 2018.

[38] D. M. Zajac, A. J. Sigillito, M. Russ, F. Borjans, J. M. Taylor, G. Burkard, and J. R. Petta. Resonantly driven CNOT gate for electron spins. *Science*, 359:439, 2018.

[39] Nico W. Hendrickx, William I. L. Lawrie, Maximillian Russ, Floor van Riggelen, Sander L. de Snoo, Raymond N. Schouten, Amir Sammak, Giordano Scappucci, and Menno Veldhorst. A four-qubit germanium quantum processor. *Nature*, 591:580, 2021.

[40] Xiao Xue, Maximilian Russ, Nodar Samkharadze, Brennan Undseth, Amir Sammak, Giordano Scappucci, and Lieven M. K. Vandersypen. Computing with spin qubits at the surface code error threshold. 2021. arXiv:2107.00628.

[41] L J Klein, D E Savage, and M A Eriksson. Coulomb blockade and kondo effect in a few-electron silicon/silicon-germanium quantum dot. *Appl. Phys. Lett.*, 90:033103, Jan 2007.

[42] K. A. Slinker, K. L. M. Lewis, C. C. Haselby, S. Goswami, L. J. Klein, J. O. Chu, S. N. Coppersmith, R. Joynt, R. H. Blick, M. Friesen, and M. A. Eriksson. Quantum dots in Si/SiGe 2DEGs with Schottky top-gated leads. *New J. Phys.*, 7:246, Jan 2005.

[43] Susan J Angus, Andrew J Ferguson, Andrew S Dzurak, and Robert G Clark. Gate-defined quantum dots in intrinsic silicon. *Nano Lett.*, 7:2051–2055, Jan 2007.

[44] D. M. Zajac, T. M. Hazard, X. Mi, K. Wang, and J. R. Petta. A reconfigurable gate architecture for Si/SiGe quantum dots. *Appl. Phys. Lett.*, 106:223507, 2015.

[45] L. DiCarlo, H. J. Lynch, A. C. Johnson, L. I. Childress, K. Crockett, C. M. Marcus, M. P. Hanson, and A. C. Gossard. Differential charge sensing and charge delocalization in a tunable double quantum dot. *Phys. Rev. Lett.*, 92(22):226801, 2004.

[46] C B Simmons, M Thalakulam, N Shaji, L J Klein, H Qin, R H Blick, D E Savage, M G Lagally, S N Coppersmith, and M A Eriksson. Single-electron quantum dot in Si/SiGe with integrated charge sensing. *Appl. Phys. Lett.*, 91:213103, 2007.

[47] C. Barthel, M. Kjaergaard, J. Medford, M. Stopa, C. M. Marcus, M. P. Hanson, and A. C. Gossard. Fast sensing of double-dot charge arrangement and spin state with a radio-frequency sensor quantum dot. *Physical Review B*, 81(16):161308(R), apr 2010.

[48] D. J Reilly, C. M Marcus, M. P Hanson, and A. C Gossard. Fast single-charge sensing with a rf quantum point contact. *Appl Phys Lett*, 91:162101, 2007.

[49] E. A Laird, J. M Taylor, D. P DiVincenzo, C. M Marcus, M. P Hanson, and A. C Gossard. Coherent spin manipulation in an exchange-only qubit. *Phys. Rev. B*, 82(7):075403, 2010.

[50] K. D Petersson, C. G Smith, D Anderson, P Atkinson, G. A. C Jones, and D. A Ritchie. Charge and spin state readout of a double quantum dot coupled to a resonator. *Nano Lett*, 10(8):2789–2793, Aug 2010.

[51] L. P. Kouwenhoven, C. M. Marcus, P. L. McEuen, S. Tarucha, R. M. Westervelt, and N. S. Wingreen. *Mesoscopic Electron Transport*, volume 345, chapter Electron Transport in Quantum Dots, page 105. Kluwer, 1997.

[52] R. Hanson, L. P. Kouwenhoven, J. R. Petta, S. Tarucha, and L. M. K. Vandersypen. Spins in few-electron quantum dots. *Rev. Mod. Phys.*, 79:1217–1265, 2007.

[53] F. A. Zwanenburg, A. S. Dzurak, A. Morello, M. Y. Simmons, L. C. L. Hollenberg, G. Klimeck, S. Rogge, S. N. Coppersmith, and M. A. Eriksson. Silicon quantum electronics. *Rev. Mod. Phys.*, 85:961, 2013.

[54] K. D. Petersson, J. R. Petta, H. Lu, and A. C. Gossard. Quantum coherence in a one-electron semiconductor charge qubit. *Phys. Rev. Lett.*, 105:246804, 2010.

[55] Gang Cao, Hai-Ou Li, Tao Tu, Li Wang, Cheng Zhou, Ming Xiao, Guang-Can Guo, Hong-Wen Jiang, and Guo-Ping Guo. Ultrafast universal quantum control of a quantum-dot charge qubit using Landau–Zener–Stückelberg interference. *Nat. Commun.*, 4:1401, 2013.

[56] Dohun Kim, D. R. Ward, C. B. Simmons, John King Gamble, Robin Blume-Kohout, Erik Nielsen, D. E. Savage, M. G. Lagally, Mark Friesen, S. N. Coppersmith, and M. A. Eriksson. Microwave-driven coherent operations of a semiconductor quantum dot charge qubit. *Nat. Nanotechnol.*, 10:243–247, 2015.

[57] Giordano Scappucci, Christoph Kloeffel, Floris A. Zwanenburg, Daniel Loss, Maksym Myronov, Jian-Jun Zhang, Silvano De Franceschi, Georgios Katsaros, and Menno Veldhorst. The germanium quantum information route. *Nature Review Materials*, 2020.

[58] M. Pioro-Ladrière, T. Obata, Y. Tokura, Y.-S. Shin, T. Kubo, K. Yoshida, T. Taniyama, and S. Tarucha. Electrically driven single-electron spin resonance in a slanting Zeeman field. *Nat. Phys.*, 4(10):776–779, 2008.

[59] Jun Yoneda, Tomohiro Otsuka, Tatsuki Takakura, Michel Pioro-Ladrière, Roland Brunner, Hong Lu, Takashi Nakajima, Toshiaki Obata, Akito Noiri, Christopher J. Palmstrøm, Arthur C. Gossard, and Seigo Tarucha. Robust micromagnet design for fast electrical manipulations of single spins in quantum dots. *Appl. Phys. Express*, 8:084401, 2015.

[60] Jun Yoneda, Kenta Takeda, Tomohiro Otsuka, Takashi Nakajima, Matthieu R. Delbecq, Giles Allison, Takumu Honda, Tetsuo Kodera, Shunri Oda, Yusuke Hoshi, Noritaka Usami, Kohei M. Itoh, and Seigo Tarucha. A quantum-dot spin qubit with coherence limited by charge noise and fidelity higher than 99.9%. *Nature Nanotechnol.*, 13:102, 2018.

[61] C. H. Yang, K. W. Chan, R. Harper, W. Huang, T. Evans, J. C.C. Hwang, B. Hensen, A. Laucht, T. Tanttu, F. E. Hudson, S. T. Flammia, K. M. Itoh, A. Morello, S. D. Bartlett, and A. S. Dzurak. Silicon qubit fidelities approaching incoherent noise limits via pulse engineering. *Nat Electron*, 2:151–158, 2019.

[62] Peter Stano and Daniel Loss. Review of performance metrics of spin qubits in gated semiconducting nanostructures. 2021. preprint arXiv:2107.06485v1.

[63] Zhan Shi, C. B. Simmons, J. R. Prance, John King Gamble, Teck Seng Koh, Yun-Pil Shim, Xuedong Hu, D. E. Savage, M. G. Lagally, M. A. Eriksson, Mark Friesen, and S. N. Coppersmith. Fast hybrid silicon double-quantum-dot qubit. *Phys. Rev. Lett.*, 108:140503, 2012.

[64] Z. Shi, C. B. Simmons, J.R. Prance, John King Gamble, Mark Friesen, D. E. Savage, M. G. Lagally, S. N. Coppersmith, and M. A. Eriksson. Tunable singlet-triplet splitting in a few-electron Si/SiGe quantum dot. *Appl. Phys. Lett.*, 99:233108, 2011.

[65] Zhan Shi, C. B. Simmons, Daniel R. Ward, J. R. Prance, Xian Wu, Teck Seng Koh, John King Gamble, D. E. Savage, M. G. Lagally, Mark Friesen, S. N. Coppersmith, and M. A. Eriksson. Fast coherent manipulation of three-electron states in a double quantum dot. *Nat. Commun.*, 5:3020, 2014.

[66] Joshua S. Schoenfield, Blake M. Freeman, and HongWen Jiang. Coherent manipulation of valley states at multiple charge configurations of a silicon quantum dot device. *Nature Commun.*, 8(1):64, 2017.

[67] X. Mi, S. Kohler, and J. R. Petta. High-resolution valley spectroscopy of Si quantum dots. *Phys. Rev. Lett.*, 98:176803, Oct 2018.

[68] Samuel F. Neyens, Ryan H. Foote, Brandur Thorgrimsson, T. J. Knapp, Thomas McJunkin, L. M. K. Vandersypen, Payam Amin, Nicole K. Thomas, James S. Clarke, D. E. Savage, M. G. Lagally, Mark Friesen, S. N. Coppersmith, and M. A. Eriksson. The critical role of substrate disorder in valley splitting in Si quantum wells. *Appl. Phys. Lett.*, 112:243107, 2018.

[69] Edward H. Chen, Kate Raach, Andrew Pan, Andrey A. Kiselev, Edwin Acuna, Jacob Z. Blumoff, Teresa Brecht, Maxwell Choi, Wonill Ha, Daniel Hulbert, Michael P. Jura, Tyler Keating, Ramsey Noah, Bo Sun, Bryan J. Thomas, Matthew Borselli, C.A.C. Jackson, Matthew T. Rakher, and Richard S. Ross. Detuning axis pulsed spectroscopy of valley-orbital states in Si/Si-Ge quantum dots. *Phys. Rev. Appl.*, 15:044033, 2021.

[70] J. P. Dodson, H. Ekmel Ercan, J. Corrigan, Merritt Losert, Nathan Holman, Thomas McJunkin, L. F. Edge, Mark Friesen, S. N. Coppersmith, and M. A. Eriksson. How valley-orbit states in silicon quantum dots probe quantum well interfaces, 2021. preprint arXiv:2103.14702.

[71] W. H Lim, C. H. Yang, F. A Zwanenburg, and A. S Dzurak. Spin filling of valley-orbit states in a silicon quantum dot. *Nanotechnology*, 22(33):335704, 2011.

[72] C. H. Yang, A. Rossi, R. Ruskov, N. S. Lai, F. A. Mohiyaddin, S. Lee, C. Tahan, Gerhard Klimeck, A. Morello, and A. S. Dzurak. Spin-valley lifetimes in a silicon quantum dot with tunable valley splitting. *Nature Communications*, 4:2069, 2013.

[73] John King Gamble, M. A. Eriksson, S. N. Coppersmith, and Mark Friesen. Disorder-induced valley-orbit hybrid states in Si quantum dots. *Phys. Rev. B*, 88:035310, 2013.

[74] D. M. Zajac, T. M. Hazard, X. Mi, E. Nielsen, and J. R. Petta. Scalable gate architecture for a one-dimensional array of semiconductor spin qubits. *Phys. Rev. Appl.*, 6:054013, 2016.

[75] Gang Cao, Hai-Ou Li, Guo-Dong Yu, Bao-Chuan Wang, Bao-Bao Chen, Xiang-Xiang Song, Ming Xiao, Guang-Can Guo, Hong-Wen Jiang, Xuedong Hu, and Guo-Ping Guo. Tunable hybrid qubit in a GaAs double quantum dot. *Phys. Rev. Lett.*, 116(8):086801, 2016.

[76] Wonjin Jang, Min-Kyun Cho, Hyeongyu Jang, Jehyun Kim, Jaemin Park, Gyeonghun Kim, Byoungwoo Kang, Hwanchul Jung, Vladimir Umansky, and Dohun Kim. Single-shot readout of a driven hybrid qubit in a GaAs double quantum dot. *Nano Letters*, 21(12):4999–5005, June 2021.

[77] Dohun Kim, D. R. Ward, C. B. Simmons, D. E. Savage, M. G. Lagally, Mark Friesen, S. N. Coppersmith, and M. A. Eriksson. High-fidelity resonant gating of a silicon-based quantum dot hybrid qubit. *npj Quantum Inf.*, 1:15004, 2015.

[78] Brandur Thorgrimsson, Dohun Kim, Yuan-Chi Yang, L. W. Smith, C. B. Simmons, D. R. Ward, R. H. Foote, J. Corrigan, D. E. Savage, M. G. Lagally, Mark Friesen, S. N. Coppersmith, and M. A. Eriksson. Extending the coherence of a quantum dot hybrid qubit. *npj Quantum Inf.*, 3:32, 2017.

[79] J. P. Dodson*, J. Corrigan*, Brandur Thorgrimsson, Samuel F. Neyens, T. J. Knapp, Thomas McJunkin, S. N. Coppersmith, and M. A. Eriksson. Manuscript in preparation.

[80] D. P. DiVincenzo, D. Bacon, J. Kempe, G. Burkard, and K. B. Whaley. Universal quantum computation with the exchange interaction. *Nature*, 408(6810):339, Nov 2000.

[81] J. Levy. Universal quantum computation with spin-1/2 pairs and Heisenberg exchange. *Phys. Rev. Lett.*, 89(14):147902, Jan 2002.

[82] K. Wang, C. Payette, Y. Dovzhenko, P. W. Deelman, and J. R. Petta. Charge relaxation in a single-electron Si/SiGe double quantum dot. *Phys. Rev. Lett.*, 111:046801, 2013.

[83] J. P. Dodson, Nathan Holman, Brandur Thorgrimsson, Samuel F. Neyens, E. R. MacQuarrie, Thomas McJunkin, Ryan H. Foote, L. F. Edge, S. N. Coppersmith, and M. A. Eriksson. Fabrication process and failure analysis for robust quantum dots in silicon. *Nanotechnology*, 31(50):505001, 2020.

[84] M. G. Borselli, R. S. Ross, A. A. Kiselev, E. T. Croke, K. S. Holabird, P. W. Deelman, L. D. Warren, I. Alvarado-Rodriguez, I. Milosavljevic, F. C. Ku, W. S. Wong, A. E. Schmitz, M. Sokolich, M. F. Gyure, and A. T. Hunter. Measurement of valley splitting in high-symmetry Si/SiGe quantum dots. *Appl. Phys. Lett.*, 98(12):123118, Jan 2011.

[85] C. H. Yang, W. H. Lim, N. S. Lai, A. Rossi, A. Morello, and A. S. Dzurak. Orbital and valley state spectra of a few-electron silicon quantum dot. *Phys. Rev. B*, 86:115319, 2012.

[86] Thomas Mcjunkin, E. R. Macquarrie, Leah Tom, S. F. Neyens, J. P. Dodson, Brandur Thorgrimsson, J. Corrigan, H. Ekmel Ercan, D. E. Savage, M. G. Lagally, Robert Joynt, S. N. Coppersmith, Mark Friesen, and M. A. Eriksson. Valley splittings in Si / SiGe quantum dots with a germanium spike in the silicon well. *Physical Review B*, 104:085406, 2021.

[87] P. Scarlino, D. J. van Woerkom, A. Stockklauser, J. V. Koski, M. C. Collodo, S. Gasparinetti, C. Reichl, W. Wegscheider, T. Ihn, K. Ensslin, and A. Wallraff. All-microwave control and dispersive readout of gate-defined quantum dot qubits in circuit quantum electrodynamics. *Phys. Rev. Lett.*, 122:206802, 2019.

[88] E. R. MacQuarrie, Samuel F. Neyens, J. P. Dodson, J. Corrigan, Brandur Thorgrimsson, Nathan Holman, L. F. Edge, Mark Friesen, S. N. Coppersmith, and M. A. Eriksson. Progress toward a capacitively mediated CNOT between two charge qubits in Si/SiGe. *npj Quantum Inf.*, 6:81, 2020.

[89] S. A. Studenikin, J. Thorgrimson, G. C. Aers, A. Kam, P. Zawadzki, Z. R. Wasilewski, A. Bogan, and A. S. Sachrajda. Enhanced charge detection of spin qubit readout via an intermediate state. *Appl. Phys. Lett.*, 101:233101, 2012.

[90] K. MacLean, S. Amasha, Iuliana P. Radu, D. M. Zumbühl, M. A. Kastner, M. P. Hanson, and A. C. Gossard. Energy-dependent tunneling in a quantum dot. *Phys. Rev. Lett.*, 98(3):036802, Jan 2007.

[91] Y. Nazarov and Y. Blanter. *Quantum Transport: Introduction to Nanoscience*. Cambridge University Press, 1st edition, 2009.

[92] J. M. Elzerman, R. Hanson, L. H. Willems van Beveren, L. M. K. Vandersypen, and L. P. Kouwenhoven. Excited-state spectroscopy on a nearly closed quantum dot via charge detection. *Appl. Phys. Lett.*, 84:4617–4619, 2004.

[93] J. Corrigan, J. P. Dodson, H. Ekmel Ercan, J. C. Abadillo-Uriel, Brandur Thorgrimsson, T. J. Knapp, Nathan Holman, Thomas McJunkin, Samuel F. Neyens, E. R. MacQuarrie, Ryan H. Foote, L. F. Edge, Mark Friesen, S. N. Coppersmith, and M. A. Eriksson. Accepted at Phys. Rev. Lett., available at https://arxiv.org/abs/2009.13572.

[94] Adam Frees, Sebastian Mehl, John King Gamble, Mark Friesen, and S. N. Coppersmith. Adiabatic two-qubit gates in capacitively coupled quantum dot hybrid qubits. *npj Quantum Inf.*, 5:73, 2019.

[95] Samuel F. Neyens, E. R. MacQuarrie, J. P. Dodson, J. Corrigan, Nathan Holman, Brandur Thorgrimsson, M. Palma, Thomas McJunkin, L. F. Edge, Mark Friesen, S. N. Coppersmith, and M. A. Eriksson. Measurements of capacitive coupling within a quadruple-quantum-dot array. *Phys. Rev. Applied*, 12:064049, 2019.

[96] K. D. Petersson, C. G. Smith, D. Anderson, P. Atkinson, G. A. C. Jones, and D. A. Ritchie. Microwave-driven transitions in two coupled semiconductor charge qubits. *Phys. Rev. Lett.*, 103:016805, 2009.

[97] Daniel R. Ward, Dohun Kim, Donald E. Savage, Max G. Lagally, Ryan H. Foote, Mark Friesen, Susan N. Coppersmith, and Mark A. Eriksson. State-conditional coherent charge qubit oscillations in a Si/SiGe quadruple quantum dot. *npj Quantum Inf.*, 2:16032, 2016.

[98] X. Mi, J. V. Cady, D. M. Zajac, P. W. Deelman, and J. R. Petta. Strong coupling of a single electron in silicon to a microwave photon. *Science*, 355:156–158, 2017.

[99] X. Croot, X. Mi, S. Putz, M. Benito, F. Borjans, G. Burkard, and J. R. Petta. Flopping-mode electric dipole spin resonance. *Phys. Rev. Research*, 2:012006, Jan 2020.

[100] B. Kratochwil, J. V. Koski, A. J. Landig, P. Scarlino, J. C. Abadillo-Uriel, C. Reichl, S. N. Coppersmith, W. Wegscheider, Mark Friesen, A. Wallraff, T. Ihn, and K. Ensslin. Charge qubit in a triple quantum dot with tunable coherence. *Phys. Rev. Research*, 3:013171, Feb 2021.

[101] J. C. Abadillo-Uriel, Cameron King, S. N. Coppersmith, and Mark Friesen. Long-range two-hybrid-qubit gates mediated by a microwave cavity with red sidebands. 2021. preprint arXiv:2106.10555.

[102] C. H. Yang, R. C.C. Leon, J. C.C. Hwang, A. Saraiva, T. Tanttu, W. Huang, J. Camirand Lemyre, K. W. Chan, K. Y. Tan, F. E. Hudson, K. M. Itoh, A. Morello, M. Pioro-Ladrière, A. Laucht, and A. S. Dzurak. Operation of a silicon quantum processor unit cell above one kelvin. *Nature*, 580:350–354, 2020.

[103] R. C.C. Leon, C. H. Yang, J. C.C. Hwang, J. Camirand Lemyre, T. Tanttu, W. Huang, K. W. Chan, K. Y. Tan, F. E. Hudson, K. M. Itoh, A. Morello, A. Laucht, M. Pioro-Ladrière, A. Saraiva, and A. S. Dzurak. Coherent spin control of s-, p-, d- and f-electrons in a silicon quantum dot. *Nat. Commun.*, 11(1):797, 2020.

[104] K. Ono, D. G. Austing, Y. Tokura, and S. Tarucha. Current rectification by Pauli exclusion in a weakly coupled double quantum dot system. *Science*, 297:1313, 2002.

[105] M. D. Shulman, O. E. Dial, S. P. Harvey, H. Bluhm, V. Umansky, and A. Yacoby. Demonstration of entanglement of electrostatically coupled singlet-triplet qubits. *Science*, 336:202–205, 2012.

[106] M. D. Reed, B. M. Maune, R. W. Andrews, M. G. Borselli, K. Eng, M. P. Jura, A. A. Kiselev, T. D. Ladd, S. T. Merkel, I. Milosavljevic, E. J. Pritchett, M. T. Rakher, R. S. Ross, A. E. Schmitz, A. Smith, J. A. Wright, M. F. Gyure, and A. T. Hunter. Reduced sensitivity to charge noise in semiconductor spin qubits via symmetric operation. *Phys. Rev. Lett.*, 116(11):110402, 2016.

[107] Ruoyu Li, Luca Petit, David P. Franke, Juan Pablo Dehollain, Jonas Helsen, Mark Steudtner, Nicole K. Thomas, Zachary R. Yoscovits, Kanwal J. Singh, Stephanie Wehner, Lieven M. K. Vandersypen, James S. Clarke, and Menno Veldhorst. A crossbar network for silicon quantum dot qubits. *Science Advances*, 4(7), 2018.

[108] L. M. K Vandersypen, H. Bluhm, J. S. Clarke, A. S. Dzurak, R. Ishihara, A. Morello, D. J. Reilly, L. R. Schreiber, and M. Veldhorst. Interfacing spin qubits in quantum dots and donors? Hot, dense, and coherent. *npj Quantum Inf.*, 3:34, 2017.

[109] L. Petit, H. G. J. Eenink, M. Russ, W. I L. Lawrie, N. W. Hendrickx, S. G. J Philips, J. S. Clarke, L. M K. Vandersypen, and M. Veldhorst. Universal quantum logic in hot silicon qubits. *Nature*, 580:355–359, 2020.

[110] Garnett W. Bryant. Electronic structure of ultrasmall quantum-well boxes. *Phys. Rev. Lett.*, 59(10):1140, Sept 1987.

[111] Constantine Yannouleas and Uzi Landman. Spontaneous symmetry breaking in single and molecular quantum dots. *Phys. Rev. Lett.*, 82(26):5325, June 1999.

[112] Jerzy Cioslowski and Katarzyna Pernal. The ground state of harmonium. *J. Chem. Phys.*, 113:8434.

[113] S. M. Reimann, M. Koskinen, and M. Manninen. Formation of Wigner molecules in small quantum dots. *Phys. Rev. B*, 62:8108, 2000.

[114] A. V. Filinov, M. Bonitz, and Yu. E. Lozovik. Wigner crystallization in mesoscopic 2d electron systems. *Phys. Rev. Lett.*, 86:3851–3854, 2001.

[115] Boris Reusch, Wolfgang Häusler, and Hermann Grabert. Wigner molecules in quantum dots. *Phys. Rev. B*, 63:113313, 2001.

[116] B. Szafran, F. M. Peeters, S. Bednarek, T. Chwiej, and J. Adamowski. Spatial ordering of charge and spin in quasi-one-dimensional Wigner molecules. *Phys. Rev. B*, 70:035401, 2004.

[117] Massimo Rontani, Carlo Cavazzoni, Devis Bellucci, and Guido Goldoni. Full configuration interaction approach to the few-electron problem in artificial atoms. *The Journal of Chemical Physics*, 124(12):124102, 2006.

[118] Amit Ghosal, A. D. Güçlü, C. J. Umrigar, Denis Ullmo, and Harold U. Baranger. Incipient Wigner localization in circular quantum dots. *Phys. Rev. B*, 76:085341, Aug 2007.

[119] F Cavaliere, U De Giovannini, M Sassetti, and B Kramer. Transport properties of quantum dots in the Wigner molecule regime. *New Journal of Physics*, 11(12):123004, dec 2009.

[120] I. Shapir, A. Hamo, S. Pecker, C. P. Moca, Ö. Legeza, G. Zarand, and S. Ilani. Imaging the electronic Wigner crystal in one dimension. *Science*, 364:870–875, 2019.

[121] A. M. Mintairov, J. Kapaldo, J. L. Merz, S. Rouvimov, D. V. Lebedev, N. A. Kalyuzhnyy, S. A. Mintairov, K. G. Belyaev, M. V. Rakhlin, A. A. Toropov, P. N. Brunkov, A. S. Vlasov, Yu.M. Zadiranov, S. A. Blundell, A. M. Mozharov, I. Mukhin, M. Yakimov, S. Oktyabrsky, A. V. Shelaev, and V. A. Bykov. Control of Wigner localization

and electron cavity effects in near-field emission spectra of In(Ga)P/GaInP quantum-dot structures a. *Phys. Rev. B*, 97(19):195443, May 2018.

[122] Sokratis Kalliakos, Massimo Rontani, Vittorio Pellegrini, César Pascual García, Aron Pinczuk, Guido Goldoni, Elisa Molinari ad Loren N. Pfeiffer, and Ken W. West. A molecular state of correlated electrons in a quantum dot. *Nat. Phys.*, 4:467–471, Apr 2008.

[123] Achintya Singha, Vittorio Pellegrini, Aron Pinczuk, Loren N. Pfeiffer, Ken W. West, and Massimo Rontani. Correlated electrons in optically tunable quantum dots: Building an electron dimer molecule. *Phys. Rev. Lett.*, 104(24):246802, June 2010.

[124] C. Ellenberger, T. Ihn, C. Yannouleas, U. Landman, K. Ensslin, D. Driscoll, and A. C. Gossard. Excitation spectrum of two correlated electrons in a lateral quantum dot with negligible zeeman splitting. *Phys. Rev. Lett.*, 96:126806, 2006.

[125] L. H. Kristinsdóttir, J. C. Cremon, H. A. Nilsson, H. Q. Xu, L. Samuelson, H. Linke, A. Wacker, and S. M. Reimann. Signatures of Wigner localization in epitaxially grown nanowires. *Phys. Rev. B*, 83:041101, Jan 2011.

[126] S. Pecker, F. Kuemmeth, A. Secchi, M. Rontani, D. C. Ralph, P. L. McEuen, and S. Ilani. Observation and spectroscopy of a two-electron Wigner molecule in an ultraclean carbon nanotube. *Nat. Phys.*, 9:576–581, July 2013.

[127] L. A. Tracy, D. R. Luhman, S. M. Carr, N. C. Bishop, G. A. Ten Eyck, T. Pluym, J. R. Wendt, M. P. Lilly, and M. S. Carroll. Single shot spin readout using a cryogenic high-electron-mobility transistor amplifier at sub-Kelvin temperatures. *Appl. Phys. Lett.*, 108:063101, 2016.

[128] U. Merkt, J. Huser, and M. Wagner. Energy spectra of two electrons in a harmonic quantum dot. *Phys. Rev. B*, 43:7320–7323, Mar 1991.

[129] S. A. Blundell and S. Chacko. Excited states of incipient Wigner molecules. *Phys. Rev. B*, 83:195444, May 2011.

[130] L. Wang, K. Shen, B. Y. Sun, and M. W. Wu. Singlet-triplet relaxation in multivalley silicon single quantum dots. *Phys. Rev. B*, 81:235326, 2010.

[131] E Wach, D P Zebrowski, and B Szafran. Charge density mapping of strongly-correlated few-electron two-dimensional quantum dots by the scanning probe technique. *J Phys-Condens Mat*, 25:335801, 2013.

[132] F Cavaliere, N Traverso Ziani, F Negro, and M Sassetti. Thermally enhanced Wigner oscillations in two-electron 1d quantum dots. *J Phys-Condens Mat*, 26:505301, 2014.

[133] H. Ekmel Ercan, S. N. Coppersmith, and Mark Friesen. Strong electron-electron interactions in Si/SiGe quantum dots. 2021. preprint arXiv:2105.10645.

[134] Arne Hollmann, Tom Struck, Veit Langrock, Andreas Schmidbauer, Floyd Schauer, Tim Leonhardt, Kentarou Sawano, Helge Riemann, Nikolay V. Abrosimov, Dominique Bougeard, and Lars R. Schreiber. Large, tunable valley splitting and single-spin relaxation mechanisms in a Si/SiGe quantum dot. *Phys. Rev. Applied*, 13:034068, 2020.

[135] T. B. Boykin, G. Klimeck, M. A. Eriksson, M. Friesen, S. N. Coppersmith, P. von Allmen, F. Oyafuso, and S. Lee. Valley splitting in strained silicon quantum wells. *Appl. Phys. Lett.*, 84:115–117, 2004.

[136] T. B. Boykin, G. Klimeck, M. Friesen, S. N. Coppersmith, P. vonAllmen, F. Oyafuso, and S. Lee. Valley splitting in low-density quantum-confined heterostructures studied using tight-binding models. *Phys. Rev. B*, 70:165325, Jan 2004.

[137] R. A. Faulkner. *Phys Rev*, 184(3):713–721, Aug 1969.

[138] J. I. Colless, A. C. Mahoney, J. M. Hornibrook, A. C. Doherty, H. Lu, A. C. Gossard, and D. J. Reilly. Dispersive readout of a few-electron double quantum dot with fast rf gate sensors. *Phys. Rev. Lett.*, 110:046805, 2013.

[139] A. Rossi, R. Zhao, A. S. Dzurak, and M. F. Gonzalez-Zalba. Dispersive readout of a silicon quantum dot with an accumulation-mode gate sensor. *Appl. Phys. Lett.*, 110:212101, 2017.

[140] Christian Volk, Anasua Chatterjee, Fabio Ansaloni, Charles M. Marcus, and Ferdinand Kuemmeth. Fast charge sensing of Si/SiGe quantum dots via a high-frequency accumulation gate. *Nano Lett.*, 19:5628–5633, 2019.

[141] T. Frey, P. J. Leek, M. Beck, A. Blais, T. Ihn, K. Ensslin, and A. Wallraff. Dipole coupling of a double quantum dot to a microwave resonator. *Phys. Rev. Lett.*, 108:046807, 2012.

[142] K. D. Petersson, L. W. McFaul, M. D. Schroer, M. Jung, J. M. Taylor, A. A. Houck, and J. R. Petta. Circuit quantum electrodynamics with a spin qubit. *Nature*, 490:380–383, 2012.

[143] Guoji Zheng, Nodar Samkharadze, Marc L. Noordam, Nima Kalhor, Delphine Brousse, Amir Sammak, Giordano Scappucci, and Lieven M. K. Vandersypen. Rapid gate-based spin readout in silicon using an on-chip resonator. *Nature Nanotechnology*, 14:742–746, 2019.

[144] L. E. Bruhat, J. J. Viennot, M. C. Dartiailh, M. M. Desjardins, T. Kontos, and A. Cottet. Cavity photons as a probe for charge relaxation resistance and photon emission in a quantum dot coupled to normal and superconducting continua. *Physical Review X*, 6:021014.

[145] X. Mi, J. V. Cady, D. M. Zajac, J. Stehlik, L. F. Edge, and J. R. Petta. *Appl Phys Lett*, 110(110):043502, Jan 2017.

[146] F. Borjans, X. Mi, and J. R. Petta. Spin digitizer for high-fidelity readout of a cavity-coupled silicon triple quantum dot. *Phys. Rev. Appl.*, 15:044052, 2021.

[147] F. Borjans, X. G. Croot, X. Mi, M. J. Gullans, and J. R. Petta. Resonant microwave-mediated interactions between distant electron spins. *Nature*, 577:195–199, 2020.

[148] Patrick Harvey-Collard, Jurgen Dijkema, Guoji Zheng, Amir Sammak, Giordano Scappucci, and Lieven M. K. Vandersypen. Circuit quantum electrodynamics with two remote electron spins. 2021. arXiv:2108.01206.

[149] J. J. Viennot, M. C. Dartiailh, A. Cottet, and T. Kontos. Coherent coupling of a single spin to microwave cavity photons. *Science*, 349:408, 2015.

[150] N Samkharadze, G Zheng, N Kalhor, D Brousse, A Sammak, U C Mendes, A Blais, G Scappucci, and L M K Vandersypen. Strong spin-photon coupling in silicon. *Science*, 359:1123, 2018.

[151] A. J. Landig, J. V. Koski, P. Scarlino, U. C. Mendes, A. Blais, C. Reichl, W. Wegscheider, A. Wallraff, K. Ensslin, and T. Ihn. Coherent spin-photon coupling using a resonant exchange qubit. *Nature*, 560:179, 2018.

[152] J. Corrigan, Benjamin Harpt, Nathan Holman, Rusko Ruskov, Piotr Marciniec, D. Rosenberg, D. Yost, J. L. Yoder, William D. Oliver, R. McDermott, Mark Friesen, Charlie Tahan, and M. A. Eriksson. Manuscript in preparation.

[153] Nathan Holman, D. Rosenberg, J.L. Yoder D. Yost, R. Das, William D. Oliver, R. McDermott, and M.A. Eriksson. Dispersive measurement of a semiconductor double quantum dot via 3d integration of a high-impedance tin resonator. 2020. arXiv:2011.08759.

[154] A. Kerman. Transport properties of quantum dots in the Wigner molecule regime. *New Journal of Physics*, 11(12):123004, Dec 2013.

[155] Nicolas Didier and Alexandre Bourassa, Jrme Blais. Fast quantum nondemolition readout by parametric modulation of longitudinal qubit-oscillator interaction. *Phys. Rev. Lett.*, 115(20):203601, Nov 2015.

[156] Flix Beaudoin, Dany Lachance-Quirion, W. A. Coish, and Michel Pioro-Ladrire. Coupling a single electron spin to a microwave resonator: Controlling transverse and longitudinal couplings. *Nanotechnology*, 27(46):464003, 2016.

[157] Baptiste Royer, Arne L. Grimsmo, Nicolas Didier, and Alexandre Blais. Fast and high-fidelity entangling gate through parametrically modulated longitudinal coupling. *Quantum*, 1(7):11, 2017.

[158] Rusko Ruskov and Charles Tahan. Quantum-limited measurement of spin qubits via curvature couplings to a cavity. *Phys. Rev. B*, 99:245306, June 2019.

[159] Rusko Ruskov and Charles Tahan. Modulated longitudinal gates on encoded spin qubits via curvature couplings to a superconducting cavity. *Phys. Rev. B*, 103:035301, Jan 2021.

[160] C. Eichler and J. R. Petta. Realizing a circuit analog of an optomechanical system with longitudinally coupled superconducting resonators. *Phys. Rev. Lett.*, 120(22):227702.

[161] R. Dassonneville, T. Ramos, V. Milchakov, L. Planat, É. Dumur, F. Foroughi, J. Puertas, S. Leger, K. Bharadwaj, J. Delaforce, C. Naud, W. Hasch-Guichard, J. J. García-Ripoll, N. Roch, and O. Buisson. Fast high-fidelity quantum nondemolition qubit readout via a nonperturbative cross-kerr coupling. *Phys. Rev. X*, 10:11045, 2020.

[162] Sumeru Hazra, Kishor V. Salunkhe, Anirban Bhattacharjee, Gaurav Bothara, Suman Kundu, Tanay Roy, Meghan P. Patankar, and R. Vijay. Engineering cross resonance interaction in multi-modal quantum circuits. *Appl Phys Lett*, 116:152601, March 2020.

[163] Hiraku Toida, Takuya Ohrai, Yuichiro Matsuzaki, Kosuke Kakuyanagi, and Shiro Saito. Control of the transition frequency of a superconducting flux qubit by longitudinal coupling to the photon number degree of freedom in a resonator. *Phys. Rev. B*, 102(9):94502, 2020.

[164] S. Touzard, A. Kou, N. E. Frattini, V. V. Sivak, S. Puri, A. Grimm, L. Frunzio, S. Shankar, and M. H. Devoret. Gated conditional displacement readout of superconducting qubits. *Phys. Rev. Lett.*, 122(8):80502, Feb 2019.

[165] Joni Ikonen, Jan Goetz, Jesper Ilves, Aarne Keränen, Andras M. Gunyho, Matti Partanen, Kuan Y. Tan, Dibyendu Hazra, Leif Grönberg, Visa Vesterinen, Slawomir Simbierowicz, Juha Hassel, and Mikko Möttönen. Qubit measurement by multichannel driving. *Phys. Rev. Lett.*, 122(8):80503, Feb 2019.

[166] C G L Bøttcher, S P Harvey, S Fallahi, G C Gardner, M J Manfra, U Vool, S D Bartlett, and A Yacoby. Parametric longitudinal coupling between a high-impedance superconducting resonator and a semiconductor quantum dot singlet-triplet spin qubit. 2021. arXiv:2107.10269v1.

[167] S. N. Shevchenko, Sahel Ashhab, and Franco Nori. Landau–Zener–Stückelberg interferometry. *Phys. Rep.*, 492(1):1–30, 2010.

[168] Ming-Bo Chen, Shun-Li Jiang, Ning Wang, Bao-Chuan Wang, Ting Lin, Si-Si Gu, Hai-Ou Li, Gang Cao, and Guo-Ping Guo. Microwave-resonator-detected excited-sate spectroscopy of a double quantum dot. 2021. arXiv:2102.08169v1.